Multicomponent seismic imaging of sand reservoirs:

Middle Magdalena Valley, Colombia.

A Thesis

Presented to

the Faculty of the Department of Earth and Atmospheric Sciences

University of Houston

In Partial Fulfillment

of the Requirements for the Degree

Master of Science

By: Maria Virginia Mason

May 2013

Multicomponent seismic imaging of sand reservoirs: Middle Magdalena Valley, Colombia

MASON, MARIA VIRGINIA

APPROVED:

R. Stewart, PhD.
Dept. of Earth and Atmospheric Sciences

E. Baysal, PhD.
Chief geophysicist at Paradigm
Dept. of Earth and Atmospheric Sciences

P. Mann, PhD.
Dept. of Earth and Atmospheric Sciences

Dean, College of Natural Sciences and Mathematics

ACKOWLEDGEMENTS

First of all I would like to thank my thesis advisors Robert Stewart, Edip Baysal, and Paul Mann for their guidance along the whole process. Also my gratitude goes to Ecopetrol for their permission to use their seismic data, and to Lumina Geophysical to provide me with the software I needed for this work. I especially thank Gabriel Gil and Cristhian Sanchez for their valuable help with the software and interpretation.

A very special thank to Raul Stolarza, Santiago Juranovic (Data Seismic S.A.), and Alejandro Juranovic, not only for giving me the financial support to achieve my masters degree, but also to give me the technical and personal support every time I need it.

My gratitude also goes to the University of Houston and Universidad Nacional de La Plata (UNLP) for letting me learn from great professors.

My main gratefulness goes to Lenny, for his unconditional support; to my family and friends in Argentina, for making me feel them close in spite of the geographical distance. I would also like to thank my Houston family and friends I was lucky to meet at school and work, for making me feel at home.

Multicomponent seismic imaging of sand reservoirs:

Middle Magdalena Valley, Colombia.

An Abstract of a Thesis

Presented to

the Faculty of the Department of Earth and Atmospheric Sciences

University of Houston

In Partial Fulfillment

of the Requirements for the Degree

Master of Science

By: Maria Virginia Mason

May 2013

ABSTRACT

Many current resource exploration targets are more difficult to image and assess than in the past; thus, more complete and sophisticated techniques, such as the multicomponent (3C) seismic method, are needed. The scope of this work is to image the sand reservoirs present in the Tenerife Field in the Middle Magdalena Valley, Colombia. The analyzed data include a migrated 3D-3C volume, raw shot gathers from two 2D-3C test lines acquired with different source sizes and depths, and varying receiver depths. Additionally, well logs and VSP from three wells in the field were incorporated into this study.

For the 2D-3C processing, a conventional processing workflow was followed except for some steps in the radial channel, such as refraction statics and velocity picking. Better results were obtained with refraction statics computed from manually-picked S-wave first breaks and with semblances generated separating positive from negative offsets. The effect of the different acquisition parameters was more evident in PS-waves, observing an improvement in the stack when increasing the fold, and source size and depth. On the other hand, PP-waves showed nearly the same stack quality with the different acquisition parameters.

Vp/Vs maps at the top of the target-horizon showed low values around one of the producing wells (Tenerife-2), which is known to have a good stack of clean sands, based on log data. The other two wells presented no Vp/Vs anomalies; in Tenerife-1 the gross thickness is far below conventional seismic resolution and in Tenerife-3 the shale-content

is very high. Thus, in the Tenerife Field, there seems to be a direct correlation between low Vp/Vs values and good quality reservoir sands.

Table of Contents

List of Figures

List of Abbreviations

V_P	: P-wave velocity
V_S	: S-wave velocity
γ	: ${V_P}/{V_S}$
ΔT_{PP}	: two-way travel time difference between two events in PP time
ΔT_{PS}	: two-way travel time difference between two events in PS time
PS-waves	: P to S in reflections (converted-waves)
MMVB	: Middle Magdalena Valley Basin
MEU	: Middle Eocene Unconformity
CDP	: Common depth point
CCP	: Common conversion point
ACP	: Asymptotic conversion point
MP	: Midpoint between source and receiver
CP	: PS-wave conversion point
S/N	: Signal-to-noise ratio
ABA	: Air blast attenuation
CT	: total refraction statics correction
CT_I	: static correction for the incident wave
CT_E	: static correction for the emergent wave
PSTM	: Pre-stack time migration
DMO	: Dip moveout
T	: Wavelet period

VSP	: Vertical seismic profiling
GR	: Gamma Ray log
SP	: Self Potential log
AI	: PP acoustic impedance
SI	: PS impedance

Chapter 1: Introduction

Many current resource exploration targets are more difficult to image and assess than in the past. To try to answer these challenges more complete and sophisticated techniques should be considered. The multicomponent seismic method includes conventional P-wave analysis, but in addition uses converted-wave events (P to S in reflections). Converted-waves have found use (especially complementing PP images) for hydrocarbon exploration, CO_2 sequestration, fault mapping, and hydrothermal studies. As P- and S-waves reflect differently from different interfaces, the use of converted-waves can often provide a better determination of rock type properties, and fluid saturation in hydrocarbon reservoirs (MacLeod et. al., 1999; Stewart et. al., 2003; Wei and Li, 2003).

This work is focused in the multicomponent seismic imaging of sand reservoirs in the Tenerife Field; one of Ecopetrol's operated areas located in Middle Magdalena Valley, Colombia (Figure 1.1). The reservoir is within the Mugrosa's sand units with thickness of 5m, far below conventional seismic resolution. Including converted-waves in the seismic analysis is aimed to help in the lithology and fluid discrimination by analyzing extracted Vp/Vs values. The data for analysis includes a migrated 3D-3C volume previously processed, raw shot gathers from two 2D-3C test lines acquired with different amounts of charge and source and receiver depths; plus well logs and VSP from three wells in the field. Inversions of the 3D PP and PS volumes, well logs, PP and PS synthetics, and the 2D-3C lines were correlated to investigate if PS-waves provide useful leads or indicators of rock type and hydrocarbon saturation.

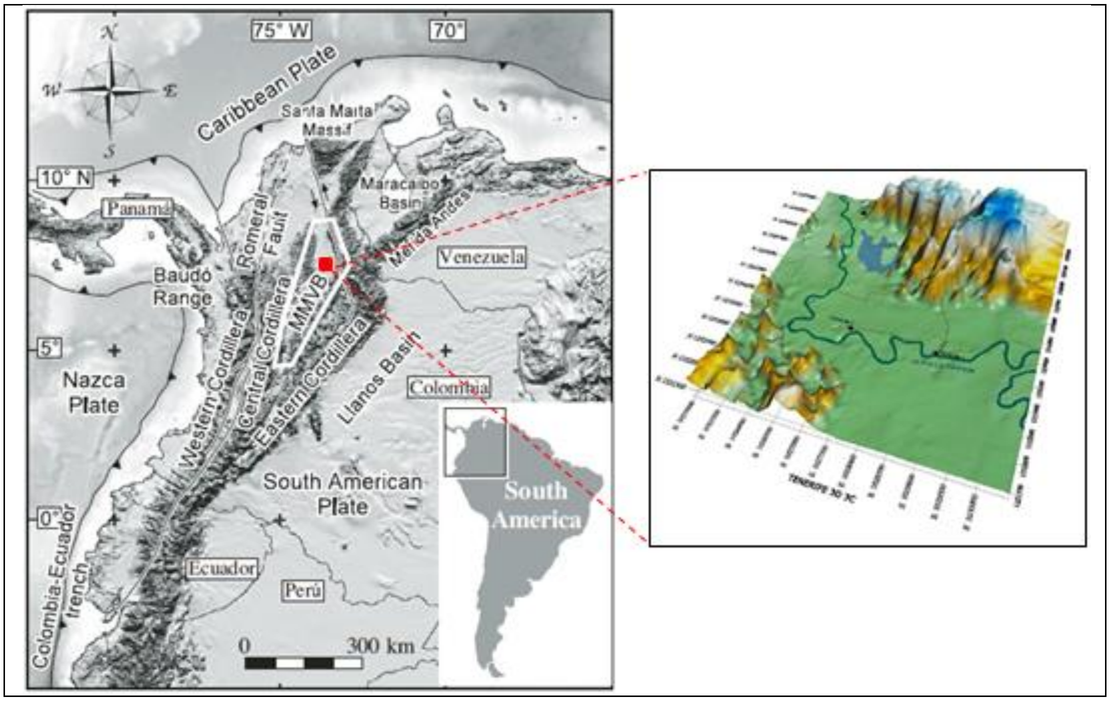

Figure 1.1: Map showing the location of Middle Magdalena Valley Basin (MMVB - delimited with white), the 3D3C survey area and the 2D3D lines crossing it (modified from Gomez et al., 2005).

1.1 Previous work in the Tenerife Field

The Tenerife Field is a small field discovered in 1971 with the successful drilling of Tenerife-1. This was followed by the drilling of Tenerife-2 and -3. Unfortunately, Tenerife-3 was a dry well. At that time, the wells locations were supported by the interpretation of 2D seismic lines and surface geology.

Several 3D-3C surveys have been conducted in Colombia in the past few years but in almost none of them the horizontal components were interpreted nor even processed.

According to Agudelo et al. (2013), the Tenerife 3C-3D dataset was acquired by Ecopetrol in 2009 as the first converted-wave-oriented experiment (from acquisition design to interpretation) in Colombia. It was aimed to improve the structural, geological and petrophysical interpretation of the field.

1.2 Middle Magdalena Valley Geology

The Middle Magdalena Valley is one of Colombia's 23 sedimentary basins. It is one of the most important as it includes the first giant oil field (LaCira-Infantas). Discovered in 1918, it has produced nearly 750 million barrels of oil from an estimated OOIP of 3.9 billion barrels of oil (Prieto et al., 2009). Forty-one oil fields have been discovered in the basin, and it still contains one of the most prolific areas to be explored: the Cretaceous carbonate plays.

Structural development took place through different stages linked to the tectonic events of the northwest corner of South America occurred during Late Triassic, Middle Cretaceous, Early Paleogene, and Middle Neogene (Barrero et al., 2007).

Studies performed by Mulholland (1943), Swolf (1947), Morales (1958), Sanderson (1951), Lobo et al. (1999), and Gomez (2005) show that during the Triassic and until the beginning of the Cretaceous, the basin area acted as a rift zone. During the Cretaceous, the basin was represented as a back-arc behind the Andes' subduction zone with mostly marine deposits. Late Cretaceous – Paleocene was characterized by a compressional deformation process due to the accretion of the terrane (which later formed the Western Cordillera) to the South American craton, causing folding and erosion of the Cretaceous sequence. At Late Eocene – Early Oligocene the Central Cordillera uplift started. At the same time the Magdalena basin, and current Eastern Cordillera, formed part of a huge foreland basin with basal continental deposits (fluvial and deltaic), lying unconformable over the Cretaceous succession. Finally, in the Late Miocene – Pliocene, a folding and thrusting period occurred; transforming the Middle Magdalena Valley in an intermountain basin.

Structural deformations in the MMVB are strongly related to compressions due to the eastwards advance of the Central Cordillera and westwards movement of the Eastern Cordillera. Due to its location (highlighted with a star in the geological cross section displayed in Figure 1.2), the east of Tenerife Field is affected mainly by basement-involved inverted normal faults, such as La Salina Fault. These are originated by compressions over a previously rifted basin. The western part is mainly affected by high-angle east verging reverse faults.

Generally within the field two main structural patterns are observed above and below the Middle Eocene Unconformity (MEU). Below the MEU faulted blocks are present, dominated by east-verging thrust and partially inverted Mesozoic normal faults. The sequence above the MEU is mainly affected by northeast striking normal faults indicating younger local extension. Thus the reservoir units in the Tenerife Field are mostly affected by normal faulting oriented oblique to the maximum horizontal stress (Velasquez-Espejo, 2012).

In Figure 1.3 a 2D seismic section (vertical channel) across the 3D survey in the Tenerife Field is shown. Also SP and Resistivity logs for the Tenerife-2 well, the top of Mugrosa-B and -C and the MEU are displayed.

Figure 1.4 describes the lithostratigraphic column. It is composed by Jurassic continental deposits overlapped by Cretaceous sediments. As it is mentioned above, late Cretaceous was characterized by a marine transgression in which limestones and shales were deposited. Paleogene units are mainly composed of siliciclastic rocks deposited mainly under continental condition with some marine influence (Barrero at al., 2007).

The reservoir in the Tenerife Field is a complex of sandstone fluvial channels within the Mugrosa Formation at 2133 m deep (from Agudelo et al., 2013). The main reservoir rocks are the lower Oligocene basal sands with average porosities of 15%-20% and permeabilities of 20-600 mD (Barrero et al., 2007). This sequence is composed of sandstones (usually from 2 to 5 m thick), occasional carbonates and clays with a total thickness of 500 - 800 m. Due to the meandering river depositional environment, the sand bodies are rather isolated and random in occurrence and can extend to 30 m thick (from ION Processing Report).

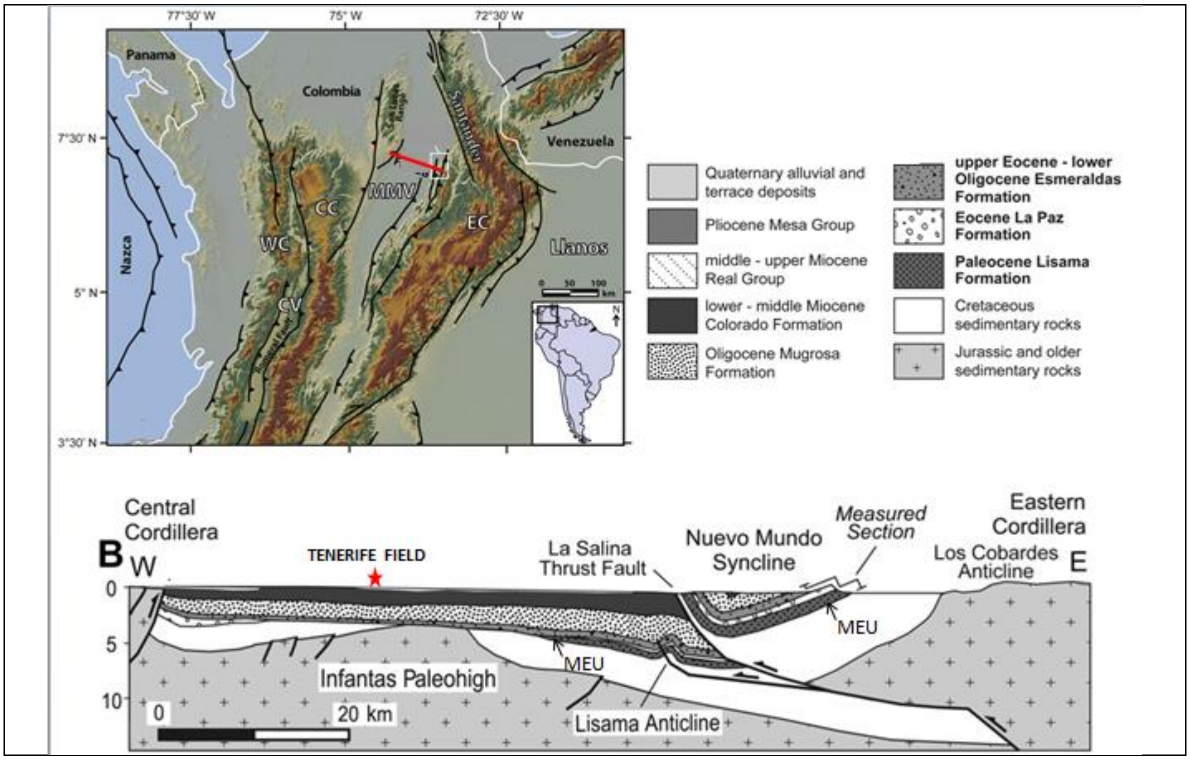

Figure 1.2: Map showing the location (in red) of the geological cross section displayed below (modified from Moreno et al., 2011).

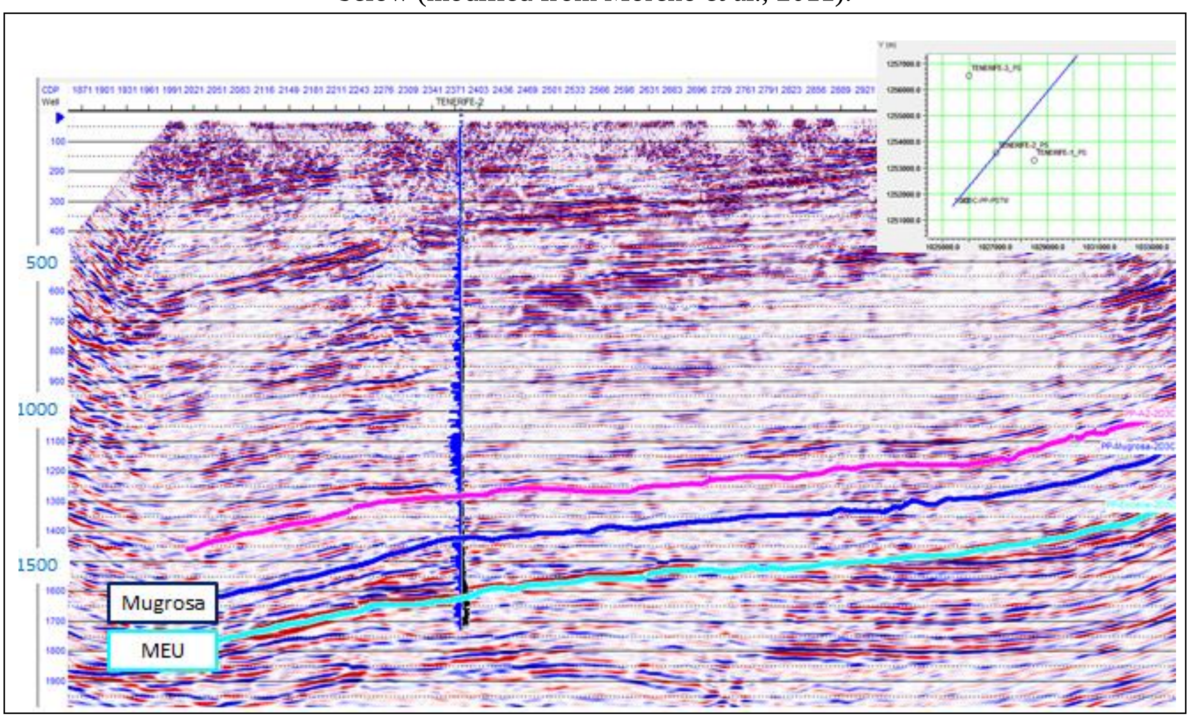

Figure 1.3: Seismic section of a 2D line crossing the Tenerife 3D-3C survey; SP and Resistivity logs for the Tenerife-2 well.

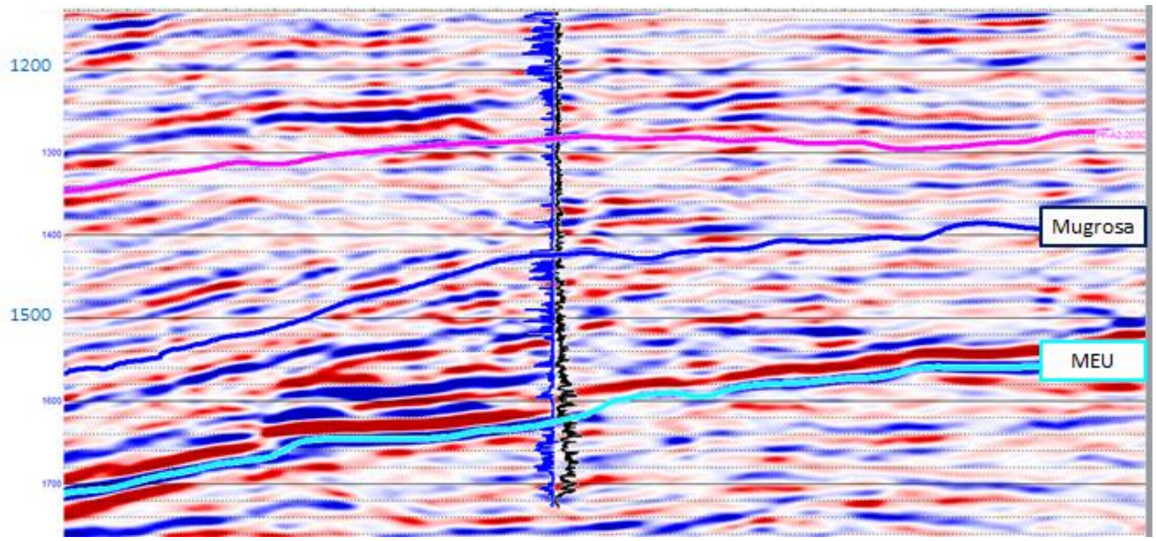

Figure 1.3 (cont.): Zoom of the display on top focusing in the well tie at the Mugrosa-C and MEU level.

1.3 Petroleum Systems in the Tenerife Field

According to Barrero et al. (2007), the main source rocks of the petroleum systems are related to the limestones and shales of the Cretaceous La Luna, Simiti and Tablazo units. These source rocks contain mostly type II organic matter and were deposited in a poorly oxygenated environment.

Petroleum migration path is mainly guided by the Eocene unconformity, which separates the primary reservoir from the Cretaceous source rocks. Barrero et al. (2007) suggests three migration paths: 1) direct vertical migration, where La Luna sub-crops the Eocene unconformity; 2) lateral migration along the Eocene sandstone carrier; 3) vertical migration via faults in the area where La Luna doesn’t sub-crop the Eocene unconformity.

Almost all the oil in the field is extracted from the Paleogene sandstones; the interbedded non marine ductile claystones from Colorado and Esmeralda Formations constitute a seal for the Paleogene sandstone reservoirs (Barrero et al., 2007).

1.4 Paleogene Stratigraphic Units

As the main reservoir in the Tenerife field is associated to the Paleogene sands, only the Paleogene units are described in detail in this section.

According to Gomez et al., (2005) the Paleogene units are described as follows:

- La Paz Formation (Middle Eocene) is composed of mudstones and sandstones above the Eocene Unconformity that were deposited in a fluvial environment indicating the complete transformation of the Middle Magdalena Valley Basin into a continental basin (Ramirez, 1998; Gomez, 2001 in Gomez et al., 2005). It is composed of two major units; a lower one, characterized by silty mudstones with a vertical root bioturbation and no organic material, and an upper unit consisting of elongated cross-bedded sandstones.
- The Esmeraldas Formation (Late Eocene) has a very similar composition to the lower unit of La Paz, characterized by layers of sandstones embedded within the mudstones and siltstones.
- The Mugrosa Formation (Oligocene) overlies conformably the Esmeraldas Formation. Gomez et al., (2005) splits it in two units; a lower one consisting of

fining-upward medium-grained sandstones organized in S-N trending bodies interbedded with mudstones, and an upper unit composed of distinctive fining-upward sandstone-mudstone sequence deposited along the inner bends of meandering rivers.

- Colorado Formation (Late Oligocene – Early Miocene) is composed of fining-upward sequences of cross-bedded sandstones and variegated mudstones with interbeds of ripple-laminated sandstones. The sandstones in this interval are conglomeratic and coarser grained, indicating a decrease in the channel sinuosity and increase in the flow energy (Gomez et al., 2005).

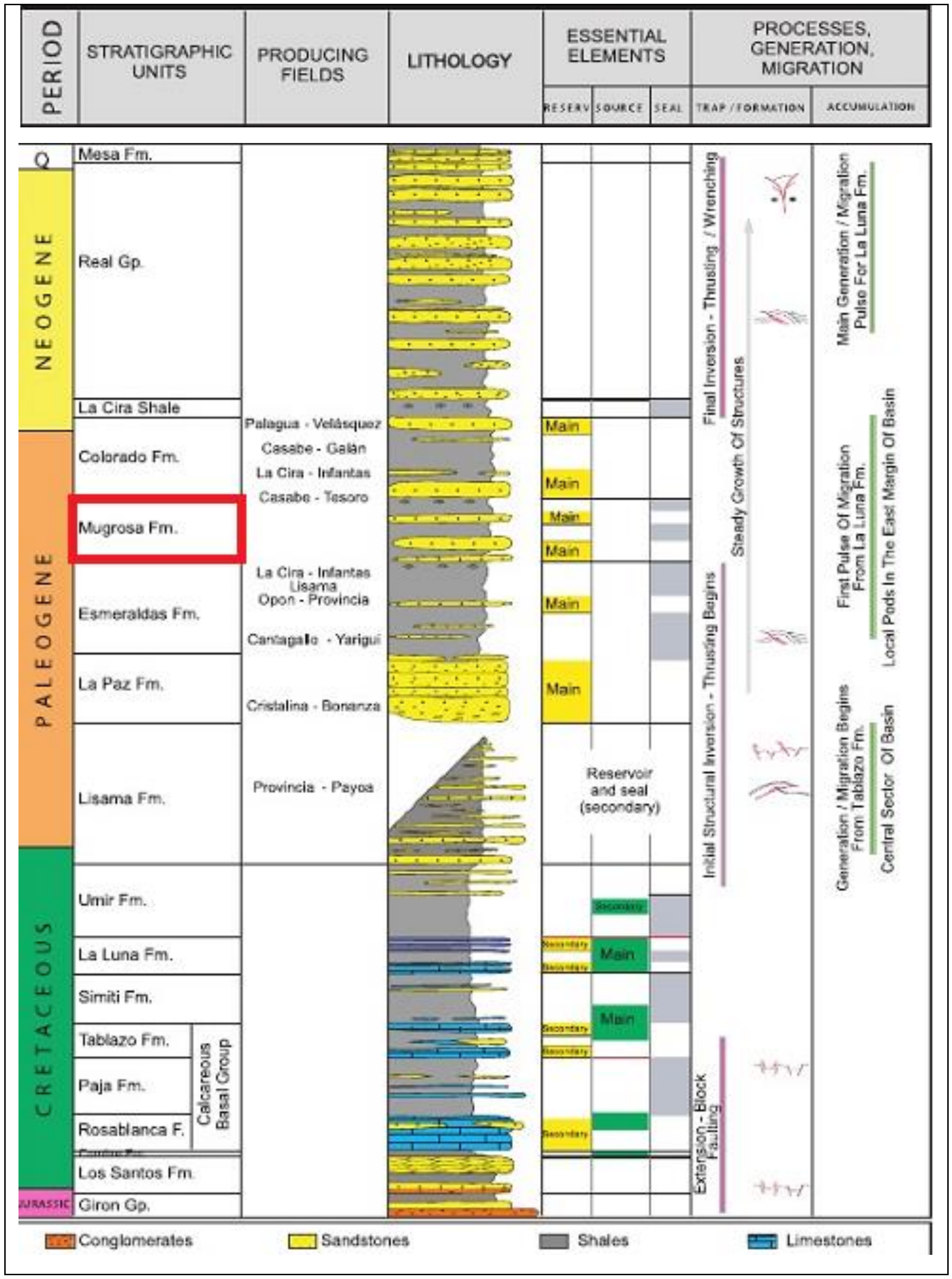

Figure 1.4: Lithostratigraphic column of the Middle Magdalena Valley. The formation of interest (Mugrosa Formation) is highlighted in red (modified from Barrero et al., 2007).

Chapter 2: Survey 2D-3C: PP-waves

2.1 Acquisition

The 2D-3C test lines were acquired with dynamite sources and one DSU-3 (Digital Sensor Unit) at each receiver station. Different shot and receiver burial depths were tested. According to Bland and Gallant (2001), it is advantageous to bury 3-C geophones since the signal-to-noise ratio improves by approximately 3 dB for every 10 cm of burial depth. Geophones, in this Colombian case, were buried 10 and 20 cm to test if in this terrain the geophone depth had a significant impact in the quality of the seismic data.

Line EXP-TEN-2D3C-1 was 9 km long with 900 stations and 10 m separation. Geophones in this line were buried 10 cm. Line EXP-TEN-2D3C-2 was 50 cm apart from line EXP-TEN-2D3C-1 with a length of 3 km; 150 stations with 20 m spacing. Geophones' burial depth was of 20 cm.

Also different shot arrangements (A1 to A5) were tested on line EXP-TEN-2D3C-1 including varying depths and charge size. For the A1 configuration, the nominal shot spacing was 40 m. A2 to A5 were shot with a variable and less dense spacing.

The different shot configurations are described in Table 2.1. The 2D line was processed considering all shots for the A1 source configuration and, for comparison purposes, a decimated version was created to have almost the same shot spacing as A2–A5.

	A1	A2	A3	A4	A5
Hole Depth (m)	10	15	15	15	20
Charge (kg)	2.7	1.8	3.6	4.5	2.7
Source Interval (m)	40	150	150	150	150
Receivers Interval (m)	10	10	10	10	10
Minimum Offset (m)	4.25	4.25	4.25	4.25	4.25
Maximum Offset (m)	7525	7525	7525	7525	7525
Nominal Fold	150	38	38	38	38

Table 2.1: Different shot depths and charge size tested in the 2D line.

2.2 Processing

The first step in the data processing was to download the data which was in SEG-D files and reformat it to **ProMAX/SeisSpace** internal format. The geometry was built based on the observers' reports that were provided in an Excel file. Source and receiver coordinates were extracted from the SPS files.

Once the geometry was applied, the vertical and horizontal channels in the raw shot records were split. Figure 2.1 shows a schematic diagram of 3C recording and an example of a raw shot gather for the vertical, radial and transverse channel (displayed with AGC and a lateral and vertical zoom). For the PP-wave processing, only the vertical component was used.

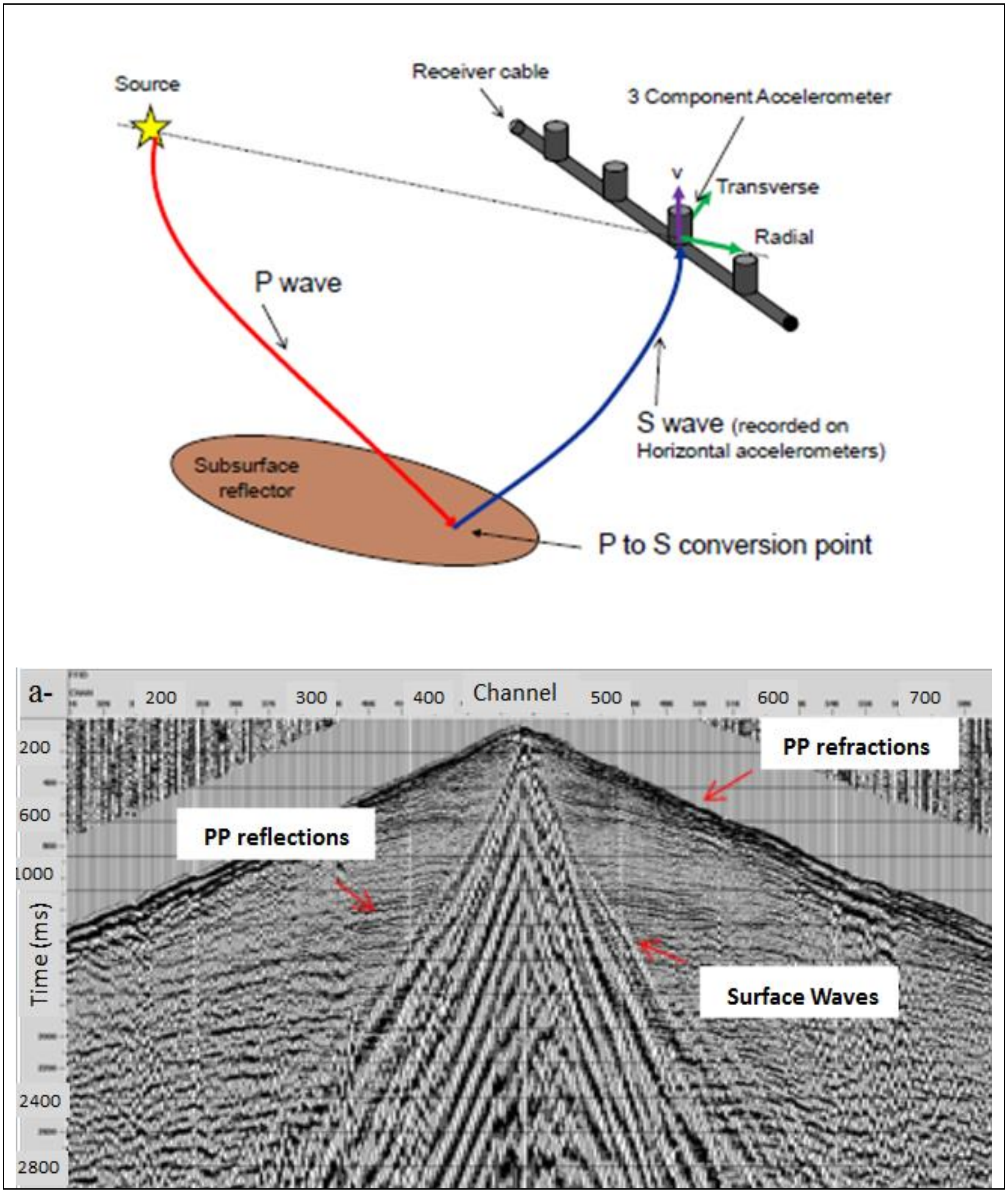

Figure 2.1: (top) Schematic diagram of 3C recording (from ION processing report) and raw shot gathers from (a) the vertical channel.

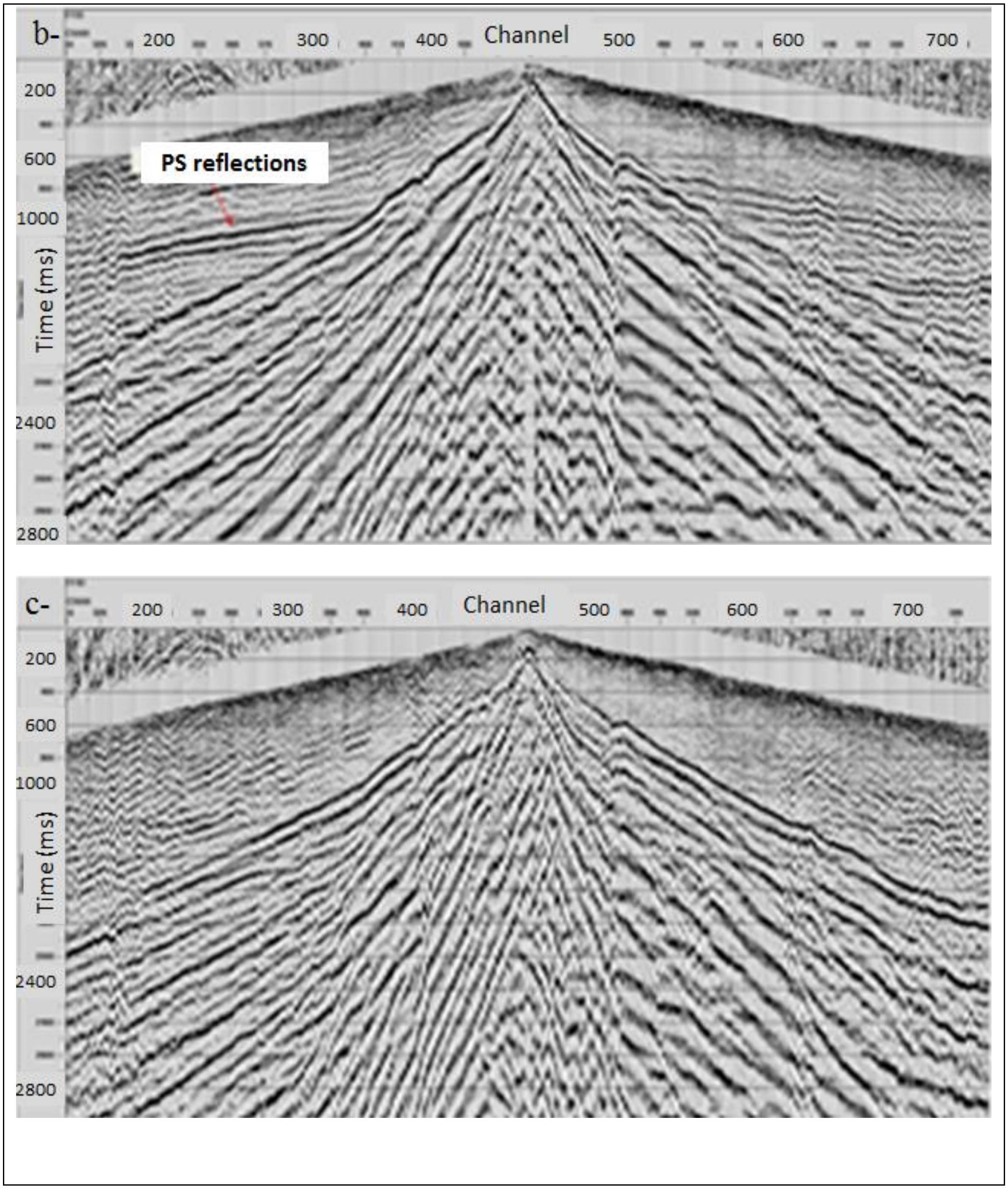

Figure 2.1: Raw shot gathers from (b) the radial channel, and (c) the transverse channel.

Figure 2.2 shows typical shot records for the different acquisition parameters for the vertical channel, displayed with no gain. The subsequent steps in the processing flow for the vertical channel are described in the following paragraphs; Appendix A shows images of the PP-stacks as going through some of the processing stages.

- Trace Editing and Noise Attenuation

Every shot record was controlled to identify noisy and defective traces taking into account the comments found in the Observer Report (inverted traces, dead traces, noisy traces, etc.).

The trace editing stage had two parts: The elimination of problematic traces (kill) and the muting of parts of one or several traces (surgical mute). A proprietary workflow was used to attenuate ground roll and anomalous amplitudes.

- Static Corrections

For static corrections calculation, the delay time method was used with GLI (Generalized Linear Inversion) of Seismic Studio.

The selected offset for refractor velocity calculation was 200-1200 m. An auto-picking program was run to pick first breaks and then a manual shot record edition was used to achieve a more reliable static set. A one weathering layer model was chosen. A constant weathering velocity was used, because there were no up-holes or refraction profiles available.

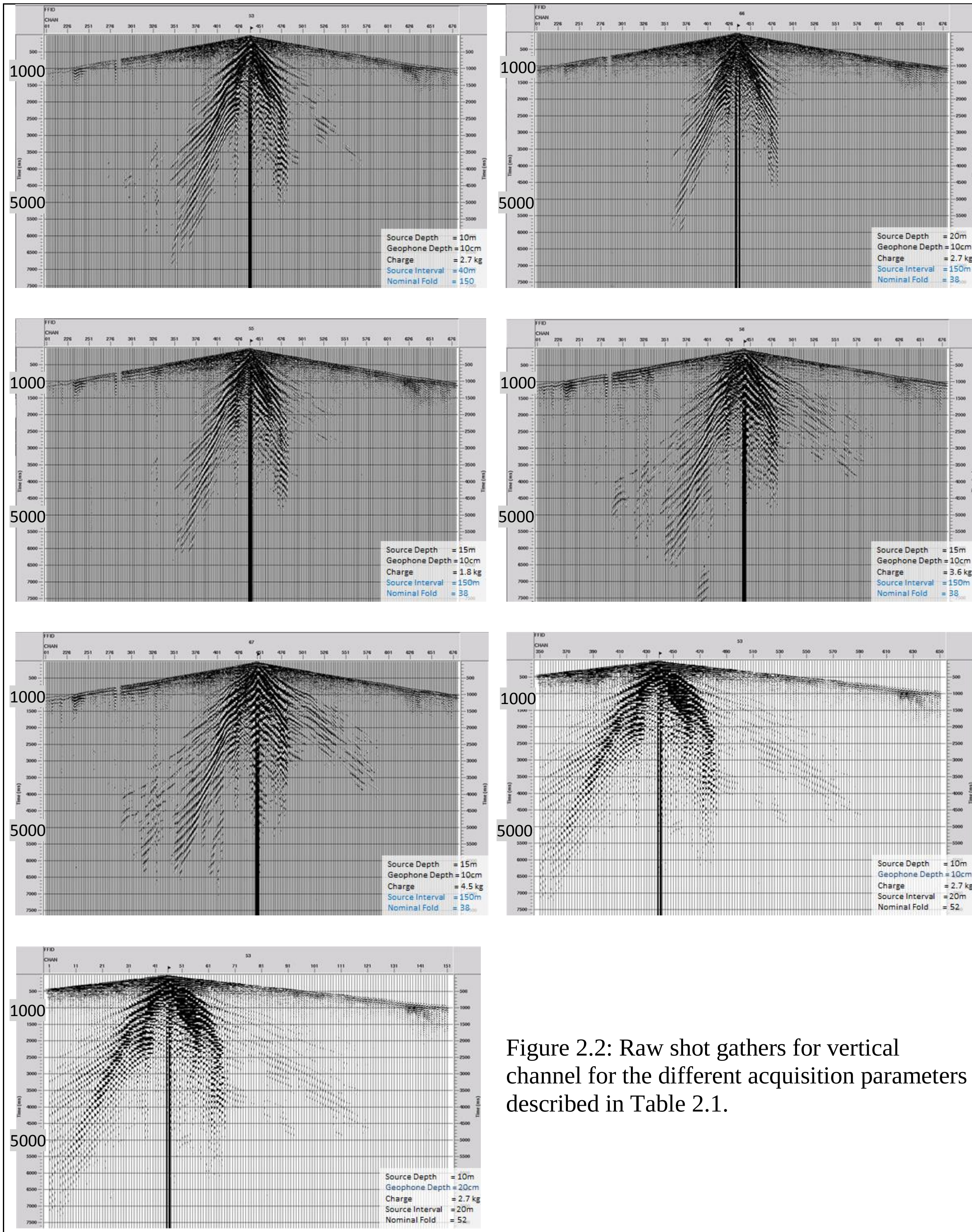

Figure 2.2: Raw shot gathers for vertical channel for the different acquisition parameters described in Table 2.1.

Model summary:

- One weathering layer model
- Weathering Velocity: 550 m/sec
- FB picking offset: 200 – 2200 m
- Final Datum: 150 m
- Replacement Velocity: 2200 m/sec

- Pseudo-true Amplitude Recovery

Different values for spherical spreading and inelastic attenuation were tested to compensate for amplitude losses due to waves propagation. The main disadvantage of using Spherical Spreading for modeling amplitude losses is that it is a function of the velocity, which is something not accurate at this stage of the processing sequence. So, a good model for the Pseudo-true Amplitude Recovery curve was obtained with t^n, being

- Time-Power constant : 3
- Recovery Curve: 3 dB/s
- Application Length: 3000 ms

- Surface consistent amplitude compensation

Once these corrections were applied, surface consistent amplitudes were computed using receivers, shots and offset. A noise reduction by Air Blast Attenuation (ABA) was also applied before the analysis.

Then, using the amplitudes' mean values, a trace rejection with "out of range" amplitudes was done, eliminating the anomalous ones.

With the compensated amplitudes a surface consistent deconvolution (see next point for description) was applied and a new Air Blast Attenuation (ABA).

- Surface Consistent Deconvolution

Starting with an initial autocorrelation and power spectrum, different operator lengths were tested both for spiking and predictive deconvolution. For the predictive deconvolution also different predictive distances were tested.

After comparing the results, based in the frequency content mainly in the target and continuity of events, the following deconvolution was chosen:

- Type: Surface consistent spiking deconvolution
- Operator length: 240 ms
- White Noise: 0.1%
- Components: Source, receiver, and offset

The aim of the spiking deconvolution is basically to try to compress the wavelet into a zero-lag spike of zero width (i.e. $\delta(t)$, Dirac delta function).

- Velocity Analysis

Two velocity analyses were performed using Semblance, Gathers, Dynamic Stack and CVS (Constant Velocity Stack). The first velocity was picked every 1 km, residual statics were calculated and applied, and a second semblance was created every 500 m for a denser velocity picking.

- Residual Static Corrections

After the first velocity analysis, residual statics were calculated using the Maximum Power Autostatics (Ronen and Claerbout, 1985) program. These static corrections are surface consistent with an analysis window width of 1800 ms centered in a hand-picked horizon that followed the structural trend. After the second Velocity Analysis, a second pass of Maximum Power Autostatics was run with the same parameters, diminishing dispersion.

- Structural Filter

So as to strengthen coherency of linear events, a structural filter designed by Lumina Geophysical was applied to the gathers. This is a smoothing and filtering technique used in prestack noise reduction that preserves edge (continuity in seismic events) while removing noise.

It is a one-dimension filter that follows the dip of seismic events within a predefined time-space (nt-nx) window. The filter estimates the median value within a series of amplitude values on the input data based on dip of the data.

Structural Filter can handle strong random noise in the pre-stack domain and works very well when dipping events are present. It preserves lateral amplitude variation with offset (AVO) in seismic gathers.

- F-XY Decon Pre-stack

Another step in the cdp noise reduction included the use of F-XY Decon pre-stack. In order to be able to use it in the 2D line a pseudo 3D was created, using shot record as in-lines and channels as cross-lines. Different “in-lines” and “cross-lines” combinations were tested and the following parameters were chosen focusing the decision in the best Signal/Noise but avoiding a synthetic looking stack.

Selected Parameters:

- Number of in-lines: 3
- Number of cross-lines: 9
- Operator Length: 250 ms
- Frequency range: 5-250 Hz

- Trim Statics

In this stage small time shifts were applied to each trace of a CDP gather (if needed) improving the coherency of the stack. These time shifts were computed from the correlation of the input trace and an external stack model. The aim was to correct for any remaining time sifts that were not considered by the surface-consistent residual statics analysis.

The selected parameters for Trim statics were:

- Statics maximum shift: 6 ms
- Minimum number of live samples in window : 15%

- Stretch mute tests

Stretch mute values of 10%, 20%, 30%, 40%, 50%, 60%, and 70% were tested for stacking. After analyzing the signal/noise with the different values, a 50% stretch mute was chosen. This allowed a contribution of a maximum offset of ~7500 m.

- Post-stack time migration

Percentages of the RMS velocity (from 70% to 100% every 10%) were tested for the Stolt migration algorithm. The velocity field was smoothed using a smoothing operator length of 100 m. This migration was done as a QC for the pre-stack time migration (PSTM), anticipating what results should be expected.

- Pre-stack time migration (PSTM)

Migration aperture tests were run over the line in the x-*t* domain, including by stretch mute and image location distance, defining the offsets to be migrated.

The values tested for stretch mute were 2%, 3%, 4%, 5%, 10%, 20%, 30%, and 40%, and for image location distance: 0-1500 m, 0-2500 m, 0-4000 m, 0-5500 m, and 0-7500 m.

A 2D Kirchhoff pre-stack time migration with a 10% stretch mute aperture was run on the line. A new semblance (every 500 m) was created to do a residual velocity analysis. A final PSTM with the refined velocity was run for the line. The PSTM gathers were kept with an offset range of 50 - 7500 m, every 50 m between traces.

- Post- process

The following post-stack process was applied:

- F-X Decon
- Time variant band-pass filter
- AGC (500 ms)

2.3 Results

Figures 2.3 and 2.4 show the stacks for the two lines acquired with the different parameters mentioned above. All the figures correspond to migrated stacks for the vertical channel processed following the step described in the previous section. In Figures 2.3 and 2.4 the stacks are displayed without and with post-process, respectively.

2.4 Comments

Several source configurations were tested considering different charge amounts and burial depths (A1 – A5). For A1 shots were exploded with 40 m spacing, while, for A2 – A5, shots spacing was on average 150 m. In order to compare the five different sets of shots, A1 was decimated to make its fold consistent with A2 –A5. Figures 2.3 and 2.4 show the migrated stacks for the vertical channel (A1 to A5 acquisition configurations) for lines EXP-TEN-2D3C-1 and EXP-TEN-2D3C-2. For line EXP-TEN-2D3C-1 the receivers' depth was of 10 cm and for line EXP-TEN-2D3C-2 of 20 cm. In Figure 2.3 the stacks are displayed with no AGC post-stack as the aim is to compare the pseudo-true amplitude at the deeper events, among other things.

When comparing the migrated seismic sections described above (with and without post-process), there is no considerable difference between them; meaning that the nominal fold, amount of charge and sources' and receivers' depths are not critical for improving PP waves' imaging in this field.

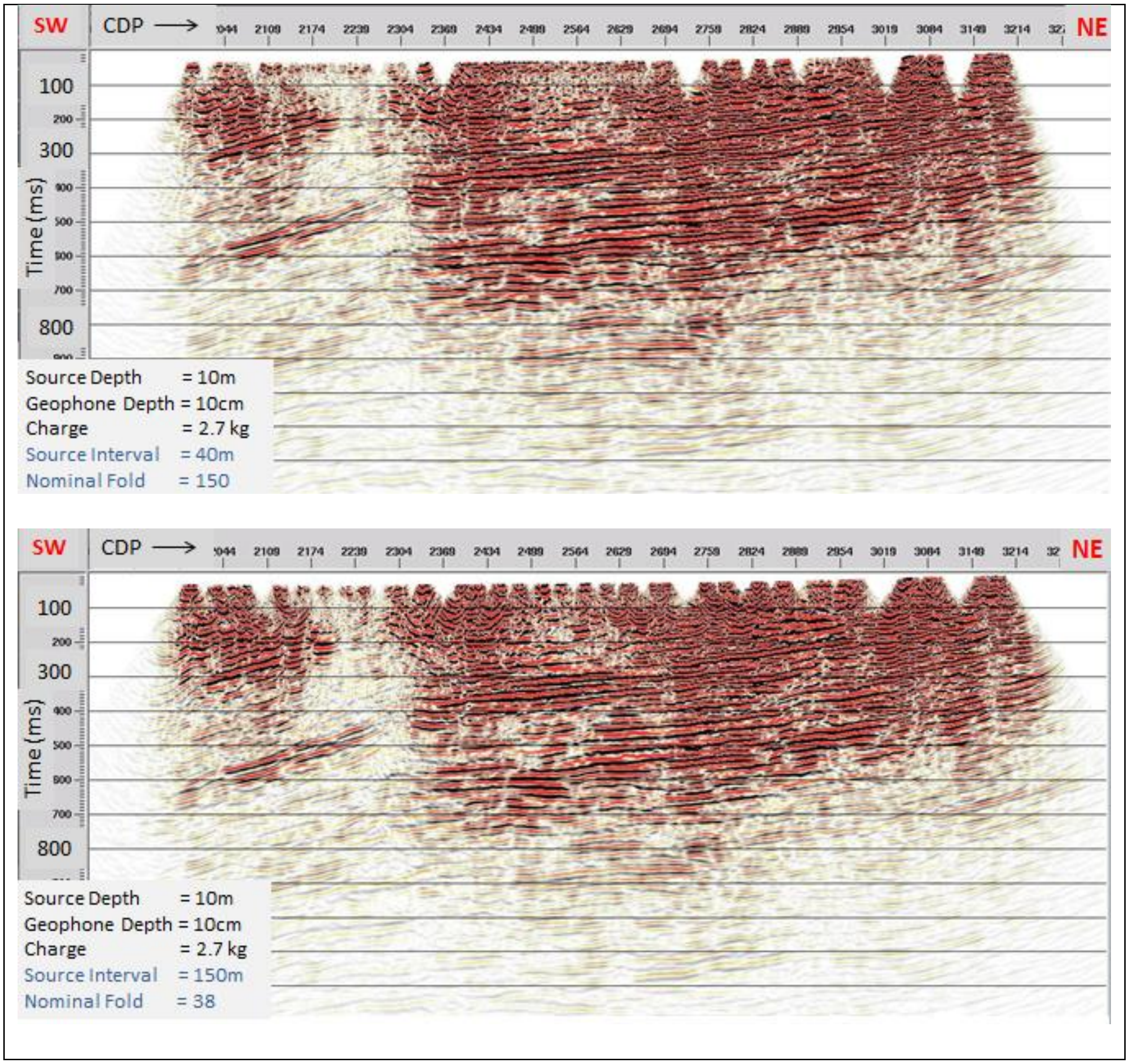

Figure 2.3: Migrated stacks for the vertical channel (displayed with no gain) acquired with the different acquisition parameters. The acquisition parameters are described in the box in the bottom left corner.

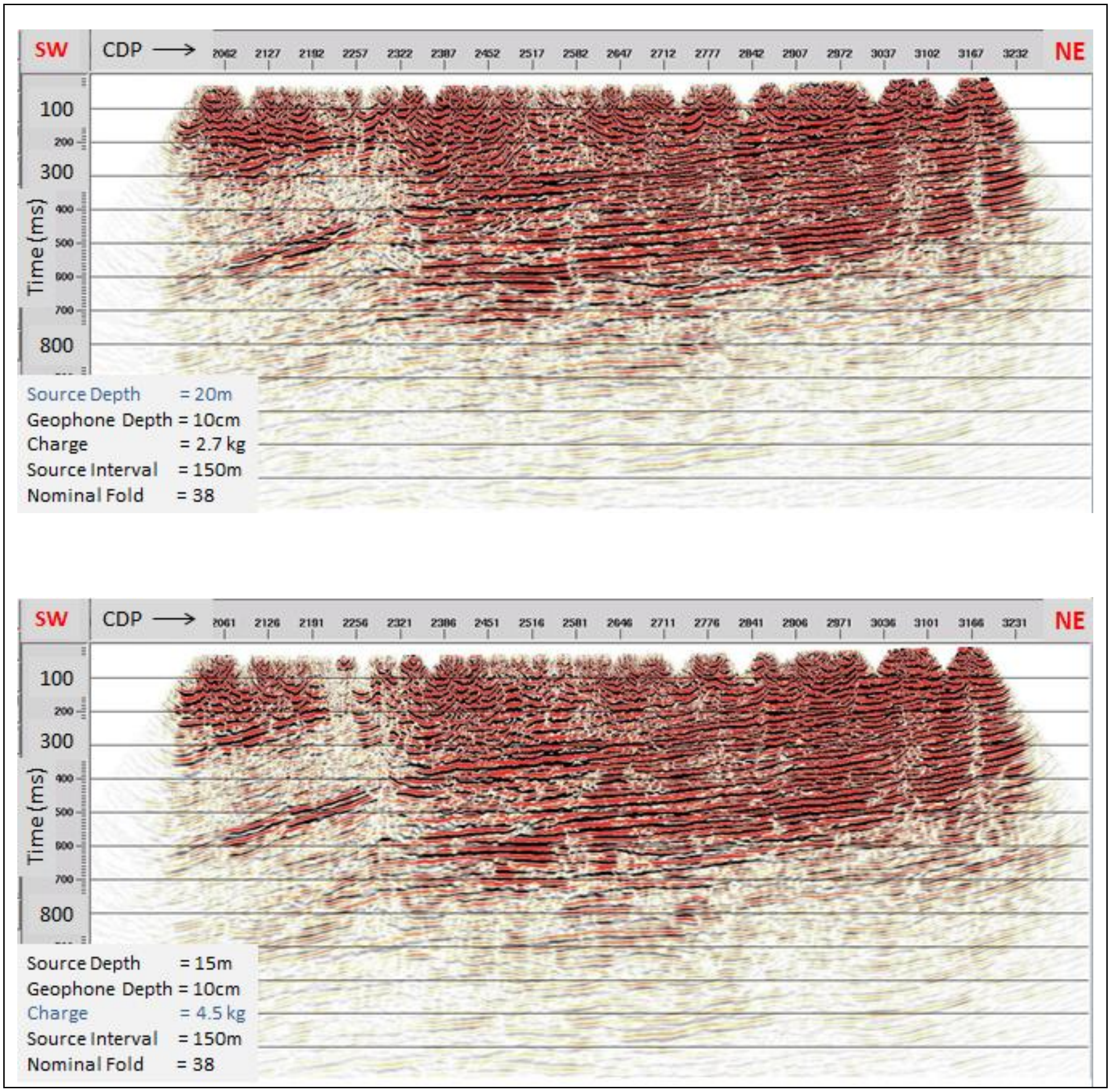

Figure 2.3 (cont.): Migrated stacks for the vertical channel (displayed with no gain) acquired with the different acquisition parameters. The acquisition parameters are described in the box in the bottom left corner.

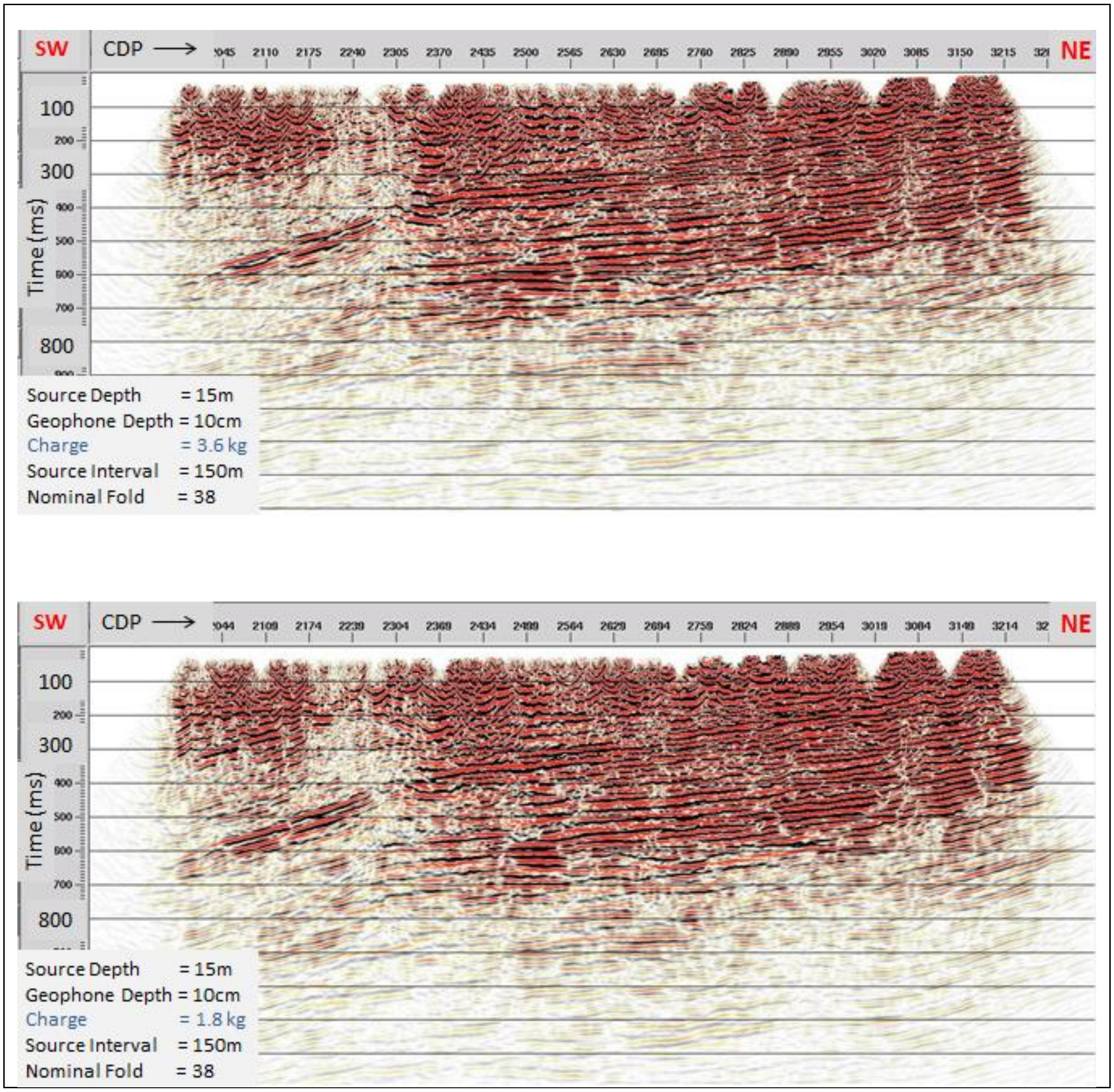

Figure 2.3 (cont.): Migrated stacks for the vertical channel (displayed with no gain) acquired with the different acquisition parameters. The acquisition parameters are described in the box in the bottom left corner.

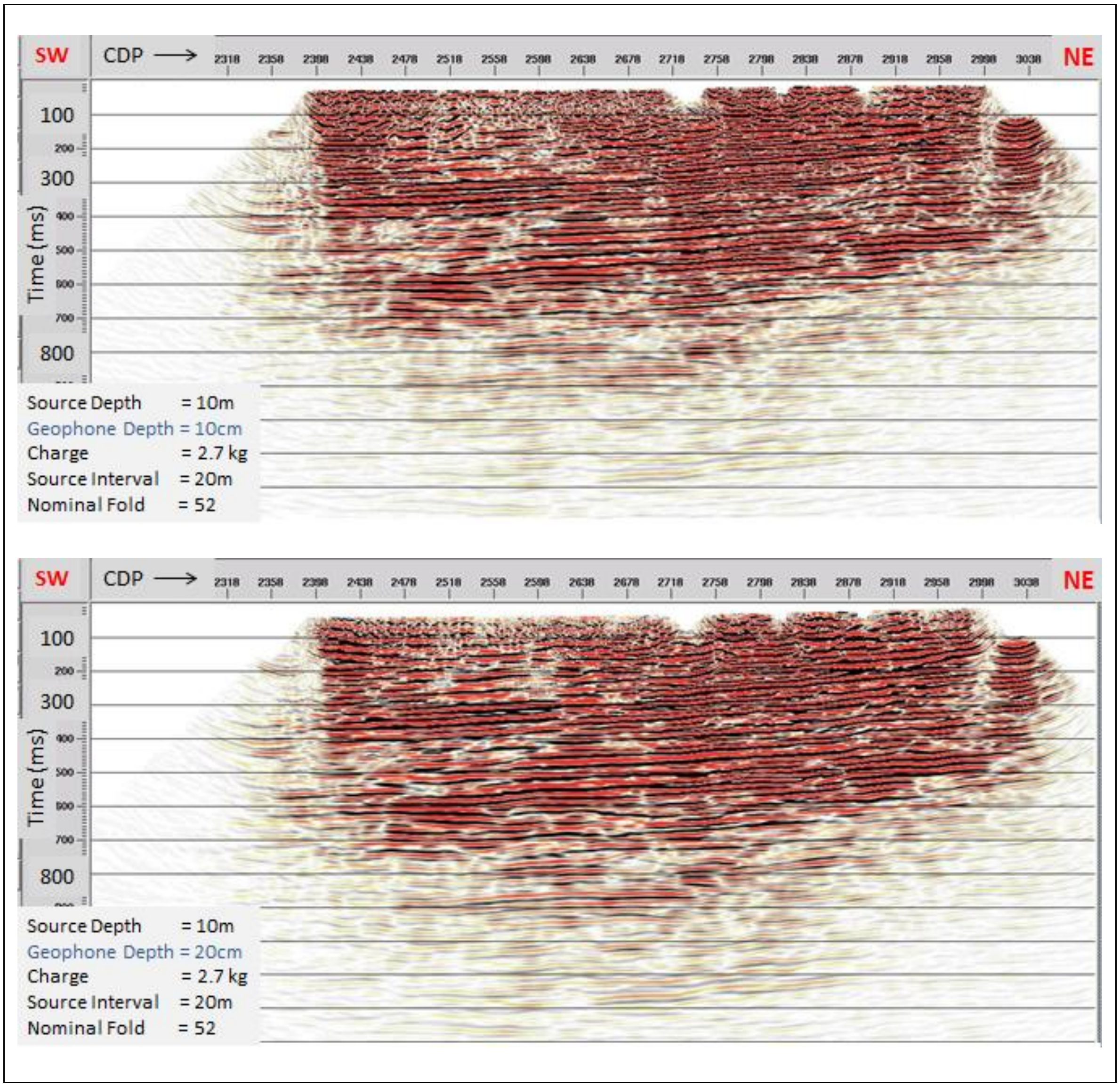

Figure 2.3 (cont.): Migrated stacks for the vertical channel (displayed with no gain) acquired with the different acquisition parameters. The acquisition parameters are described in the box in the bottom left corner.

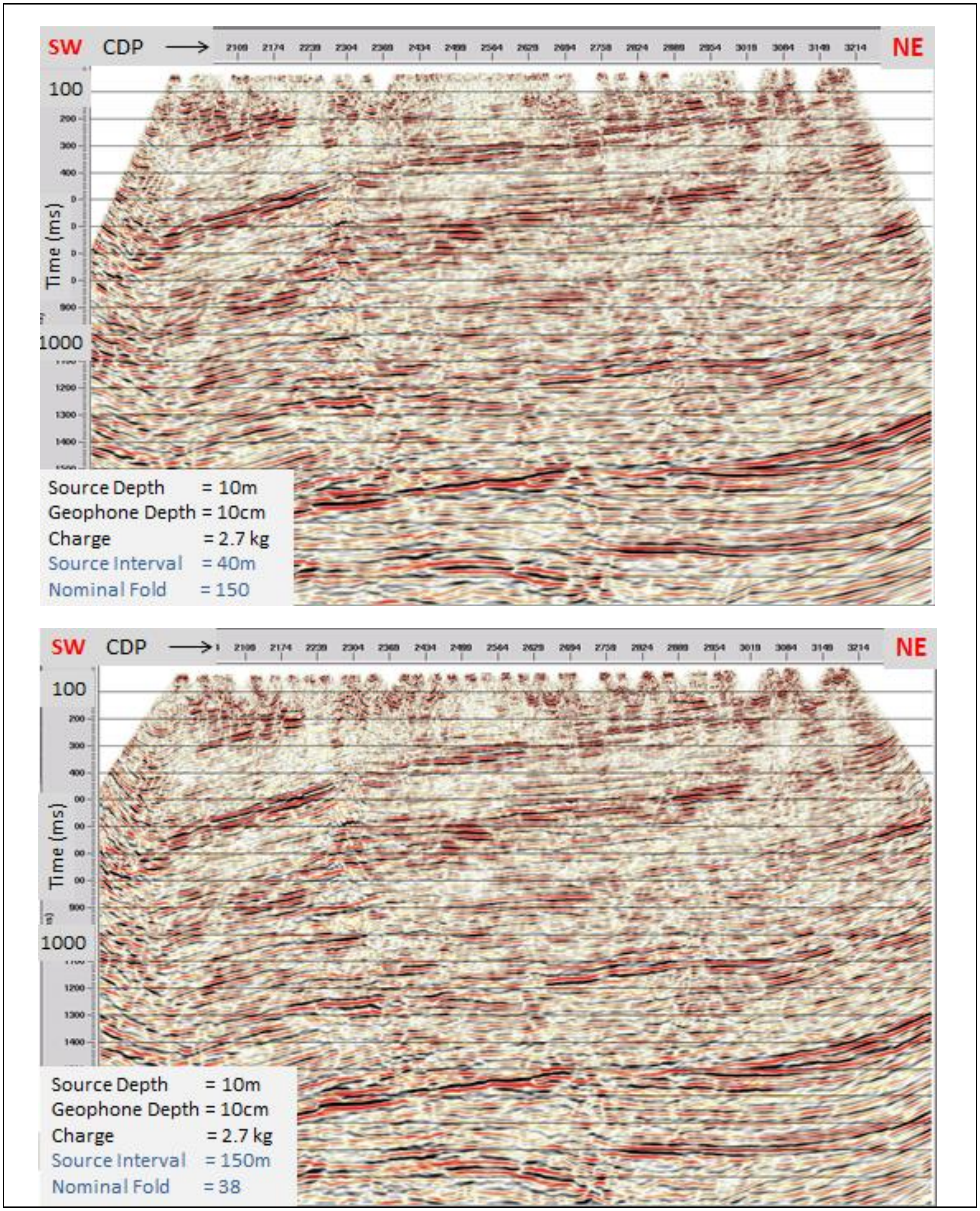

Figure 2.4: Migrated stacks for the vertical channel (displayed with post-process) acquired with the different acquisition parameters. The acquisition parameters are described in the box in the bottom left corner.

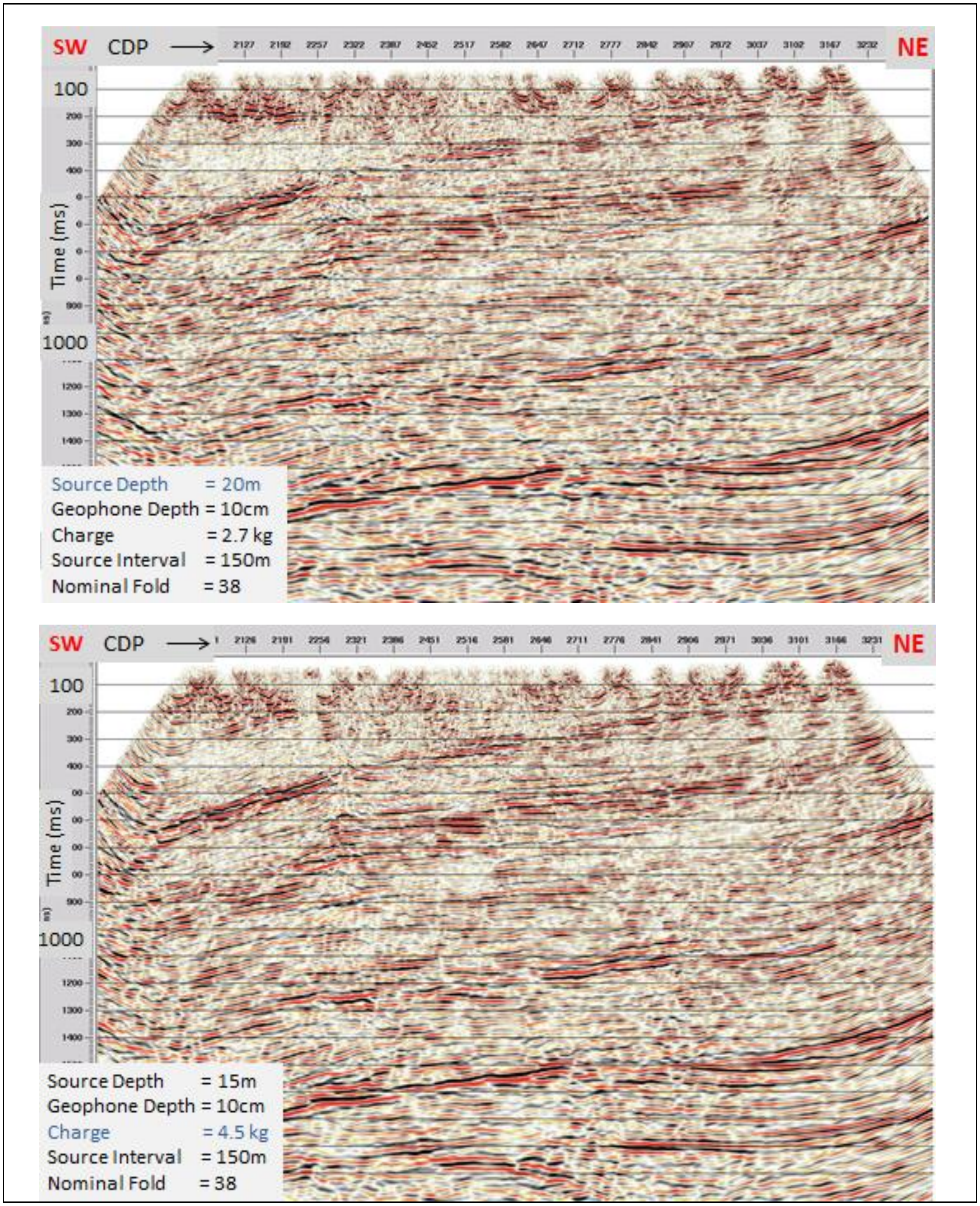

Figure 2.4 (cont.): Migrated stacks for the vertical channel (displayed with post-process) acquired with the different acquisition parameters. The acquisition parameters are described in the box in the bottom left corner.

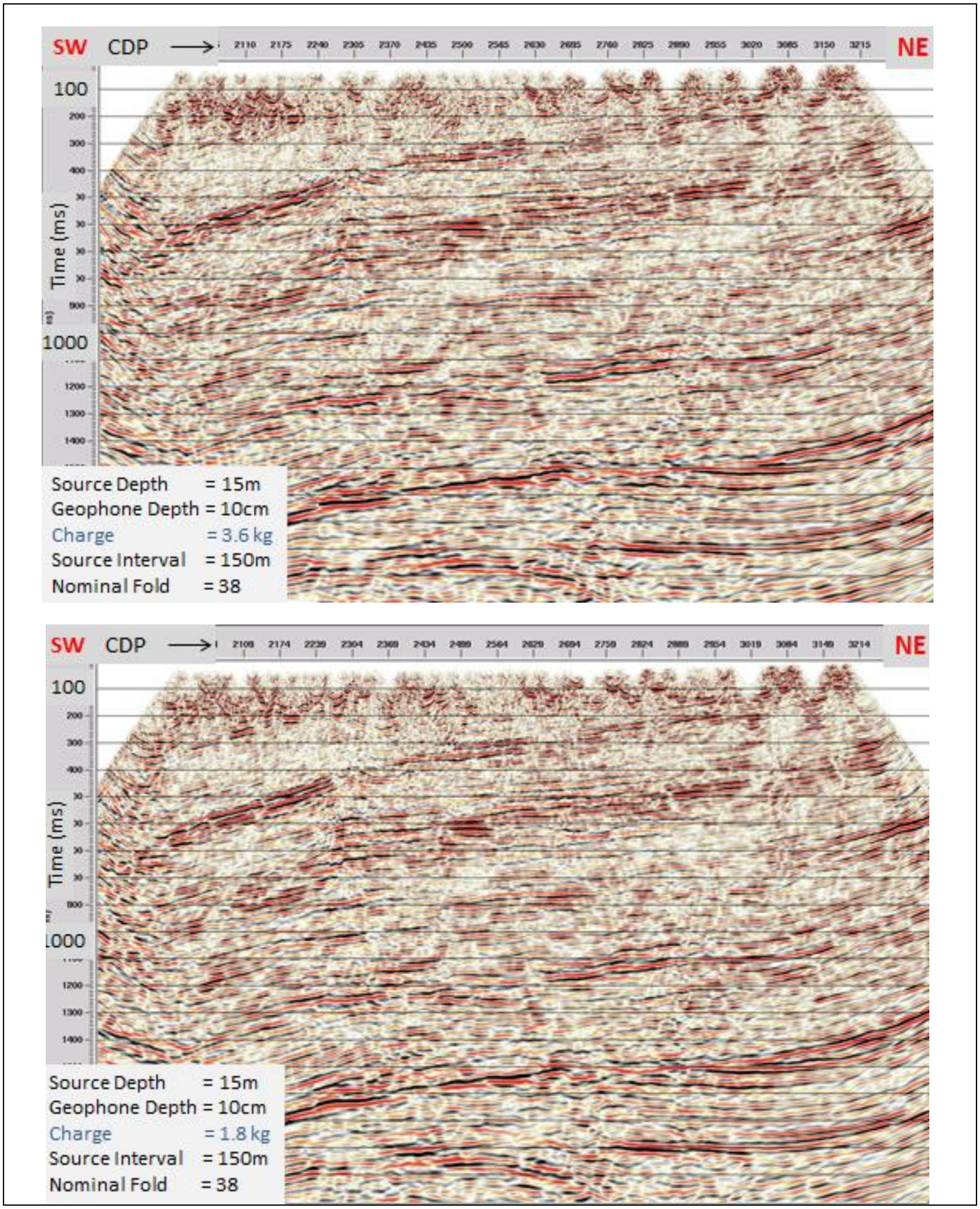

Figure 2.4 (cont.): Migrated stacks for the vertical channel (displayed with post-process) acquired with the different acquisition parameters. The acquisition parameters are described in the box in the bottom left corner.

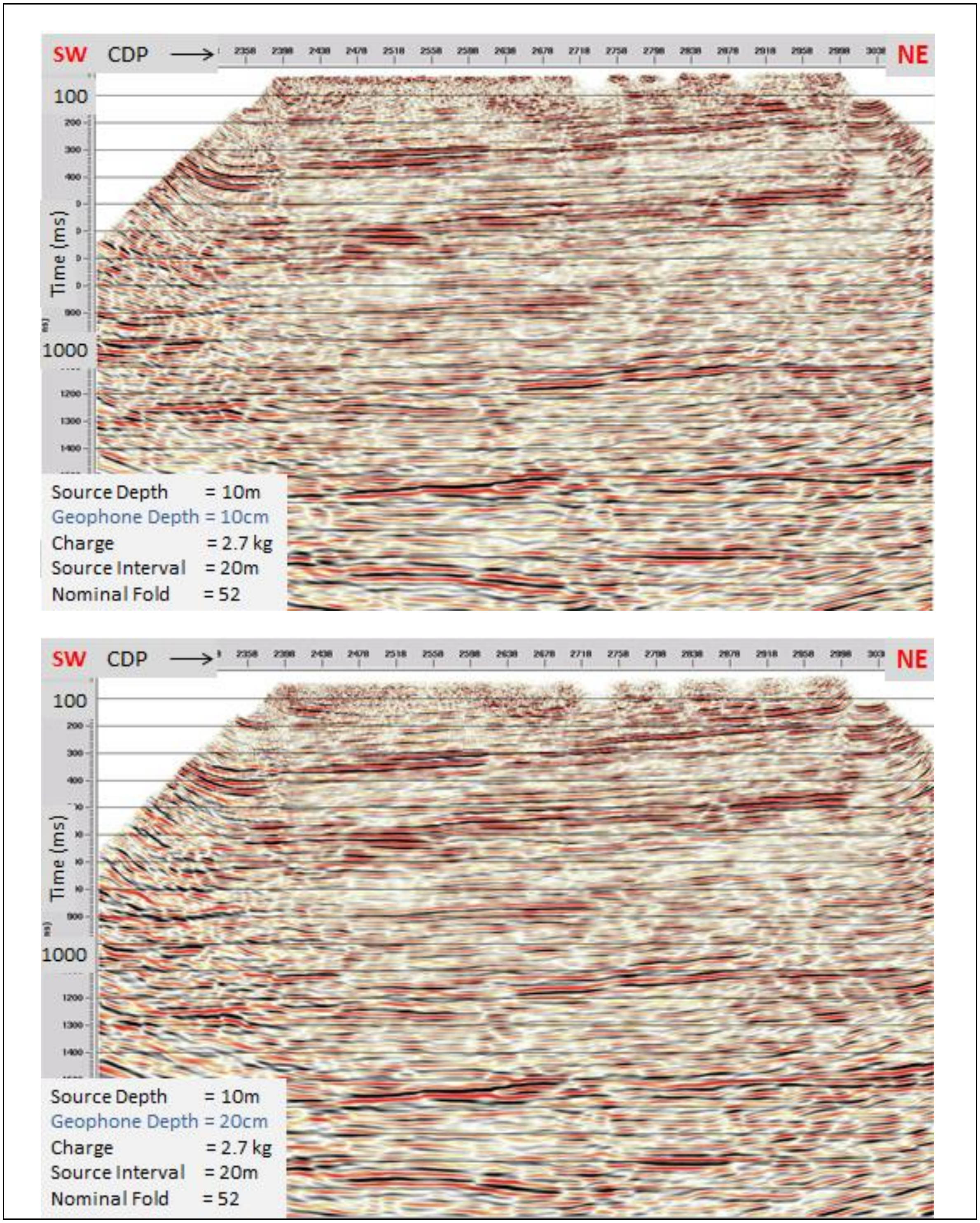

Figure 2.4 (cont.): Migrated stacks for the vertical channel (displayed with post-process) acquired with the different acquisition parameters. The acquisition parameters are described in the box in the bottom left corner.

Chapter 3: Survey 2D-3C: PS-waves

3.1 Acquisition

The PS-waves for the 2D-3C test lines were acquired at the same moment as the PP-waves. The same acquisition parameters were tested so they won't be described again in this section. For the processing stage some different considerations were made for converted-waves from PP-waves.

3.2 Processing

For converted-wave processing, the horizontal channels were used. As the geophones were already oriented with one horizontal component in the inline direction (radial component) and the other perpendicular (transverse component), no horizontal rotation was needed for geometry.

Figure 2.1 shows a random shot gather for the radial and transverse component. The difference in the reflectors' definition might be indicative of anisotropy in the media. As no good reflectors were observed in the transverse channel, only the radial component was processed to interpret converted-waves.

The processing steps for the radial channel are described below and stacks corresponding to fundamental steps in the sequence are shown in Appendix B.

- Polarity reversal

For the radial component positive and negative offsets have reverse polarities. So, polarities were reversed for negative offsets in every shot.

- Asymptotic binning

It is well known that for converted-waves the ray path is asymmetric as it is described by Snell's law: $sin\theta/Vp = sin\phi/Vs$, where θ and ϕ are the P- and S-wave angles of incidence and reflection respectively (Stewart et al., 2002). As it is shown in Figure 3.1, obtained from Stewart et al. (2002), conversion points at several depths can be adjusted by a hyperbola, in which case the binning is defined by its asymptote. Therefore the common depth point (CDP) for converted waves is named asymptotic conversion point (ACP). As it is expressed by Hardage (2011), the distance from the source to the asymptotic conversion point (ACP) can be expressed as:

$$X_{ACP} = \frac{X}{(1+[^1/_\gamma])}, \quad (1)$$

where X is the total offset (source-receiver distance), X_{ACP} is the distance from the source to the conversion point and γ the average value down to the reflector where the hyperbola is becoming almost asymptotic. For shallow interfaces this approximation is erroneous.

As the distance from the source to the ACP depends on γ, several values were tested for the asymptotic binning. A constant value of γ = 3 was selected, being the one that provided a less dispersive fold distribution (Figure 3.2). Also brute stacks were generated for every asymptotic binning and were used to confirm this selection.

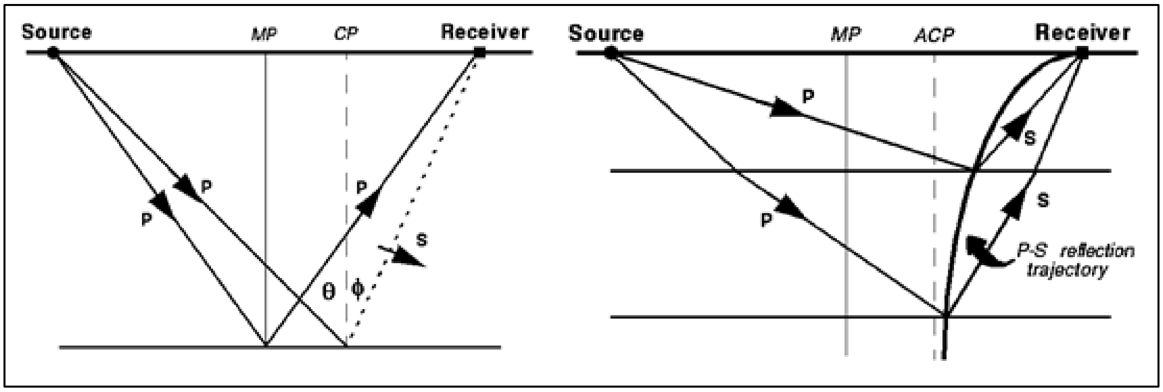

Figure 3.1: (left) Ray path of a PP- and PS-wave comparing the location of the reflection points related to each. (Right) Location of the PS-conversion points at reflectors at different depths. MP denotes the midpoint between the source and receiver, CP denotes the PS-wave conversion point and ACP denotes the asymptotic conversion point, determined by the hyperbola's asymptote (from Stewart et al., 2002).

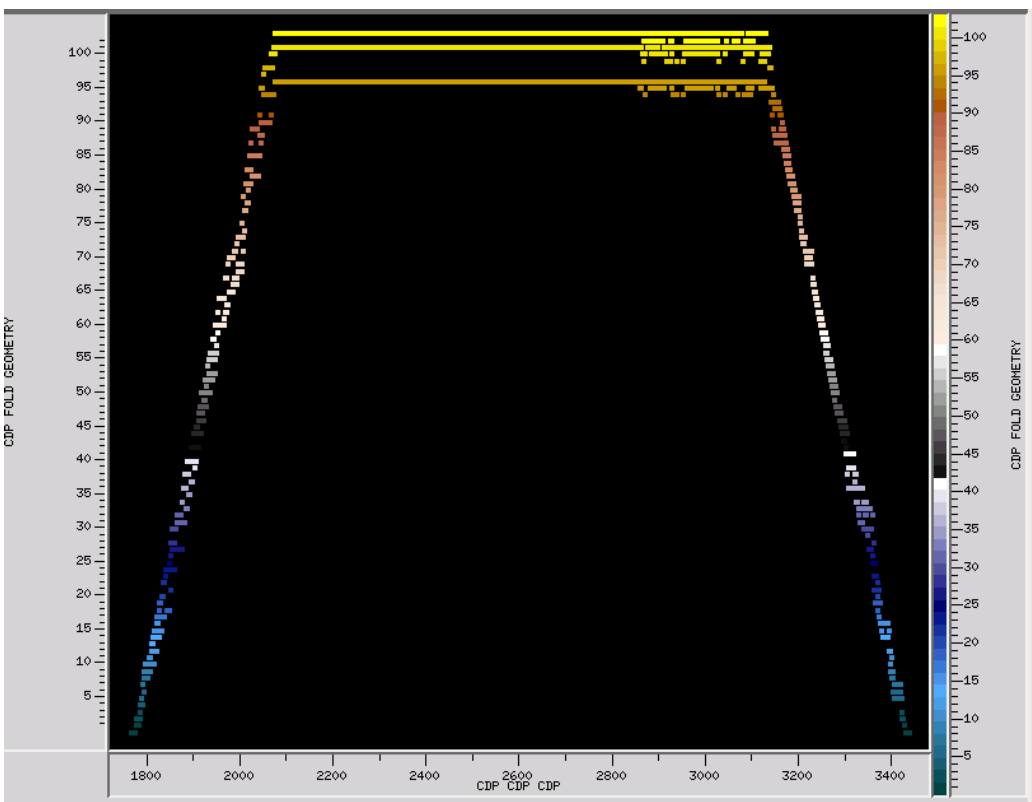

Figure 3.2: Fold distribution for an asymptotic binning with γ =3 (Line EXP-TEN-2D3C-1 - A1 shot configuration).

- Trace Editing and Noise Attenuation

After the geometry was applied, every shot record was controlled to identify noisy traces following the same criteria as for the vertical channel.

- Initial PS Velocity

For an initial estimation of the converted wave velocity, the PP-wave velocity was used. Average interval γ values varying with time obtained from the sonic logs have been used.

- Static Corrections

As the near surface is generally composed of a non-consolidated material (weathering), seismic velocities trough it are generally low, especially S-waves. S-wave statics may be two to ten times greater than P-wave statics at the same location (Tatham and McCormack, 1991).

Static corrections require both source and receiver components. For converted-waves, source statics are associated with P-waves' statics and receiver statics with S-waves. As it is usual to start with the PP processing, source statics were already computed. For receiver statics, there are several ways to calculate them.

Two methods for refraction static corrections proposed in the literature were tested in this dataset. The first one (easiest and fastest) implies computing PS refraction statics from PP refraction statics. Refraction statics are defined as:

$$CT = CT_I + CT_E \ , \qquad (2)$$

where CT is the total refraction static corrections, CT_I is the static correction for the incident wave and CT_E for the emergent wave. For the CT_I the P-wave source refraction static was used and, for the $CT_{E,}$ three times the P-wave receiver refraction static (the same γ value used for the asymptotic binning). But this method is considering a constant γ value in the near surface to determine static corrections which is not true. So, it would be useful to be able to use both P and SV refractions to determine weathering thickness and velocity.

A more laborious method proposed by Schafer (1991) consists in using the observed travel-times from S-wave refractions to determine a model of the near surface. So, based on this idea, the S-wave first breaks were picked and statics were computed using the delay time method with GLI (Generalized Linear Inversion) of Seismic Studio.

Figure 3.3 shows first break picks for S-wave refractions, the stacks computed with the two refraction statics methods discussed before and receiver and source statics profiles. After comparing results computed with both techniques, the second method was chosen, showing a better handle of statics particularly in the highlighted area.

For the source component, the PP-wave source statics were used. For the receiver component, statics corrections were calculated from the converted-wave first breaks. The converted-wave first arrivals were picked manually. The selected offset for refractor velocity calculation was 200-1200 m.

A one weathering layer model was chosen and a constant weathering velocity was used.

Model summary:

- One weathering layer model
- Weathering Velocity: 400 m/s
- FB picking offset: 200 – 1200 m
- Final Datum: 150 m
- Replacement Velocity: 750 m/s

- Pseudo-true Amplitude Recovery

As for the vertical channel, one of the first steps is to try to compensate for amplitude losses due to geometric spreading. The pseudo-true Amplitude Recovery curve was modeled with t^n, being

- Time-Power constant : 3
- Recovery Curve: 3 dB/s
- Application Length: 3000 ms.

- Surface consistent amplitude compensation

As for PP-waves, another edition by amplitudes was applied, rejecting anomalous ones. With the compensated amplitudes a surface consistent deconvolution was applied followed by a new air blast attenuation (ABA).

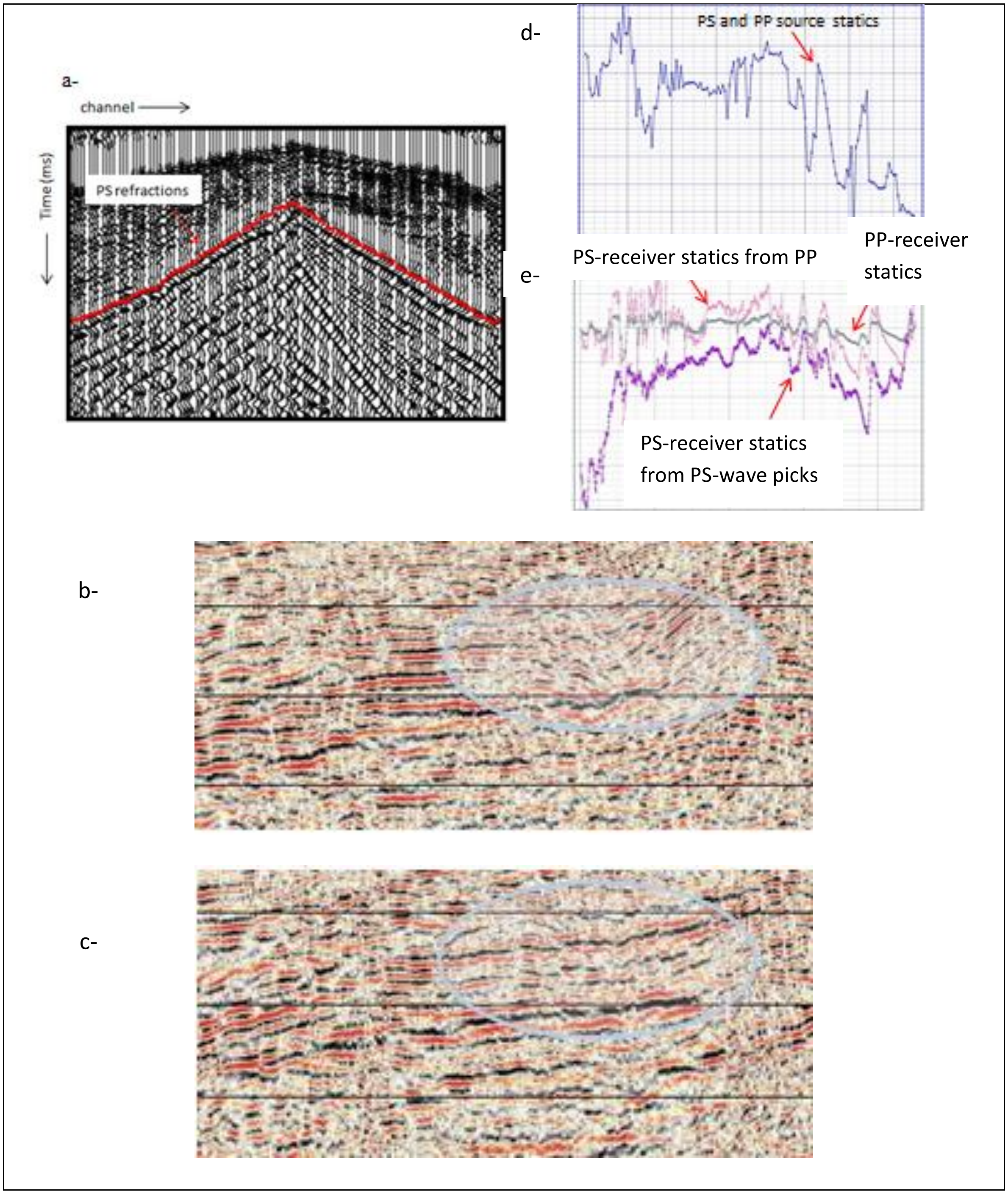

Figure 3.3: (a) First breaks picks for S-wave refractions with Seismic Studio. Stack with statics computed from (b) PP-waves and (c) from PS-waves refractions. (d) PP- (and PS-) source statics. (e) PP-receiver statics (grey), PS-receiver statics calculated from first S-wave breaks (purple), from three times PP-receiver statics (pink).

- Surface Consistent Deconvolution

Different operator lengths were tested both for spiking and predictive deconvolution. For the predictive deconvolution also different predictive distances were tested.

After comparing the results, the selected parameters for the deconvolution were the following, basing the decision in the continuity of events and resolution.

  - Type: Surface consistent spiking deconvolution
  - Operator length: 240 ms
  - White noise: 0.1%
  - Components: Source, receiver, and offset

- Velocity Analysis

When dealing with converted-waves, velocity may be offset dependent, particularly when there is a huge horizontal lithographic change (Hardage et. al., 2011). To make sure any possible lateral lithographic contrast was treated properly, from this stage onwards, positive and negative offsets were analyzed separately. Independent semblances, dynamic stacks and constant velocity stacks were created for only positive and negative offsets. These were used for velocity picking.

For both sets, velocity analyses were performed every 1000 m before first residual statics calculation, and every 500 m after the first residual static. Figure 3.4 shows a comparison between semblances generated without offset discrimination, with only positive offsets and only negative offsets. Even though along this 2D line not great lateral lithographic variations were observed, offset separation provided cleaner semblances and dynamic stacks and also increased the frequency content.

- Residual Static Corrections

Such as for the vertical channel, after the first velocity analysis, residual statics were computed with the program Maximum Power Autostatics (Ronen and Claerbout, 1985).

These static corrections are surface consistent with an analysis window width of 800 ms centered in a hand-picked horizon that followed the structural trend and a smash of 11. After the second velocity analysis, a second pass of Maximum Power Autostatics was run with the same parameters, diminishing dispersion.

- Structural Filter

Lumina Geophysical's structural filter described above was applied to the gathers to improve Signal/Noise and strengthen the coherency of linear events.

- F-XY Decon Pre-stack

Another noise attenuation technique used was F-XY Decon pre-stack, for which a pseudo 3D was built using shot records as in-lines and channels as cross-lines.

Selected Parameters:

- Number of in-lines: 3
- Number of X-lines: 9
- Operator length: 250 ms

- Frequency range: 5-250 Hz

- Trim Statics

After F-XY Decon pre-stack, trim statics were applied to the gathers to improve the coherency of events. The chosen parameters for trim statics were:

  - Statics maximum shift: 6ms.
  - Minimum number of live samples in window : 15%

- Stretch mute tests

Stretch mute values of 10%, 20%, 30%, 40%, 50%, 60%, and 70% were tested for stacking. A stretch mute of 50% was chosen, following the same criteria as in the vertical channel, providing a contribution of a maximum offset of 7500 m.

- Converted-wave DMO

According to Harrison (1992), in areas of considerable structure it is desirable to perform dip moveout (DMO) on pre-stack data to reduce the attenuation of dipping events. It is well known that in PP-waves processing, when dipping reflectors are present in the subsurface, some difficulties in reflection-point smearing and changes in the apparent stacking velocity are encountered (Levin, 1971). For PS-waves, the reflection-point imaging is asymmetric even for zero-dip events; leading to the need of an asymmetric DMO operator.

Levin (1971) presented that for dipping reflectors, at non-zero offsets, the reflection point is moved from the midpoint creating some data smearing. This smearing generates an increase in the apparent stacking velocity needed to flatten the events given by:

$$V_{app} = \frac{V}{\cos\theta}, \tag{3}$$

where V_{app} is the apparent velocity, V the true medium velocity, and θ the interface's dip. If for any two-way time and common-midpoint location more than one dip is present, only one of them will be optimally stacked causing an attenuation of the dipping reflector. Post-stack migration won't solve this issue as it assumes zero-offset data so we approach the problem with DMO.

Promax® converted-wave DMO applies a time-domain DMO to the input gathers moving the data samples horizontally to the proper conversion points. This module is based on the equation proposed by Harrison (1992):

$$\tau^2 = \frac{(h^2 - x^2)}{[\alpha^2(h-x) + \beta^2(h+x)]}\left(\frac{[\alpha^2(h-x_0) + \beta^2(h+x_0)]}{(h^2 - {x_0}^2)} t_n^2 + (x - x_0)(\alpha^2 - \beta^2)\left(\frac{\alpha+\beta}{\alpha\beta}\right)^2\right), \tag{4}$$

where x_0 is the midpoint offset of the zero-dip conversion point, and α and β are the average P and S wave velocities down to time t_n (obtained from Promax® tutorial; detailed explanation of the expression's development can be found in Harrison, 1992).

Converted-wave DMO was applied for both positive and negative offsets gathers using an average RMS velocity picked for each set.

After DMO, a residual NMO correction may still be needed. Thus, a new semblance (every 500 m) was created to do the residual velocity analysis. A new run of converted-wave DMO was run with the updated velocity field.

- Post-process

The following post-stack process was applied:

- Trace mixing
- F-X Decon
- Bandpass filter
- AGC (1000 ms)

3.3 Results

The same processing sequence was applied to the radial channel for both lines acquired with the several acquisition parameters. In this section, raw shot gathers and migrated stacks for the radial channel for the different acquisition tests are shown (Figures 3.5, 3.6 and 3.7).

In line EXP-TEN-2D3C-1 the geophone's depth was of 10 cm and in line EXP-TEN-2D3C-2 of 20 cm. As it was mentioned in the previous chapter A1 shots were exploded with a 40 m spacing, while for A2 – A5 shots spacing was ~150 m. To make a fair comparison about the charge size and depth, A1 was decimated to make its fold consistent with A2 – A5. Figure 3.6 displays the stacks no post-process as the intention is to observe if there are amplitude differences due to the different source depths and amount of charge.

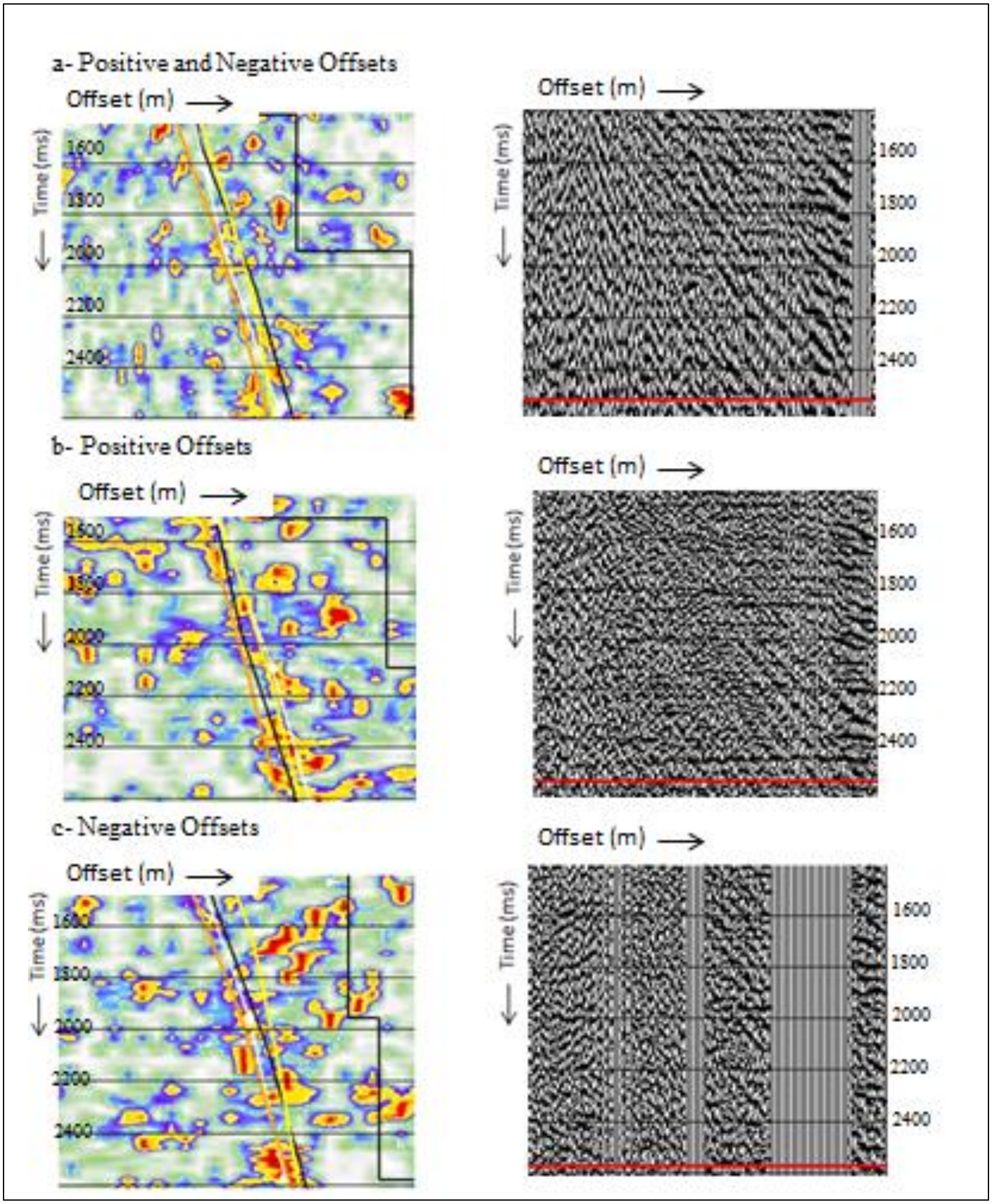

Figure 3.4: (a) Semblance and dynamic stack for positive and negative offset. (b) Semblance and Dynamic Stack for positive offset. (c) Semblance and dynamic stack for negative offset.

3.4 Comments

When comparing the migrated sections in Figures 3.6 and 3.7, we observe that there is a huge improvement in the whole section when comparing A1 decimated version with A1 with all the shots. As expected, more shots along the line will provide a better quality stack. This was not observed in the vertical channel. To analyze the influence of the amount of charge A2, A3, and A4 configurations should be compared. A2 was shot with a charge size of 1800 g, A3 with 3600 g and A4 with 4500 g. A4 is the best providing more energetic deeper reflectors and improving the continuity of the events. For conclusions about the source depth A1 (decimated version) and A5 must be compared as both were shot with the same amount of charge (2700 g) and depths of 10m and 20m respectively. A huge improvement in the signal/noise is observed with deeper sources. Deeper geophones provide a slightly better continuity of events, but the main improvement is related to more fold, as well as deeper and bigger sources.

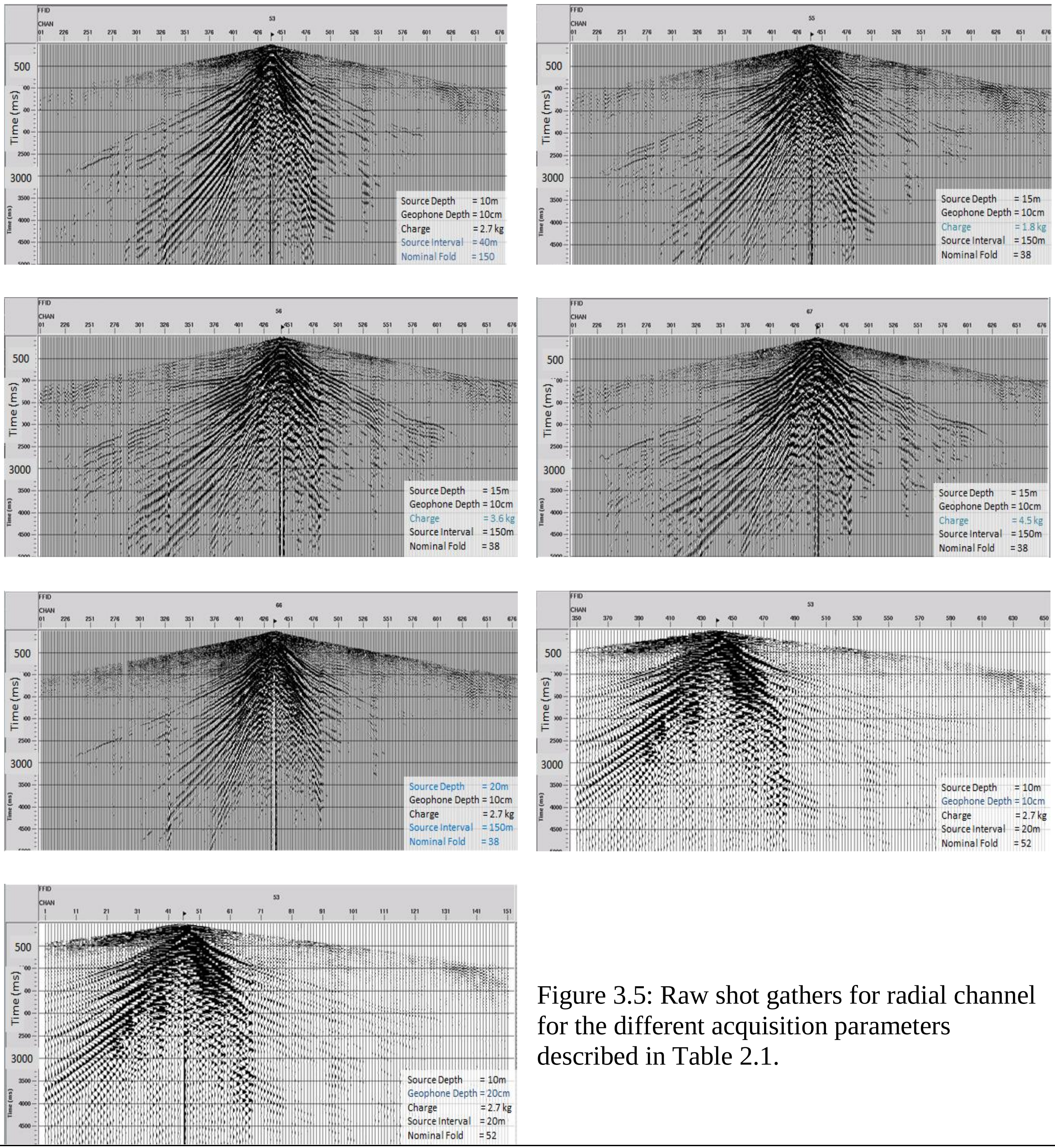

Figure 3.5: Raw shot gathers for radial channel for the different acquisition parameters described in Table 2.1.

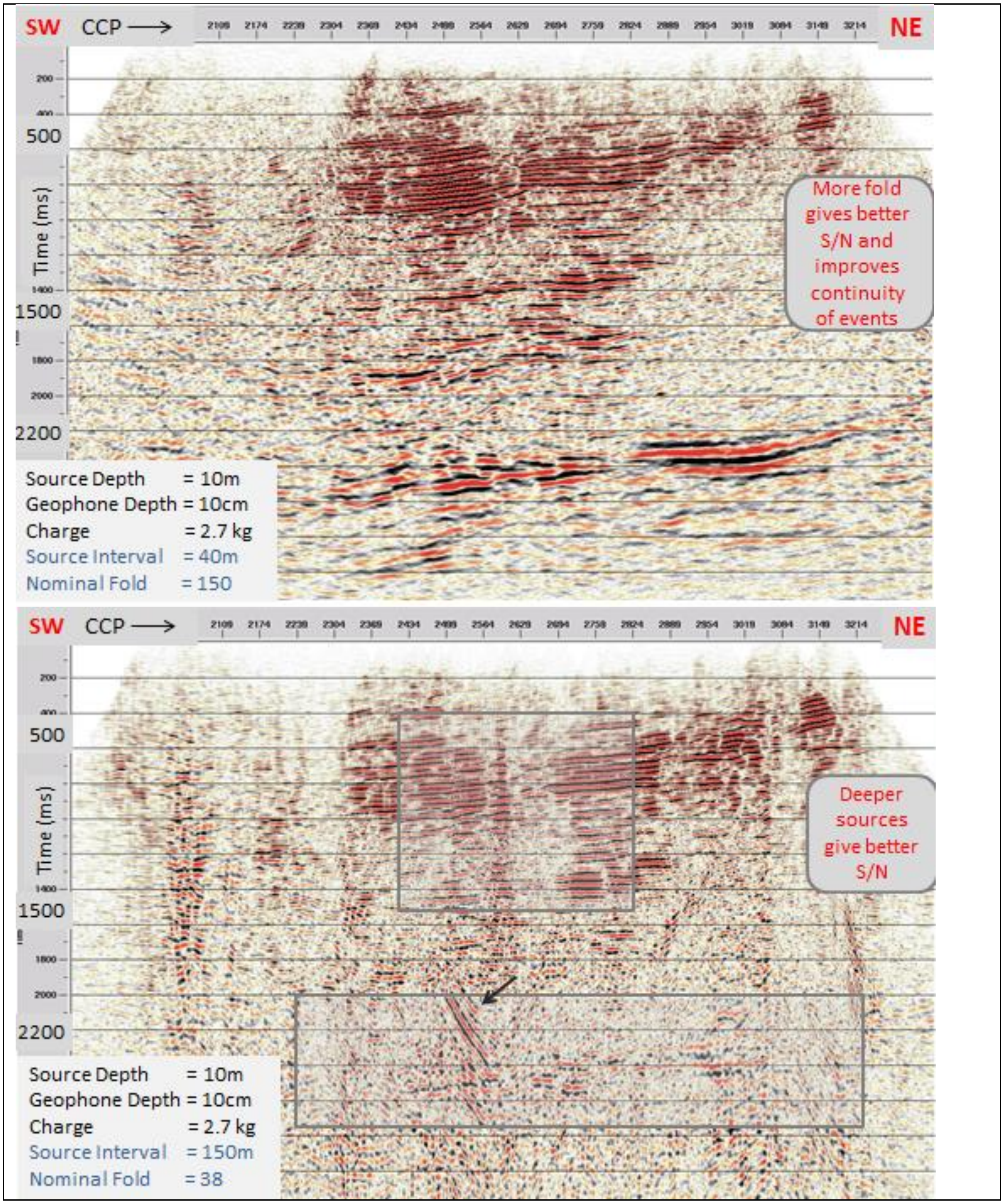

Figure 3.6: Migrated Stacks for the radial channel (displayed with no gain) acquired with the different acquisition parameters. The acquisition parameters are described in the box in the bottom left corner.

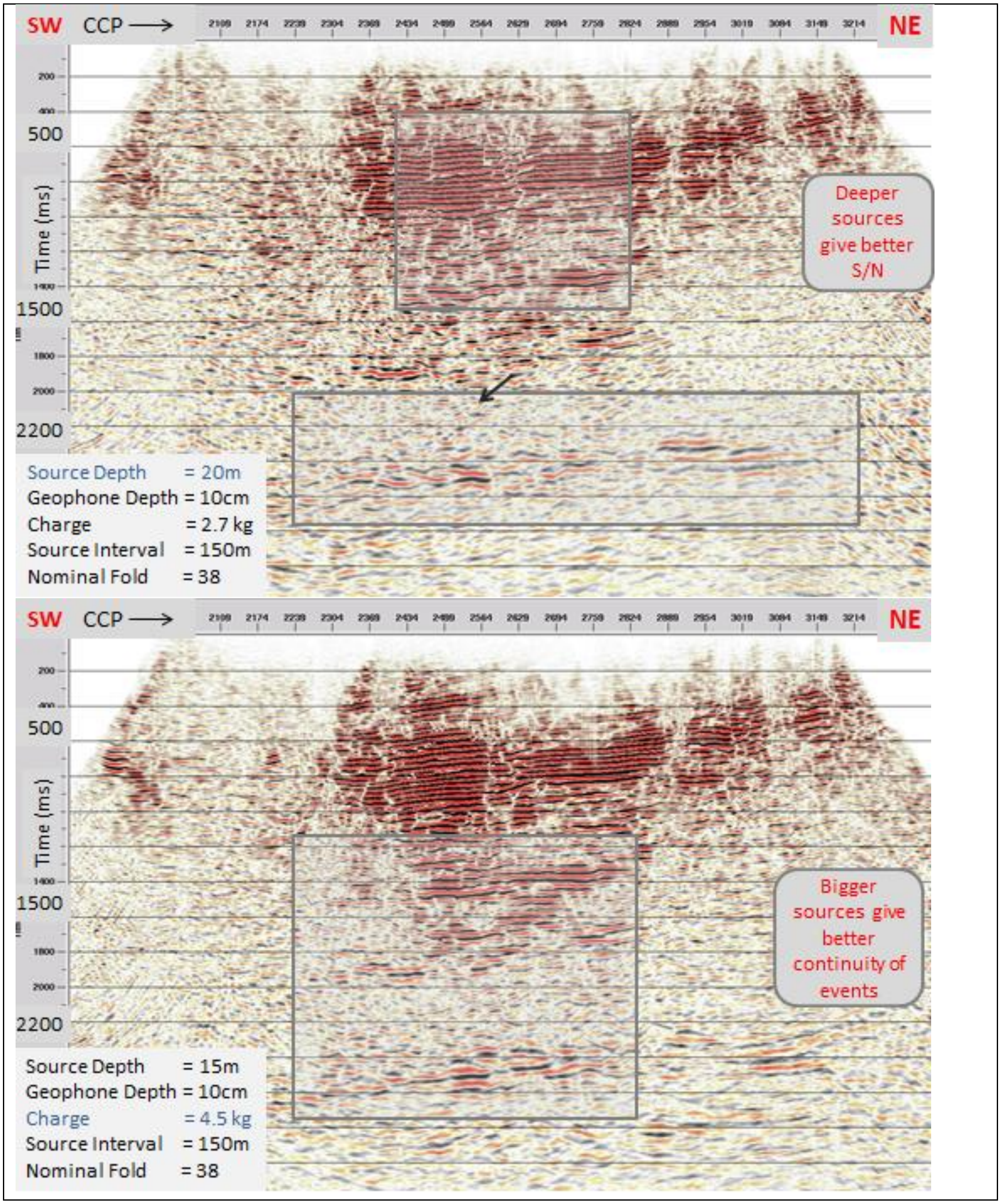

Figure 3.6 (cont.): Migrated Stacks for the radial channel (displayed with no gain) acquired with the different acquisition parameters. The acquisition parameters are described in the box in the bottom left corner.

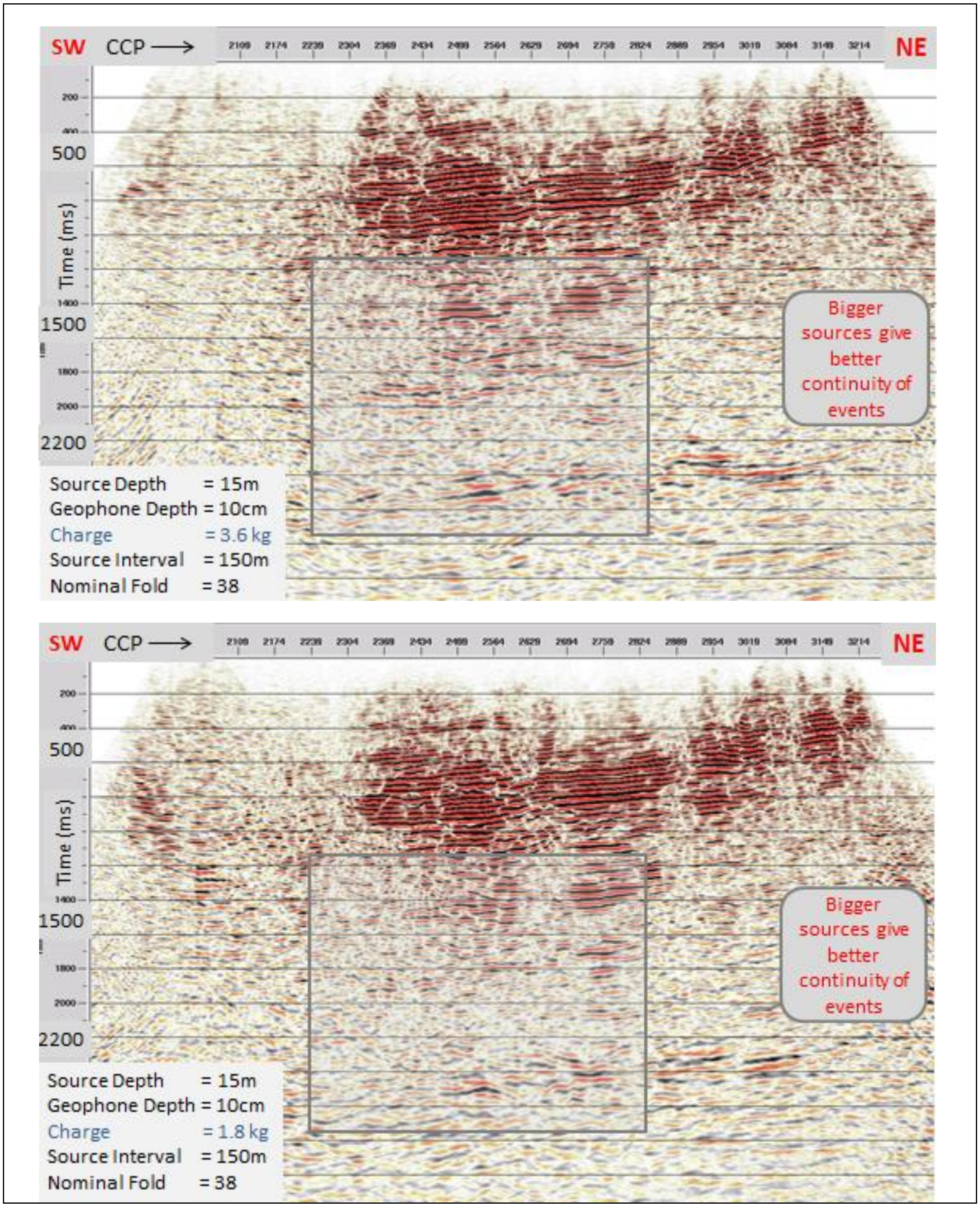

Figure 3.6 (cont.): Migrated Stacks for the radial channel (displayed with no gain) acquired with the different acquisition parameters. The acquisition parameters are described in the box in the bottom left corner.

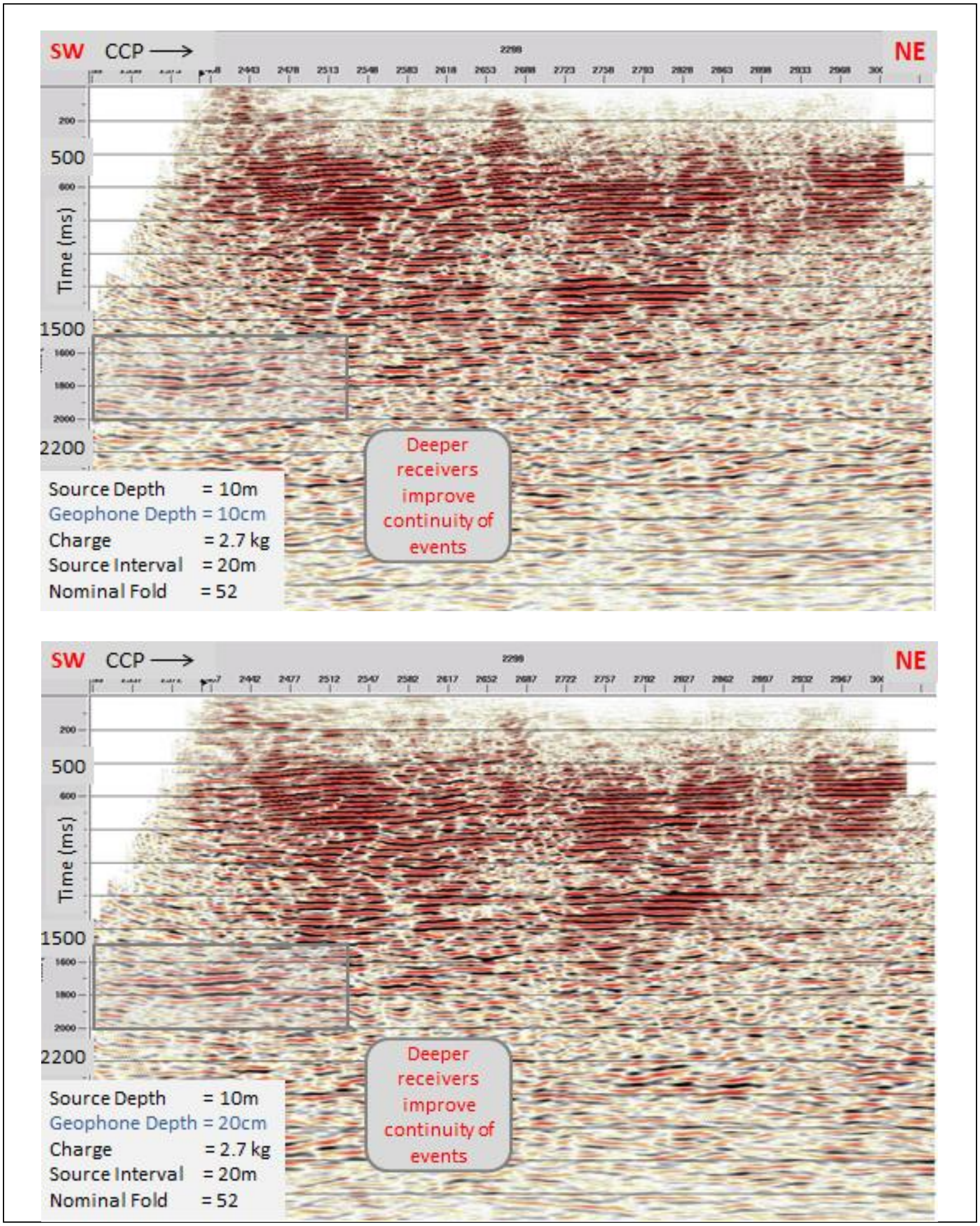

Figure 3.6 (cont): Migrated Stacks for the radial channel (displayed with no gain) acquired with the different acquisition parameters. The acquisition parameters are described in the box in the bottom left corner.

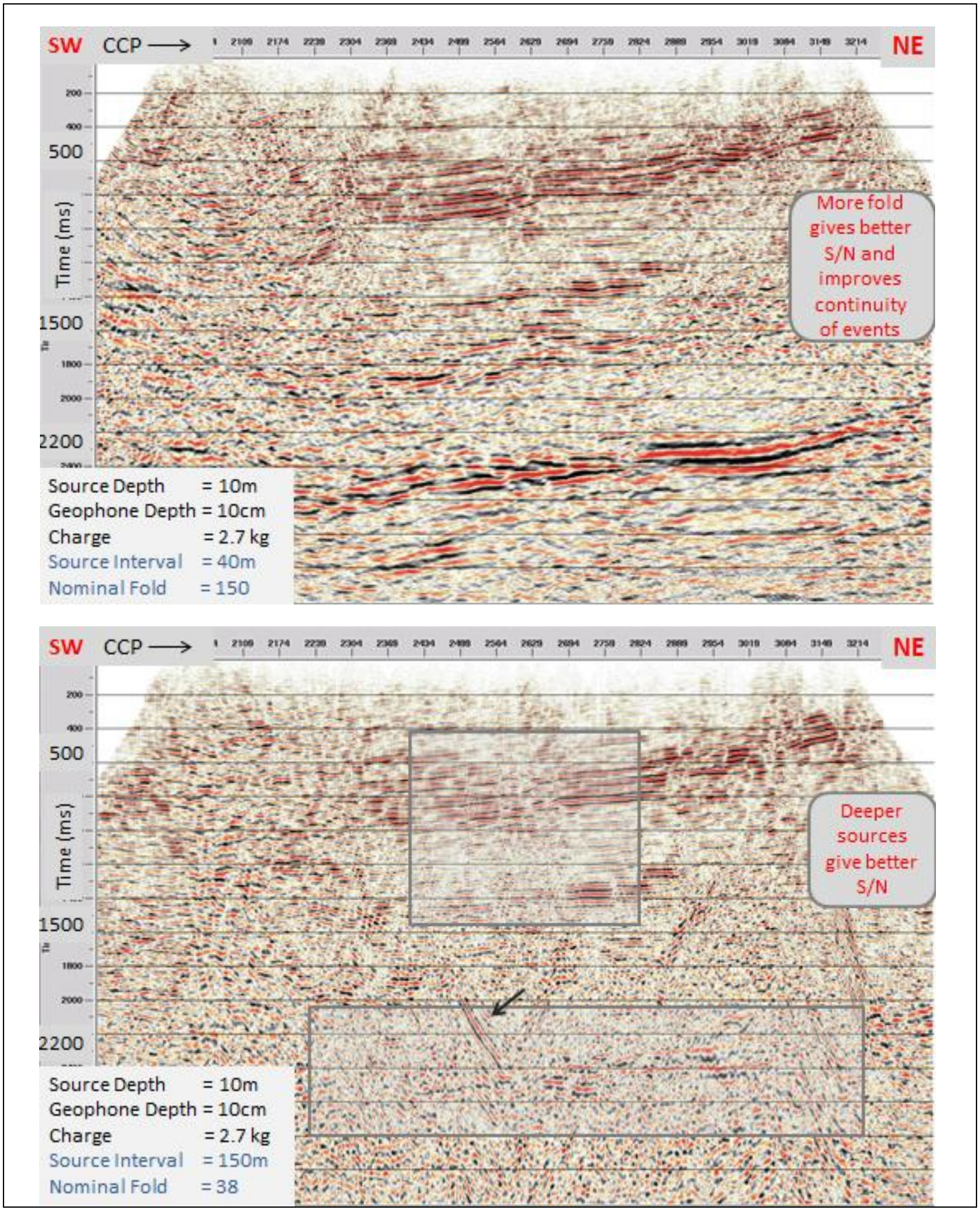

Figure 3.7: Migrated Stacks for the radial channel (displayed with post-process) acquired with the different acquisition parameters. The acquisition parameters are described in the box in the bottom left corner.

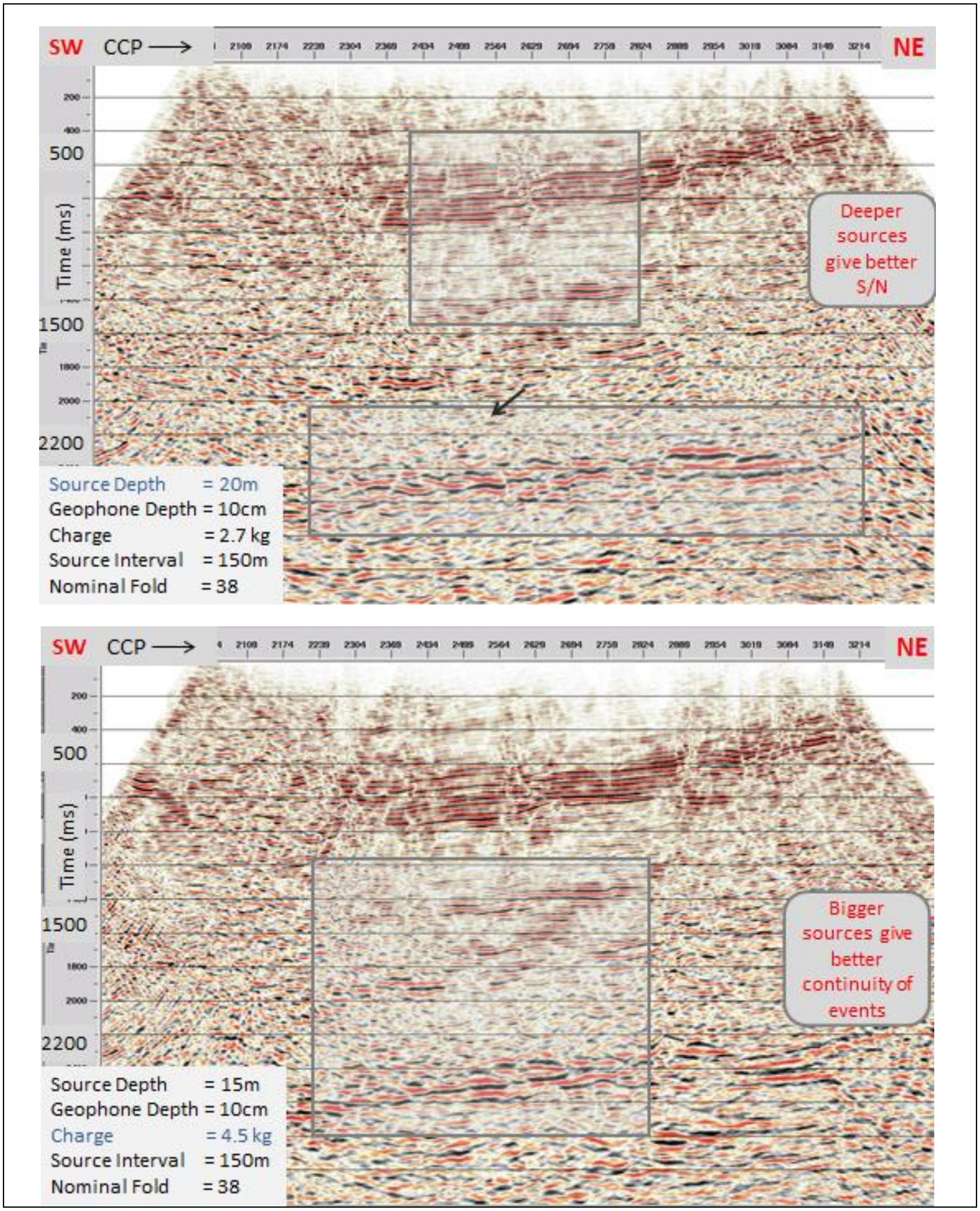

Figure 3.7 (cont.): Migrated Stacks for the radial channel (displayed with post-process) acquired with the different acquisition parameters. The acquisition parameters are described in the box in the bottom left corner.

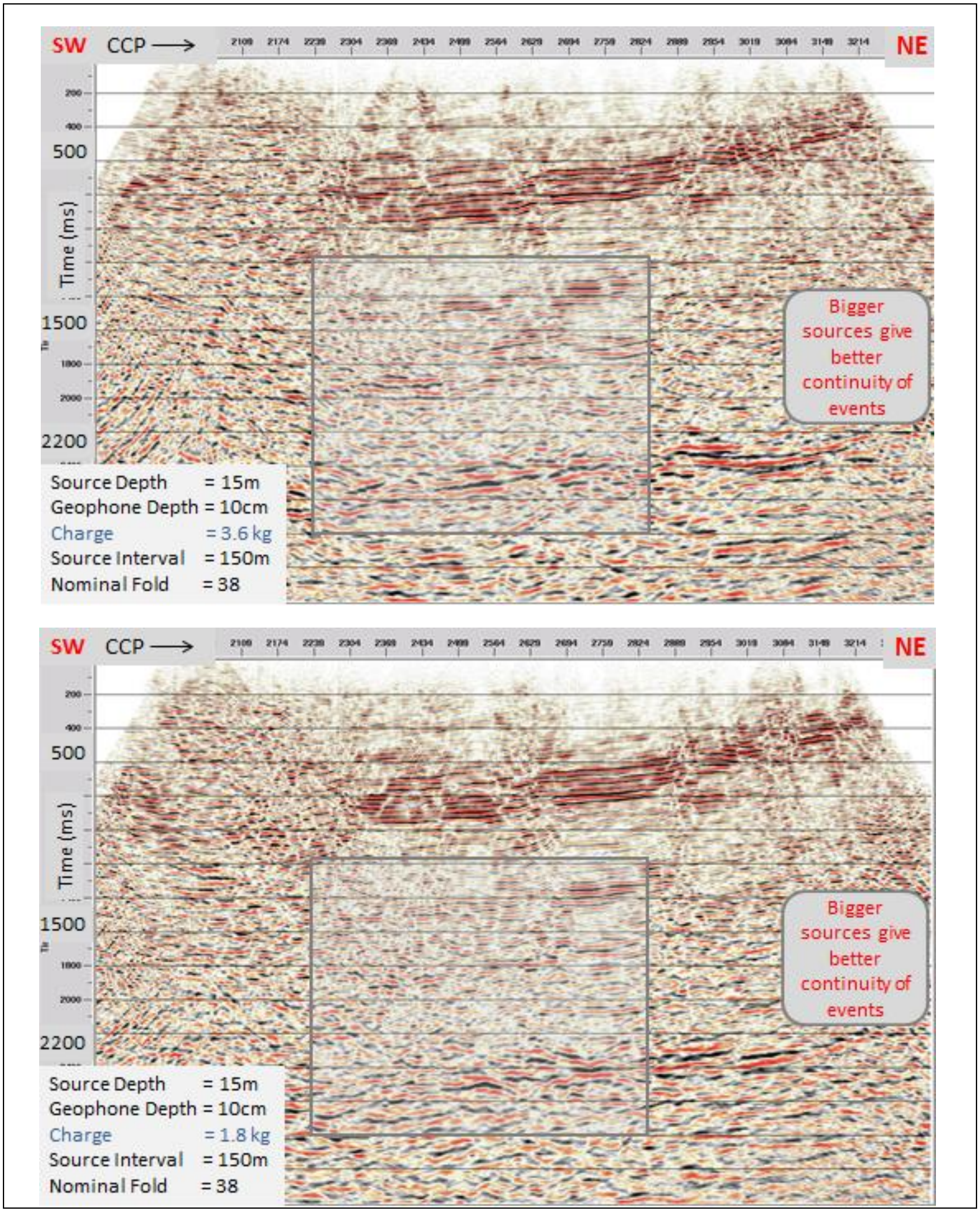

Figure 3.7 (cont.): Migrated Stacks for the radial channel (displayed with post-process) acquired with the different acquisition parameters. The acquisition parameters are described in the box in the bottom left corner.

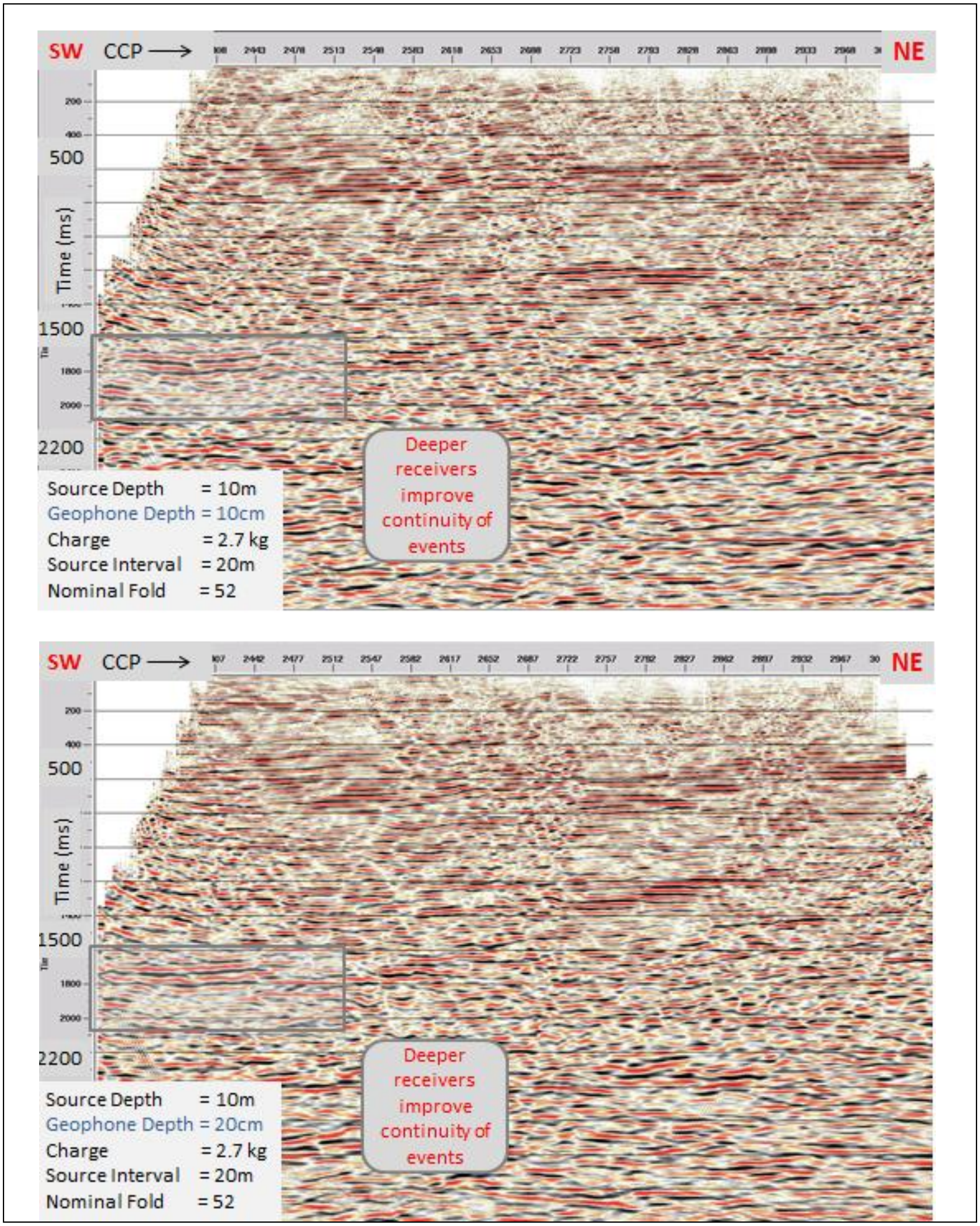

Figure 3.7 (cont.): Migrated Stacks for the radial channel (displayed with post-process) acquired with the different acquisition parameters. The acquisition parameters are described in the box in the bottom left corner.

Chapter 4: Interpretation

The aim of this case-study was to image the reservoir units within the Mugrosa Formation in the Tenerife Field, located in the Middle Magdalena Valley (Colombia). This sequence is composed of medium-grained sandstones (usually from 2 to 5 m thick) interbedded with mudstones. Due to the meandering river depositional environment, the sand bodies can extend to 30 m thick.

As it was mentioned above, the available data used for the interpretation included two 2D-3C test lines, PP- and PS-migrated volumes for the Tenerife-3D-3C survey, well logs and VSP from three wells in the field (Tenerife-1, -2 and -3).

The common logs between the three wells were SP and resistivity. In addition, sonic, Gamma Ray (GR), caliper, and Vp/Vs logs were provided for Tenerife-1; and sonic, GR, and Vp/Vs logs for Tenerife-2. Figure 4.1 shows the available logs for the three wells with the Mugrosa-C Formation marked with a straight line across them.

4.1 VSP

3C-Offset VSP corresponding to wells Tenerife-1 and -2 were processed by Schlumberger (Figures 4.2 and 4.3). This allowed an accurate time-depth conversion and, therefore, a good identification of the horizons to interpret in the seismic volumes.

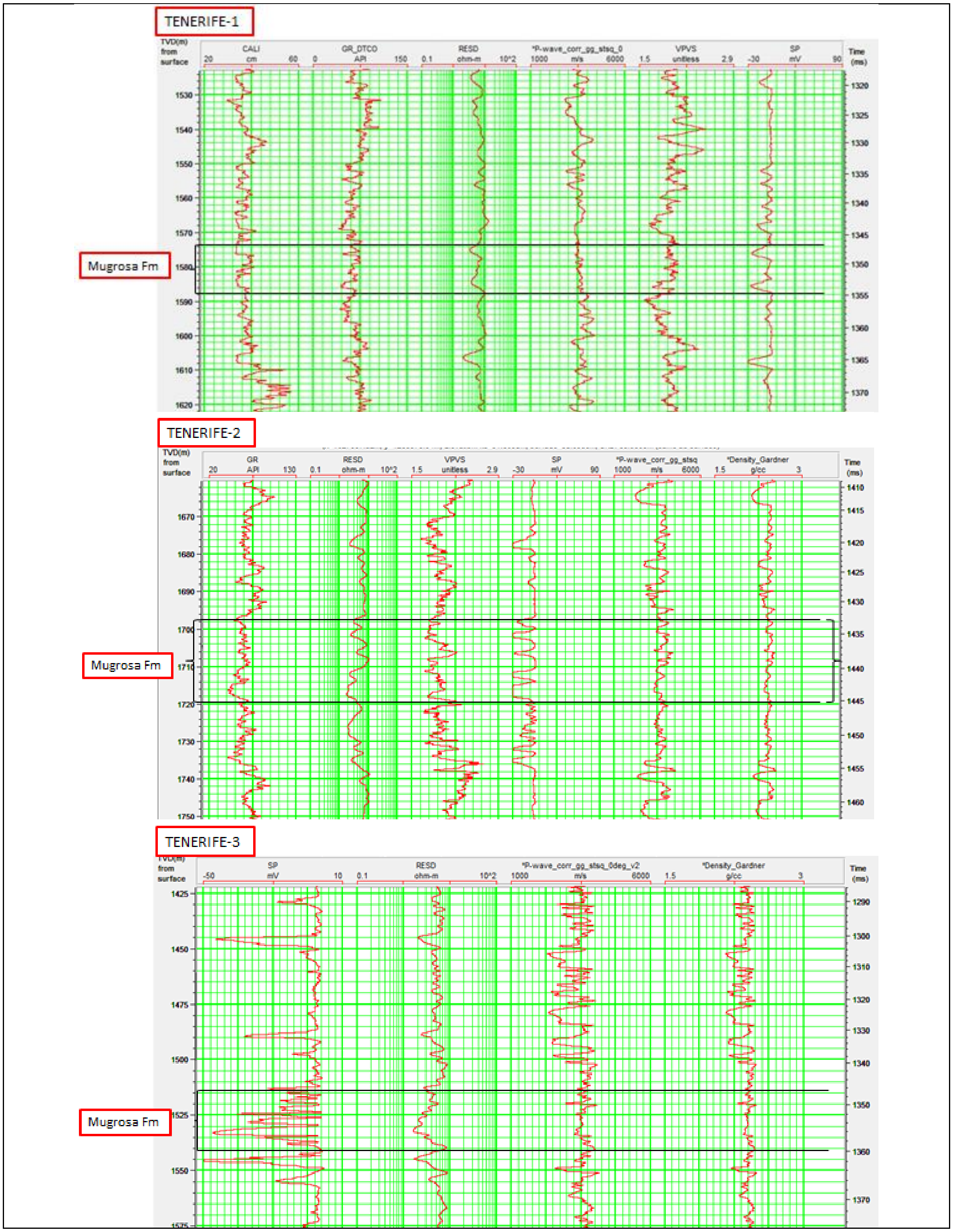

Figure 4.1: Available logs for Tenerife-1, -2 and -3. The Mugrosa-C Formation is marked with a black line across the logs.

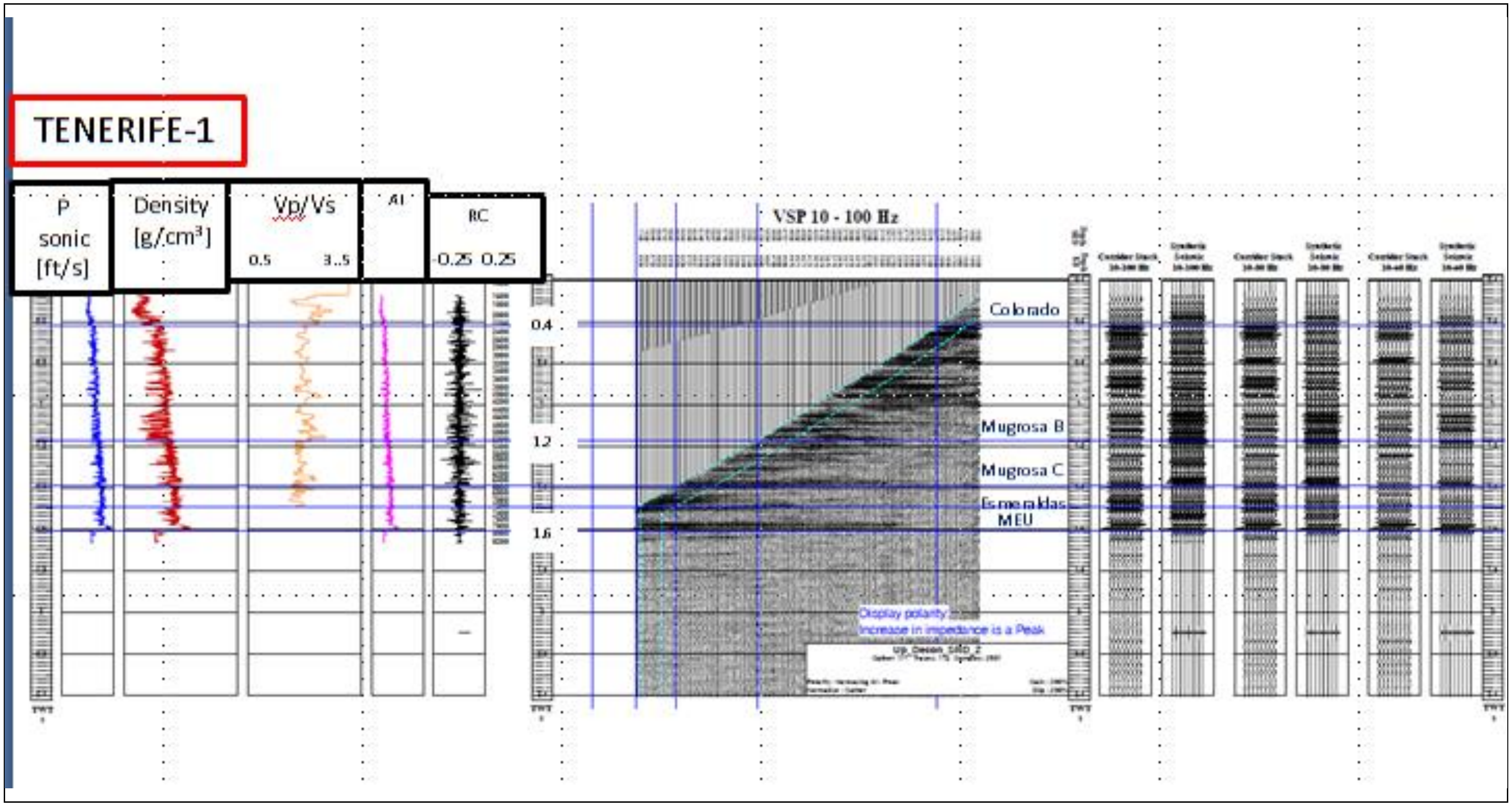

Figure 4.2: Processed VSP for Tenerife-1, showing the tops of the Colorado, Mugrosa-B and -C, Esmeraldas and Middle-Eocene Unconformity (MEU).

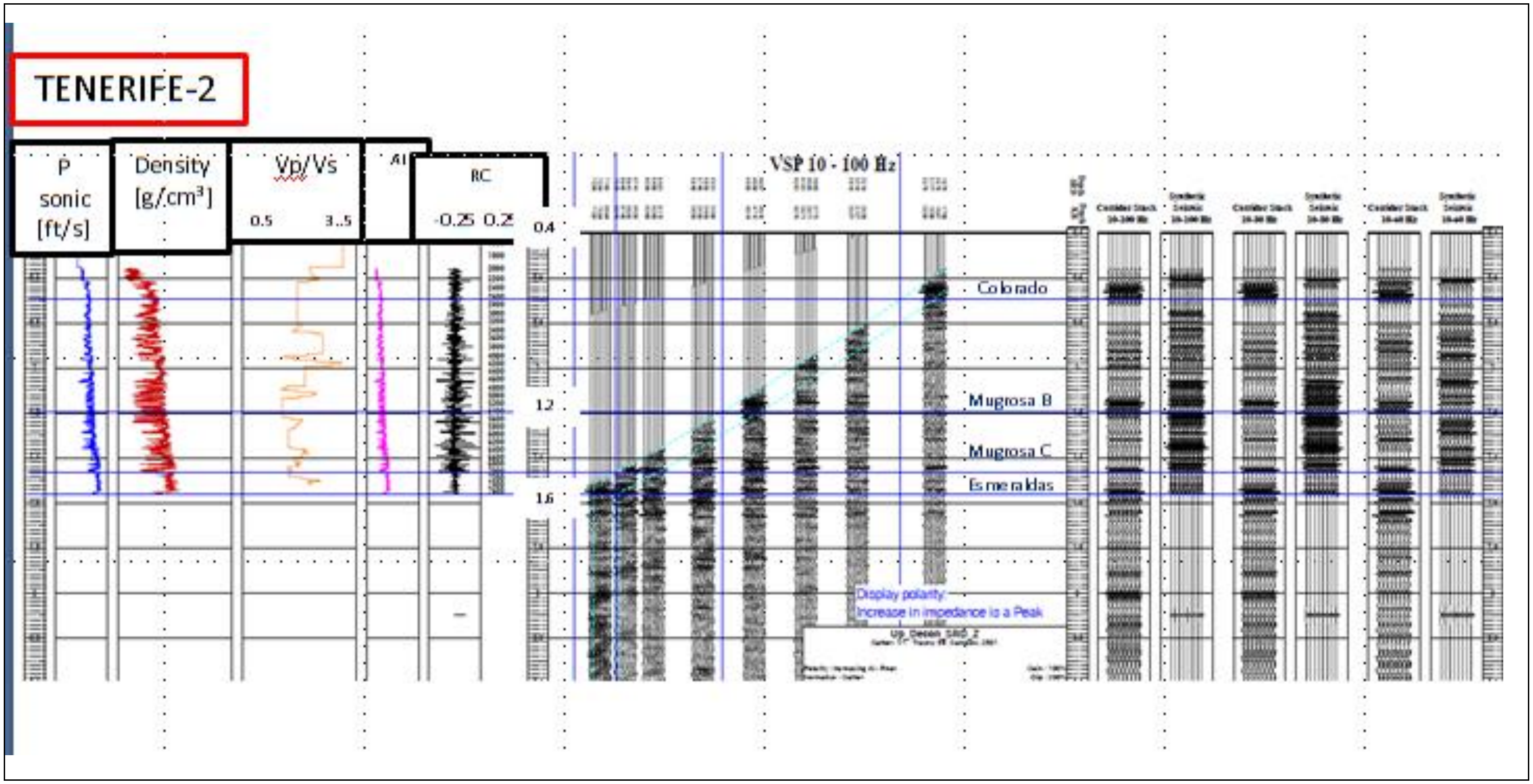

Figure 4.3: Processed VSP for Tenerife-2, showing the tops of the Colorado, Mugrosa-B and -C, Esmeraldas and Middle-Eocene Unconformity (MEU).

4.2 Cross-plots analysis

Cross-plots of Vp, Vs, Vp/Vs, GR, and Resistivity logs were expected to provide a good lithology discrimination and possible hydrocarbon saturation. S-wave sonic logs were measured in a certain interval covering the Mugrosa-C Formation (in Tenerife-1 and -2) and in the rest of the log it was calculated from P-wave logs using Castagna's Relation. This is an empirical linear relation between P- and S-wave velocities for brine-saturated and dry clastic rocks ($Vs = 0.8621\,Vp - 1.1724$; velocities given in km/s). This expression varies depending on the amount of clay and fluid content, but for this purpose it is a good approximation. For a more precise fluid saturation analysis, saturation curves would be needed; so it will be left for a future study.

In Figure 4.4 the different cross-plots mentioned above are displayed. Figure 4.4-a shows Vp/Vs versus Vp, colored by GR. Low values of GR (up to 60) can be related to sands whereas values above 60 can be related to shales. These two groups are circled in the figure, being the sands associated to higher Vp values. Thus, according to the logs, the sands are high impedance.

Figure 4.4-b shows the cross-plot of Vp/Vs against Vp, colored by resistivity. This plot can be indicative of fluid saturation. Higher resistivity values (circled in red) are related to lower Vp/Vs (less than 1.7 according to the plot) and high impedance. These can be potentially hydrocarbon sands. The group circled in green can be associated with brine sands, with Vp/Vs values of 1.7 – 1.9.

In this cross-plot (Figure 4.4-b), a pseudo-linear Vp/Vs - Vp trend can be observed for the high resistivity sands (marked with a red circle). One possible explanation for this observation can be found in Figure 4.5. This figure represents a theoretical cross-plot between Vp/Vs versus P impedance based on rock physics templates. It also displays the effect of changes in shaliness, porosity and fluid saturation. If the shaliness increases, the original curve (red curve) will be shifted towards higher Vp/Vs values (grey). An increase in the porosity will be associated with lower P impedance and slightly higher Vp/Vs values; and, for a constant porosity, an increase in the hydrocarbon saturation will reduce both the Vp/Vs and P impedance values. There are no measured Density logs in the Tenerife wells, therefore, it is assumed that the relation between Vp and density satisfies Gardner's equation; thus when plotting Vp/Vs against Vp, the same behavior as the theoretic plot is expected. A possible explanation for the observed linear trend between Vp and Vp/Vs for the high resistivity sands (marked in a red circle) could be that the sands present in the field have different porosities, hydrocarbon saturation and shaliness.

As Vs logs were computed from Vp, using Castagna's equation, the cross-plots shown in Figures 4.4-a and -b are exactly the same for Vs, leading to the same conclusions.

In Figure 4.4-c GR against Vp/Vs, colored by resistivity, is plotted for the whole logs' length every meter. A pseudo-linear trend between GR and Vp/Vs is observed, indicating that Vp/Vs could be a good lithology and fluid discriminator. This same plot was analyzed considering the different intervals between the interpreted horizons. Figures 4.4-d, -e, -f and -g display GR against Vp/Vs (colored by resistivity) for the intervals delimited by: the top of the logs – Mugrosa-C, Mugrosa-C – Esmeraldas, Esmeraldas-Eocene Unconformity, and Eocene Unconformity – bottom of the logs. A similar linear GR - Vp/Vs trend is observed for all the intervals except for the Esmeraldas – Eocene Unconformity. In the latest one, the GR values are very similar for different Vp/Vs values. According to the lithostratigraphic description of the Paleogene units, this interval is composed mainly by siltstones and mudstones, unlike the other Paleogene intervals which are mainly composed of interbedded sandstones and mudstones. According to this, in the Esmeraldas - Eocene Unconformity interval, Vp/Vs is not expected to be a good lithology discriminator.

Figure 4.4-h shows the same cross-plot as Figure 4.4-c highlighting the areas associated with shales, with most likely hydrocarbon sands and with mostly brine-saturated sands.

So, based on the cross-plots just described, it can be concluded that Vp/Vs could be a good lithology and fluid discriminator in all the Paleogene units except the interval delimited by Esmeraldas and the Eocene Unconformity. For this reason, the analysis in the 3D-3C volume is focused in this attribute.

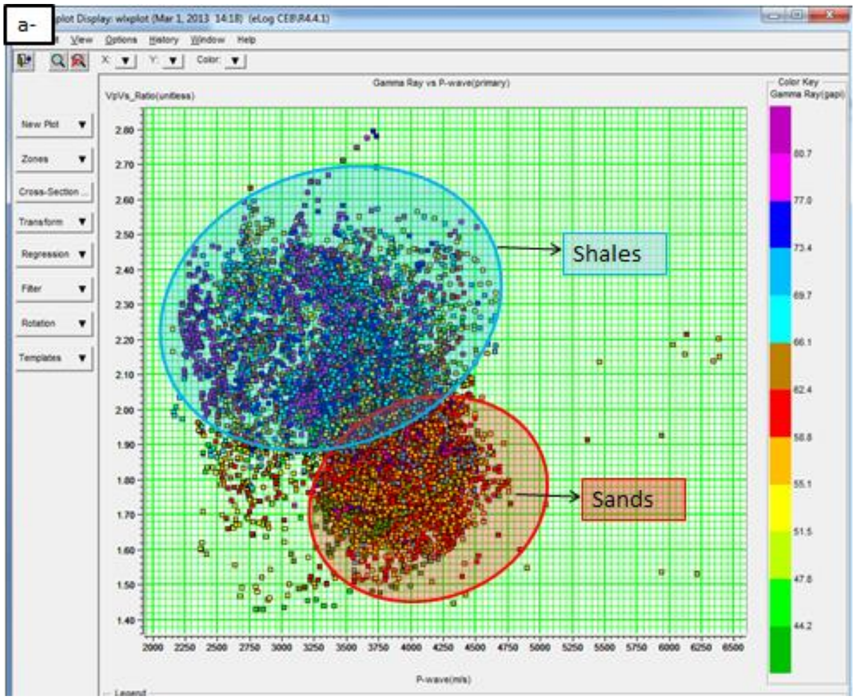

Figure 4.4-a: Cross-plot of Vp/Vs against Vp, colored by GR, circling areas mostly related to sands and shales

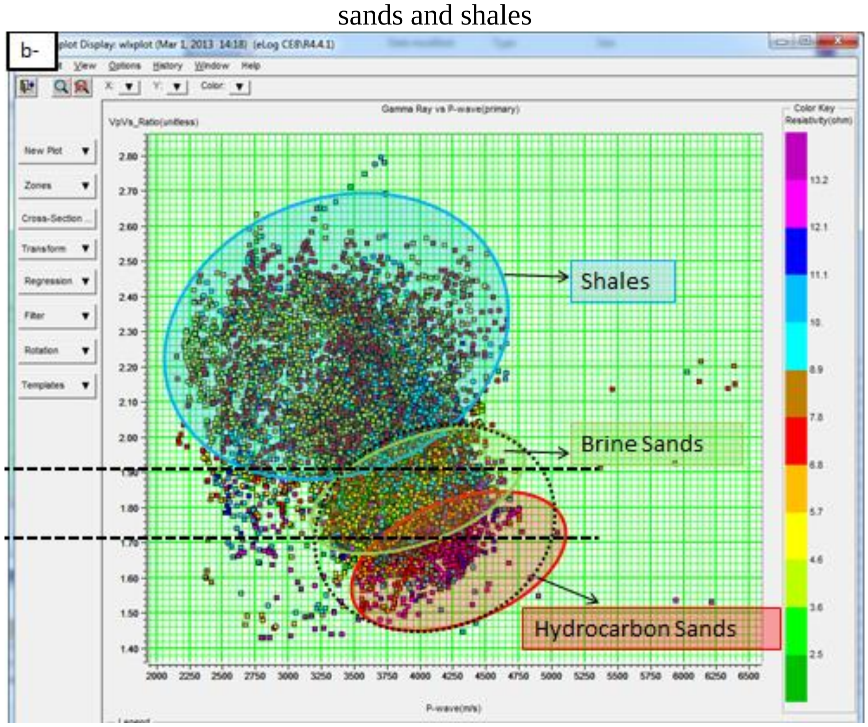

Figure 4.4-b: Cross-plot of Vp/Vs versus Vp, colored by resistivity, circling areas mostly related to shales, most likely hydrocarbon-saturated sands and brine sands.

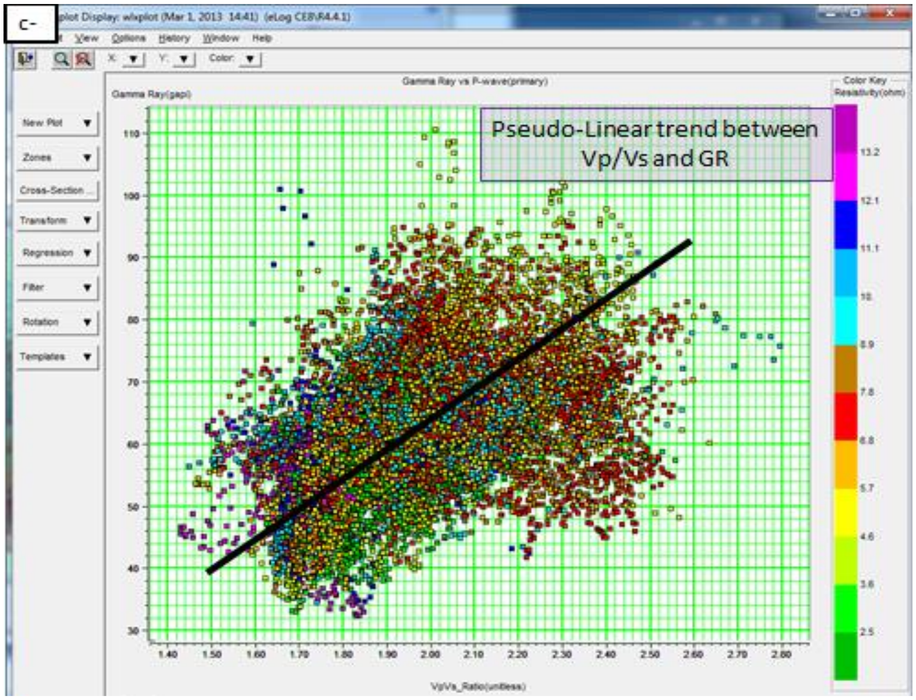

Figure 4.4-c: Cross-plot of Vp/Vs versus GR, colored by resistivity, indicating a pseudo-linear trend between Vp/Vs and GR (full log).

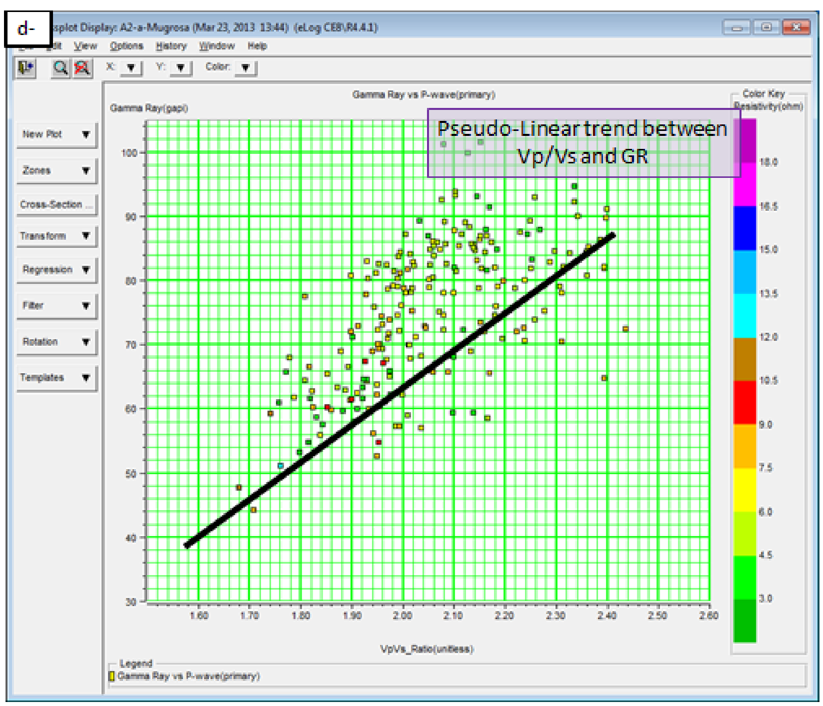

Figure 4.4-d: Cross-plot of Vp/Vs versus GR, colored by resistivity, indicating a pseudo-linear trend between Vp/Vs and GR (top – Mugrosa-C).

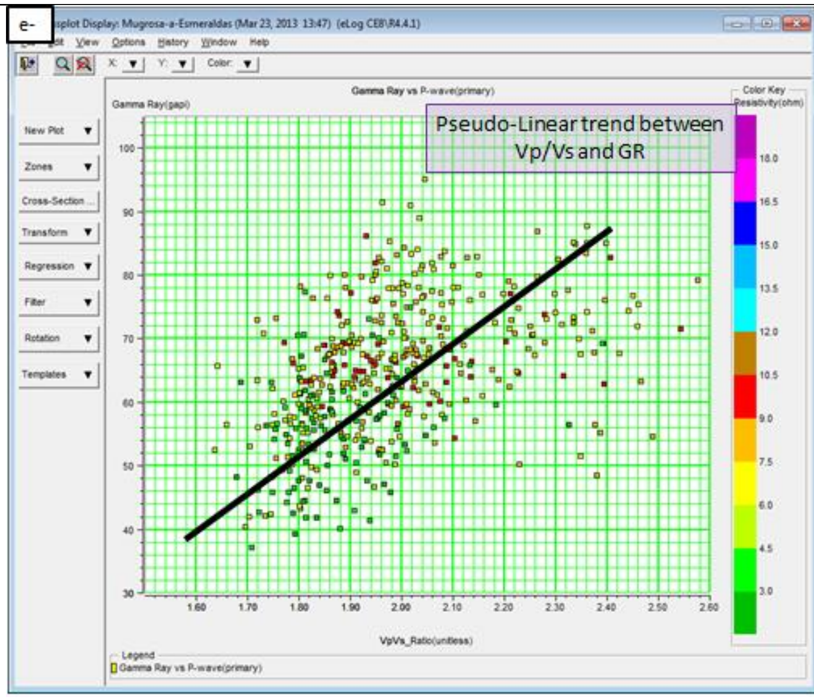

Figure 4.4-e: Cross-plot of Vp/Vs versus GR, colored by resistivity, indicating a pseudo-linear trend between Vp/Vs and GR (Mugrosa-C - Esmeraldas).

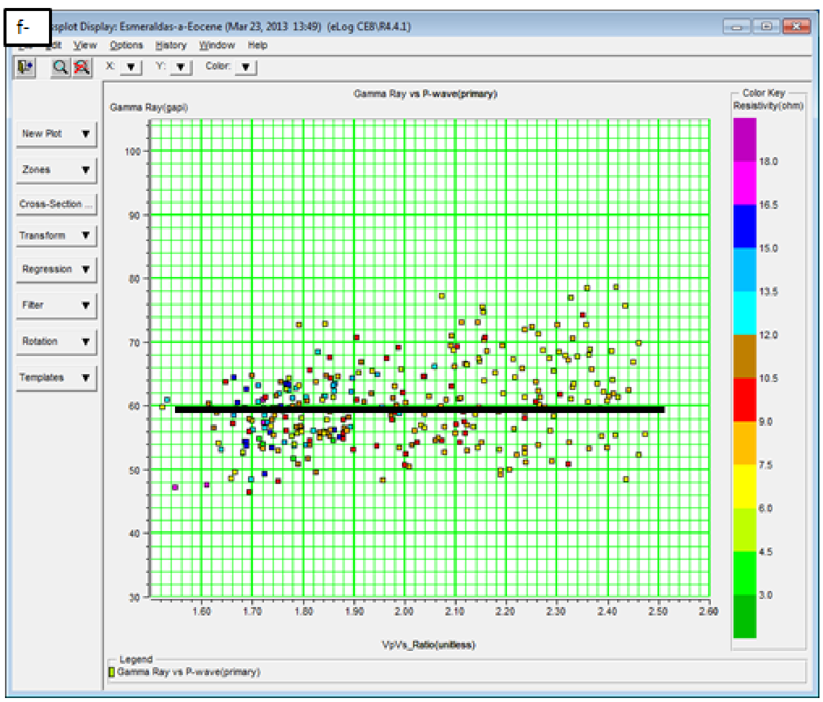

Figure 4.4-f: Cross-plot of Vp/Vs versus GR, colored by resistivity, indicating a pseudo-linear trend between Vp/Vs and GR (Esmeraldas – Eocene Unconformity).

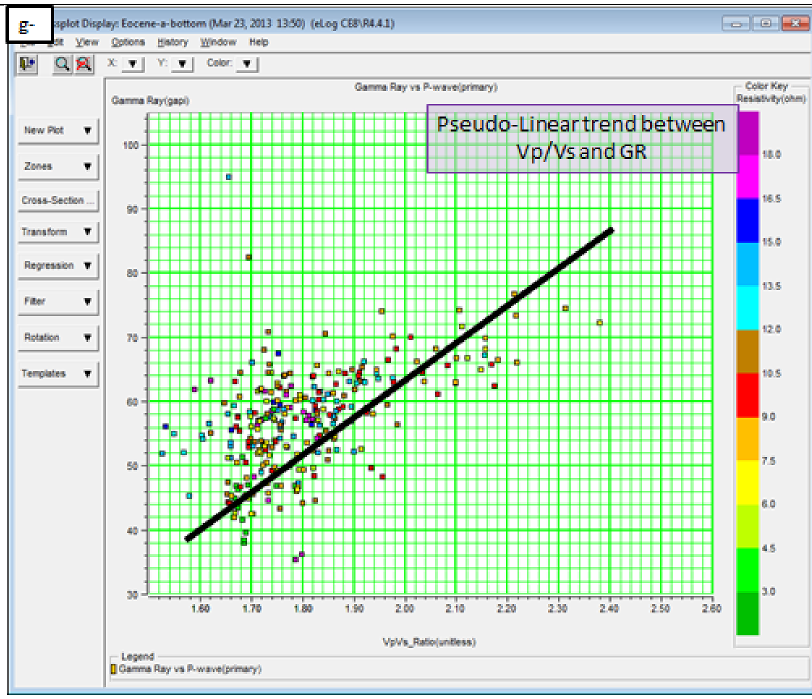

Figure 4.4-g: Cross-plot of Vp/Vs versus GR, colored by resistivity, indicating a pseudo-linear trend between Vp/Vs and GR (Eocene Unconformity - bottom of the logs).

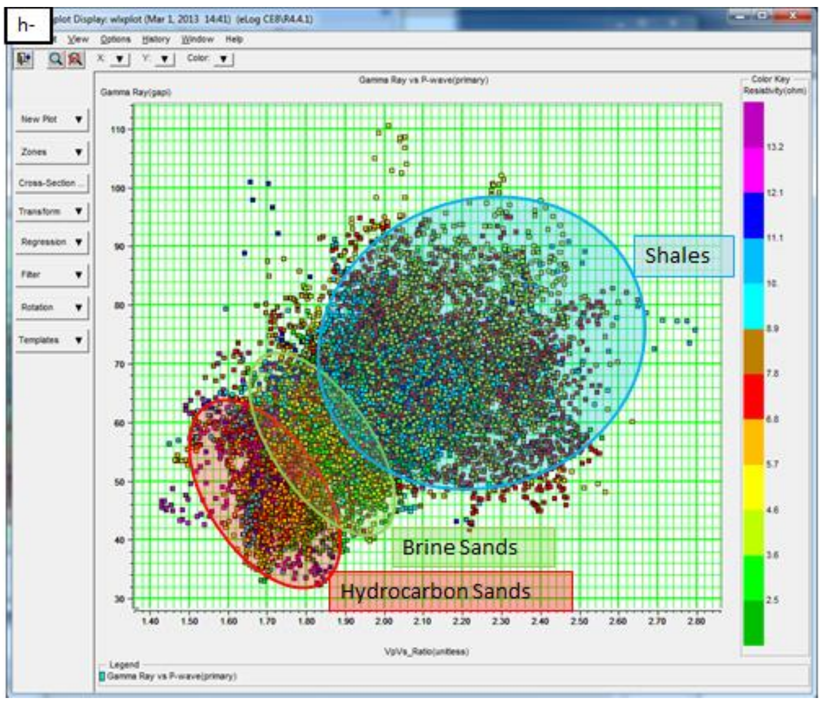

Figure 4.4-h: Cross-plot of Vp/Vs versus GR, colored by resistivity, circling areas mostly related to shales, most likely hydrocarbon-saturated sands and brine sands.

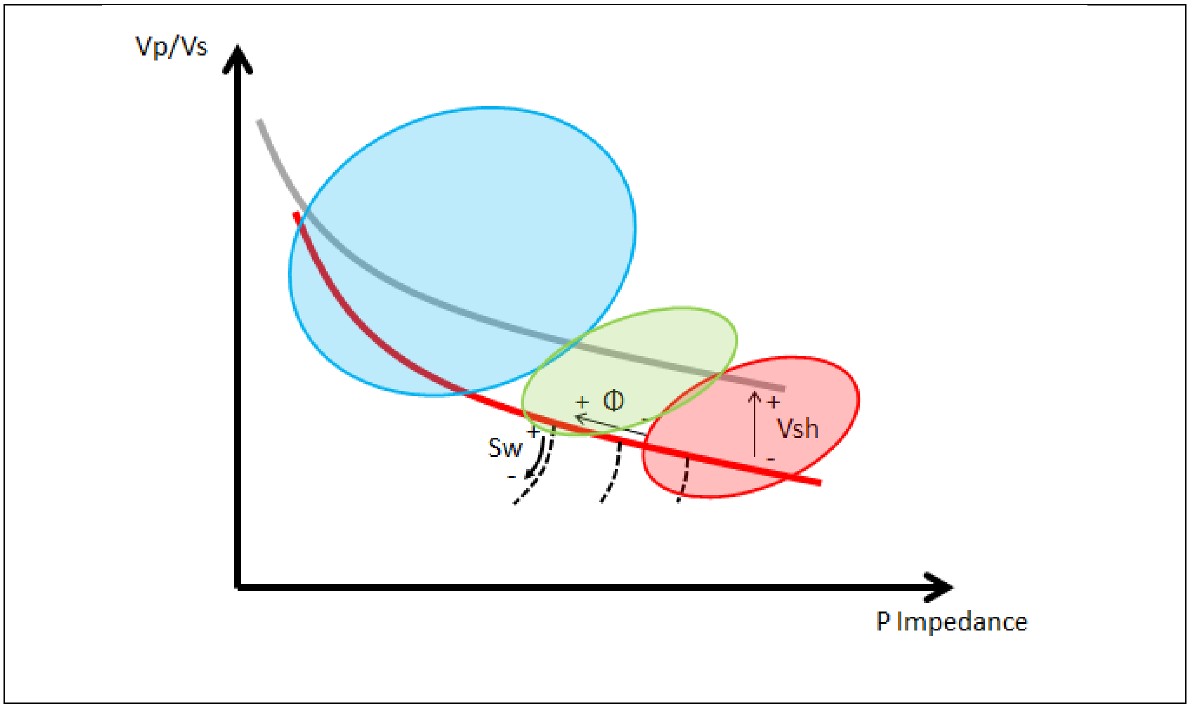

Figure 4.5: Theoretical cross-plot of Vp/Vs versus P impedance for different shaliness, porosity, and hydrocarbon saturation.

4.3 2D-3C - Interpretation

Based on the VSP and the well logs, the horizons of interest (Middle-Eocene Unconformity, Esmeraldas and Mugrosa-C and –B) were identified and interpreted in the PP- and PS- 2D-3C lines. This allowed a correlation of the events and a conversion of the PS-seismic section to PP time (Figure 4.6). A good correlation is observed; also similar amplitudes are found in almost all the seismic section except for a portion (highlighted in a grey square) where the events are more attenuated in the PP stack than in the PS.

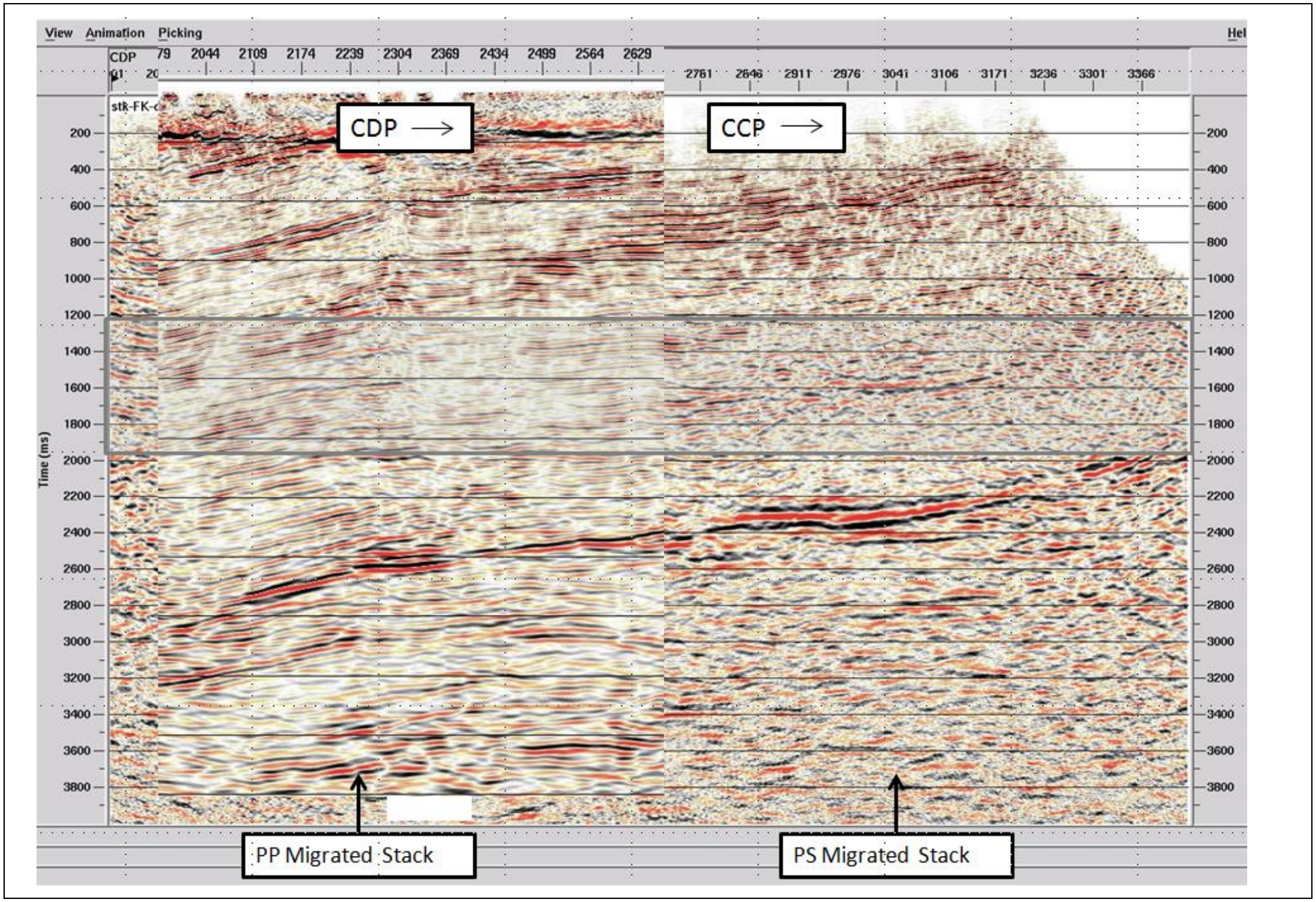

Figure 4.6 Correlation of PP- and PS-migrated stacks for line EXP-TEN-2D3C-1. PS time scale was modified to be consistent to PP-waves time (in ms).

4.4 3D-3C - Interpretation

The 3D Survey was acquired between September 2009 – January 2010 using three component MEMS sensors and a dynamite source. The whole area covers 22.6 km^2, with 19 receiver lines (with 280 m spacing between them) and 17 source lines (with 360 m spacing) conforming an orthogonal geometry.

The complex near surface of the MMV including a robust weathering, the presence of conglomerates and the recent deposition of fluvial deposits with lateral variations in thickness, led to a strong groundroll present in the shot records (Agudelo et. al., 2013). A receiver spacing of 20 m was chosen for optimal groundroll attenuation. Shot stations separation was of 20 m too, leading to a maximum effective offset of 3400 m.

The trace length was of 5000 ms for the PP section and of 8000 ms for the PS section.

The 3C-3D survey was processed up to Pre-stack Time Migration (PSTM) by ION Geophysical and CGG Veritas. The inline and crossline ranges were 6001-6504 and 2001-2575 respectively. The bin size used for processing was 10 m x 10 m, providing a nominal fold of 80.

Figures 4.7 and 4.8 show the PSTM stacks for crossline 2300 (location shown in the base-map in the bottom left) for the PP and PS volumes processed by CGG Veritas. Also the amplitude spectra for different time windows were added to show the frequency content of the stack.

The PSTM stacks processed by CGG Veritas were used for the interpretation as the seismic events were more continuous and better defined when compared to the ones provided by ION Geophysical.

As it was expected, the frequency content for the whole volume was higher in the PP-PSTM stack than in the PS stack. In the target, which is between 1100 – 1700 ms for PP-waves and 1800 - 2800 ms for PS-waves, the period (T) is 34 ms and 60 ms respectively (Figure 4.9).

According to Sheriff (1991), resolution is the ability to separate two features that are very close together. This was expressed mathematically by Lord Rayleigh who defined the limit of resolution as 1/4 of the dominant wavelength; in other words the minimum thickness of a bed in which reflections from its top and base can be distinguished can be determined by $V/4f$, being V the interval velocity and f the frequency. To compute the vertical resolution, average interval velocities were used; corresponding, in this dataset, to 3500 m/s and 2300 m/s for the PP and PS volumes respectively (obtained from the sonic logs). The dominant frequency (f_{dom}) is related to the period T by: $f_{dom} = {}^{1}/_{T}$. When replacing these values in the expression for the vertical resolution, values of 30 m and 35 m were obtained for PP and PS respectively.

Thus, with conventional seismic, the 5m-thickness sands within the Mugrosa Formation won't be resolved; but the sand bodies of 30 m thick could.

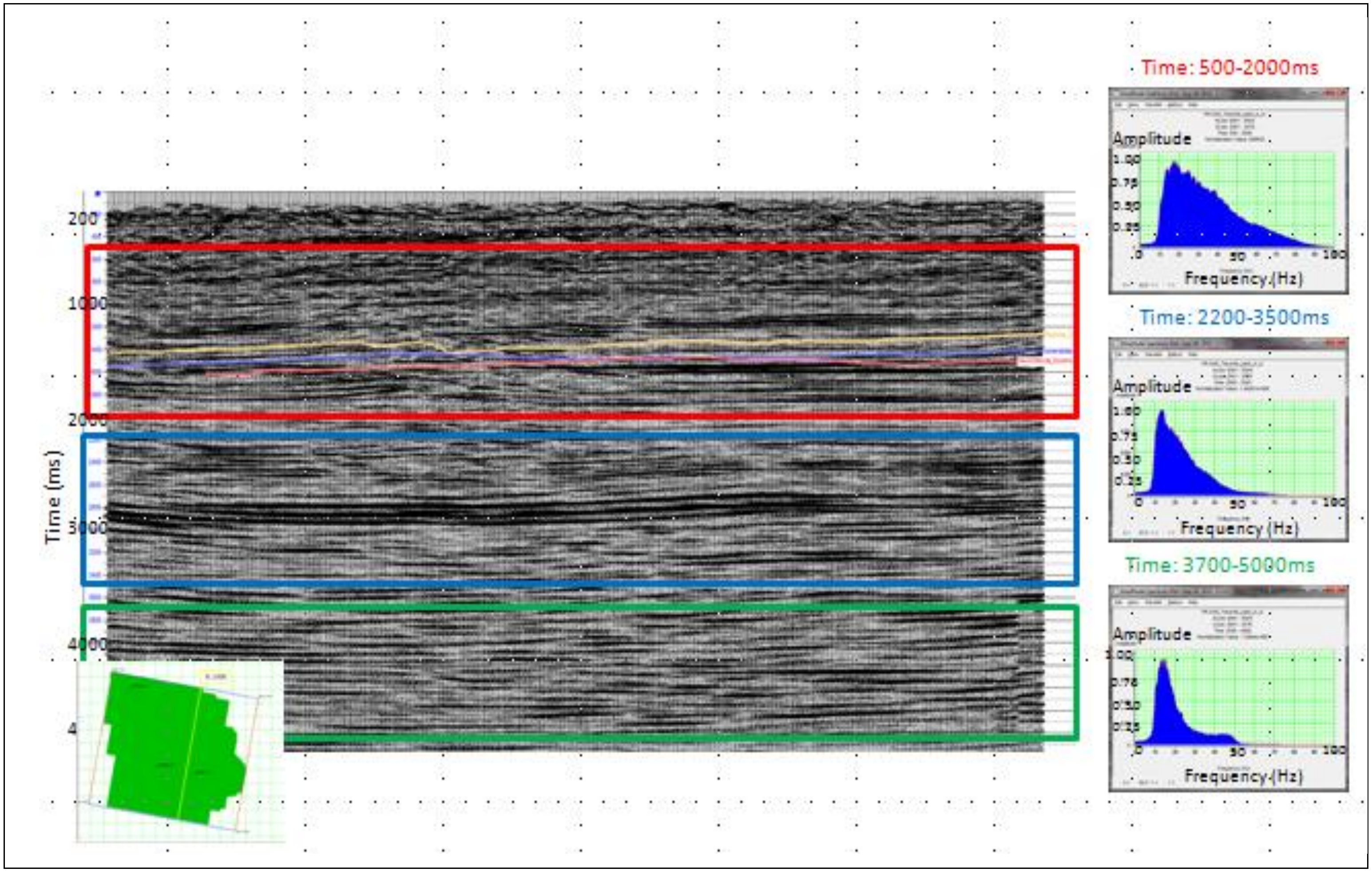

Figure 4.7: PP-PSTM stack for XL2300 (location in the base-map displayed in the bottom left of the stack) and amplitude spectra for 500-2000 ms, 2200-3500 ms and 3700-4800 ms.

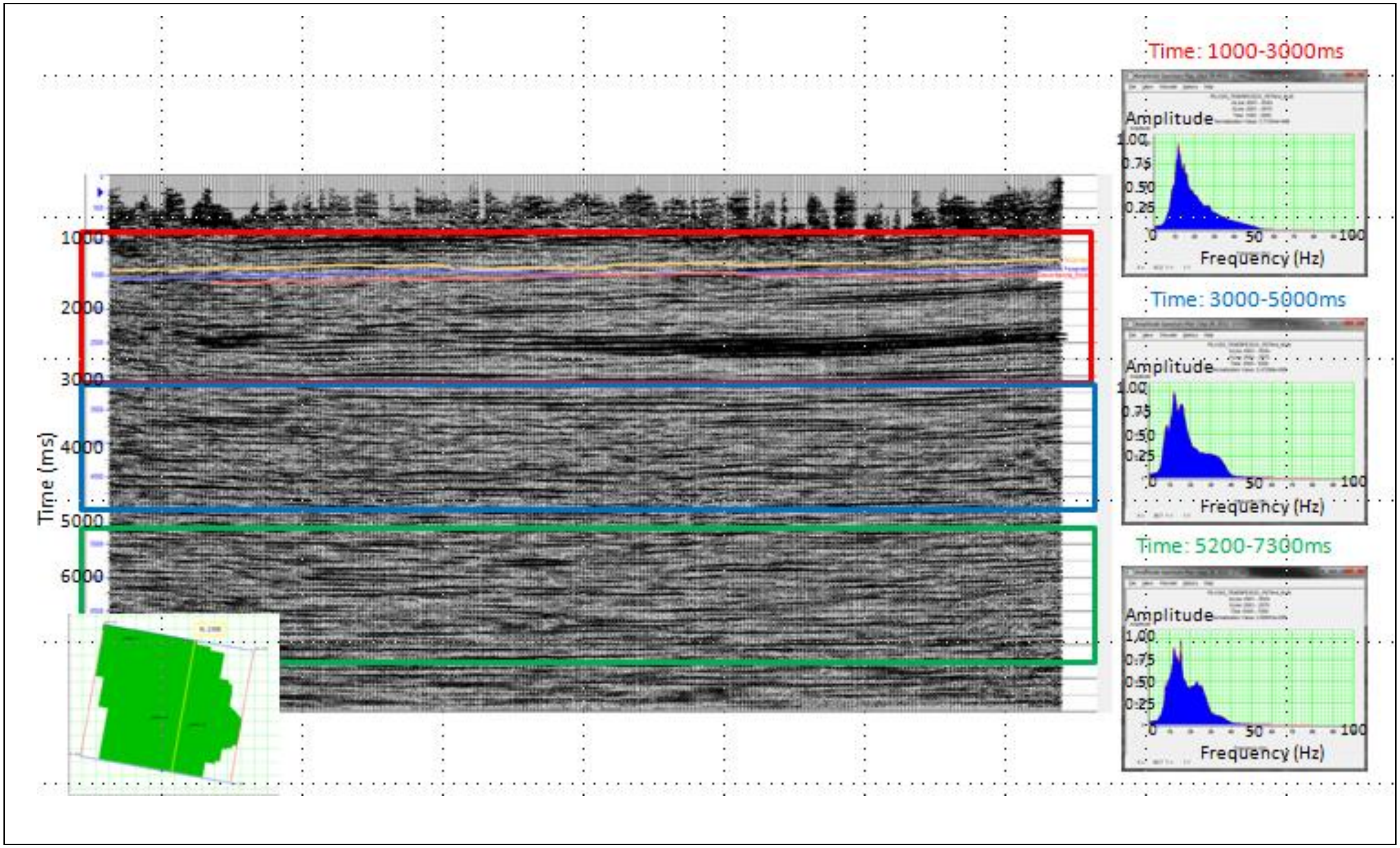

Figure 4.8: PS-PSTM stack for XL2300 (location in the base-map displayed in the bottom left of the stack) and amplitude spectra for 500-2000 ms, 2200-3500 ms and 3700-4800 ms.

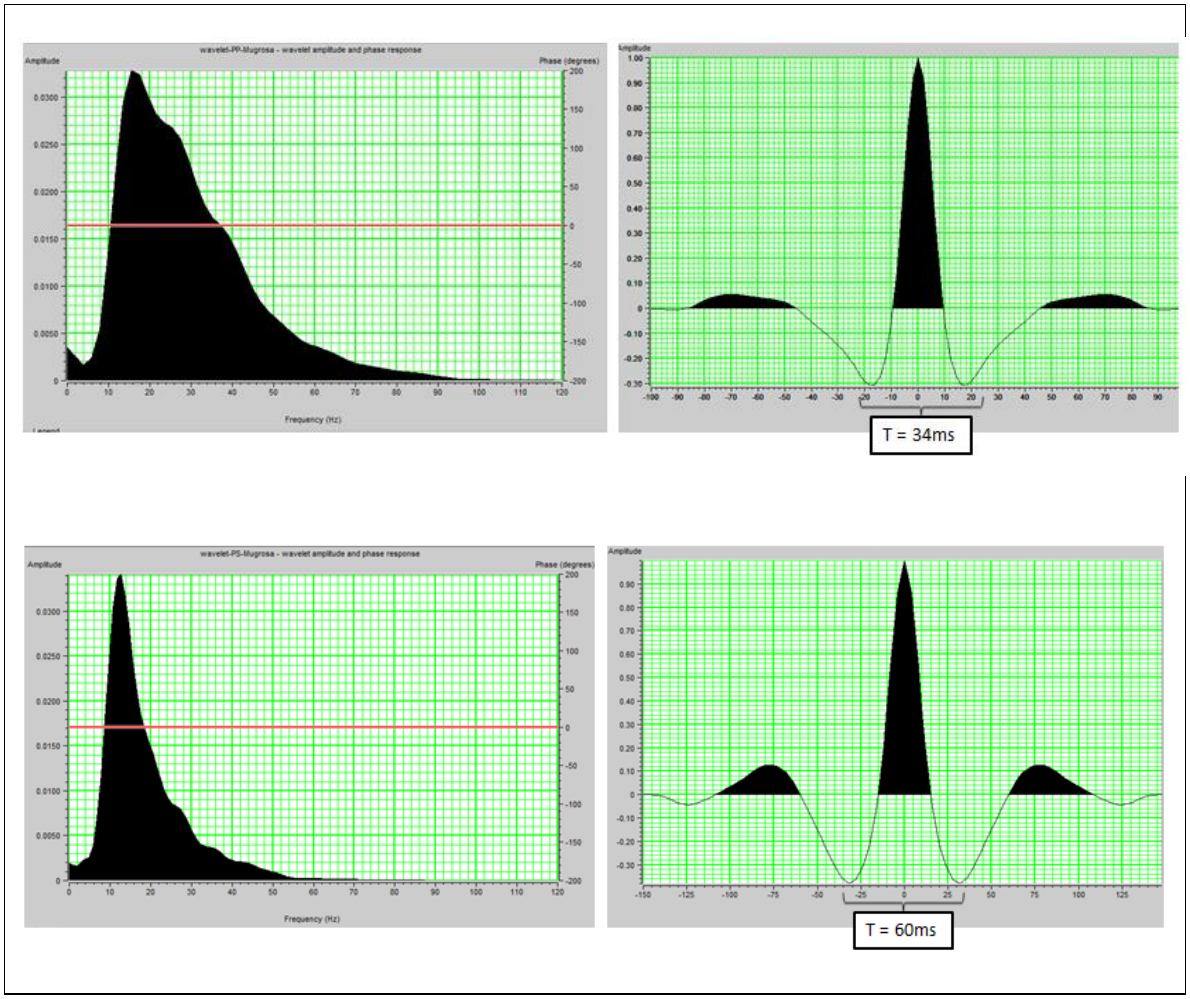

Figure 4.9: wavelet amplitude and time response for: (top) a window of 1100 – 1700 ms for the PP migrated stack, and (bottom) a window of 1800 – 2800 ms for the PS migrated stack. The period (T) for both wavelets is marked in both plots.

4.5 Vp/Vs Maps

Two types of Vp/Vs maps were obtained from the PP- and PS-migrated volumes: a regional and a high-resolution one. The regional Vp/Vs map is based on Garotta's equation, which states that:

(5)

$$\frac{V_P}{V_S} = \frac{2\Delta T_{PS}}{\Delta T_{PP}} - 1,$$

where ΔT_{PS} and ΔT_{PP} are the two-way travel-time difference between two events in PS and PP time, respectively. This approximation is not appropriate for thin layers as it becomes unstable when the denominator approaches to zero; i.e., for narrow time intervals. To obtain the long wavelength Vp/Vs maps, three of the interpreted horizons (the tops of the Eocene Unconformity, Mugrosa-C and Mugrosa-B) in the PP- and PS-migrated volumes were used. These horizons were interpreted every 10 in-lines and 10 cross-lines in the both volumes, and then were interpolated and smoothed along the whole survey area. The Time-Depth curves for the three wells have been provided. The interpreted horizons in the seismic section were tied with the wells and VSP, allowing a precise horizon correlation between the interpreted horizons in the PP- and PS-seismic sections. The Vp/Vs map obtained this way provides regional Vp/Vs values as they are constant in time for the events between two consecutive interpreted horizons. Figure 4.10 shows a regional Vp/Vs map for an arbitrary line that goes along the three wells.

The high-resolution Vp/Vs maps were obtained following the method proposed by Guliyev et al. (2006) in which the acoustic impedances are used. The regional Vp/Vs maps allow the conversion of the PS-seismic section in PS-time to PP-time. With both seismic sections in PP time, model based inversions were run providing and a new set of Vp/Vs maps from the quotient of AI and SI (AI: PP-acoustic impedance; SI: PS-impedance).

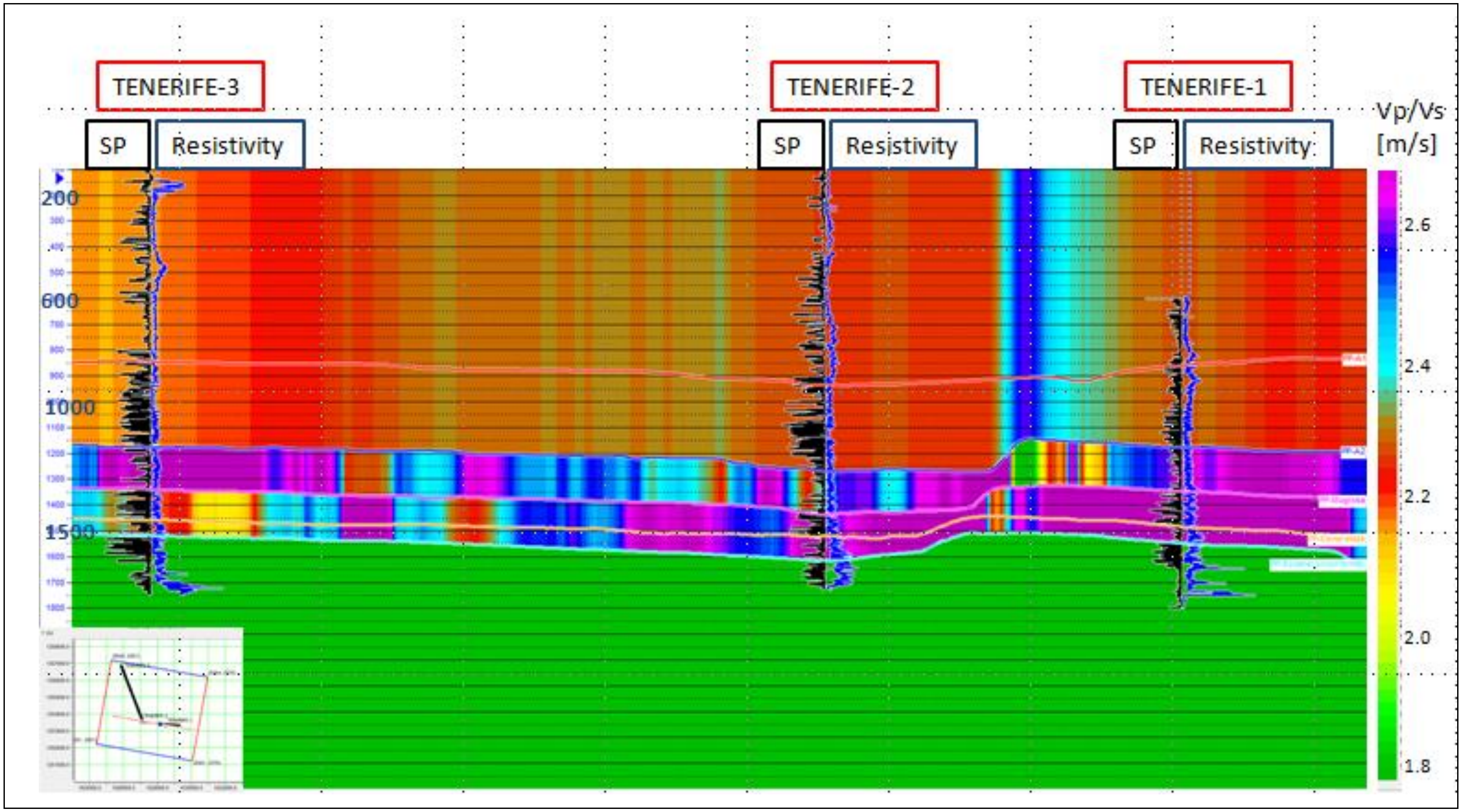

Figure 4.10: Regional Vp/Vs map along an arbitrary line (shown in the base map - bottom left) obtained from the interpreted horizons in the PP- and PS- migrated volumes.

4.6 PP-PS - Inversions

To run the model based inversions on the two seismic volumes in PP-time, first the wavelets were extracted from the PP- and PS-migrated stacks at a time window between the horizons A1 and the Eocene Unconformity. Figure 4.11 shows the wavelets extracted from the original PP- and PS- in PP-time sections. When comparing the wavelets extracted from both volumes a slight difference in the bandwidth is observed, corresponding the wider bandwidth to the PP-waves.

Although the inversion was performed separately for PP- and PS-seismic volumes, it was necessary to have similar wavelets. So, different methods were tested to create comparable ones. These included a shaping filter applied to the PP-volume using the PS- in PP-time volume as a reference, a band-pass filter applied to the PP-volume (5-8-18-50) and to the PS-volume (5-8-26-50), and a convolution of the PP-volume with the wavelet extracted from the PS- one. When comparing the extracted wavelets from all these filtered volumes, the band-pass volumes were chosen (Figure 4.12). Figure 4.13 displays the seismic sections for PP- and PS-filtered volumes used for the inversion.

No density logs were available for any of the wells, so the density needed for the inversions was calculated with the Gardner equation ($\rho = 0.23\ V^{0.25}$, for a given velocity in km/s and density in g/cc). The low-frequency models for the inversion were obtained from filtered Vp/Vs and acoustic and shear impedance logs from Tenerife-2. A low-pass filter of cutoff frequencies of 5-8 Hz was used. Figure 4.14 show the initial models for PP- and PS- for the model-based inversions. To adjust the parameters chosen for both inversions, such as number of iterations and scalars applied to the wavelet among others, the three wells were considered.

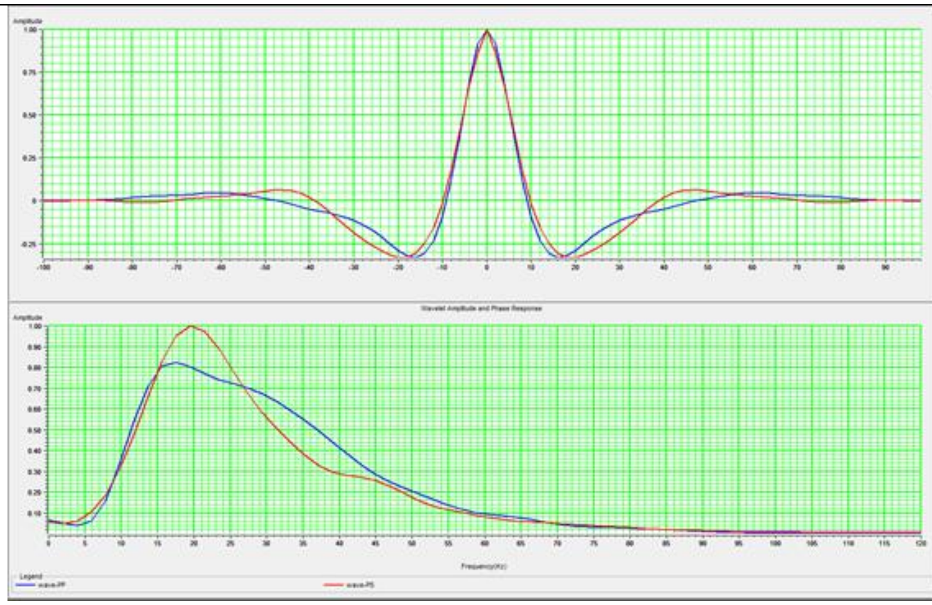

Figure 4.11: Extracted wavelets and amplitude spectra from the original PP- (blue) and PS- (red) volumes.

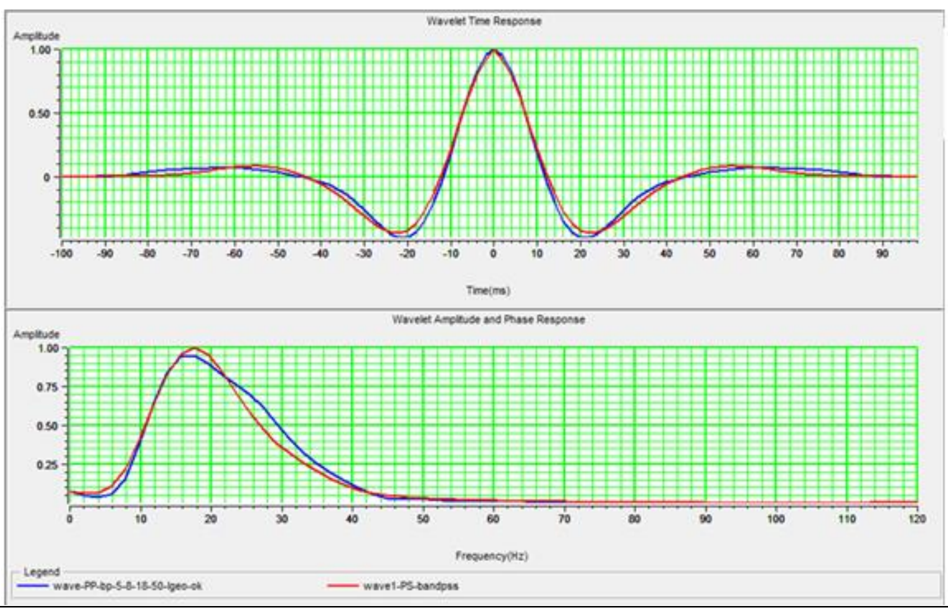

Figure 4.12: Extracted wavelets and amplitude spectra from the filtered PP- (blue) and PS- (red) volumes.

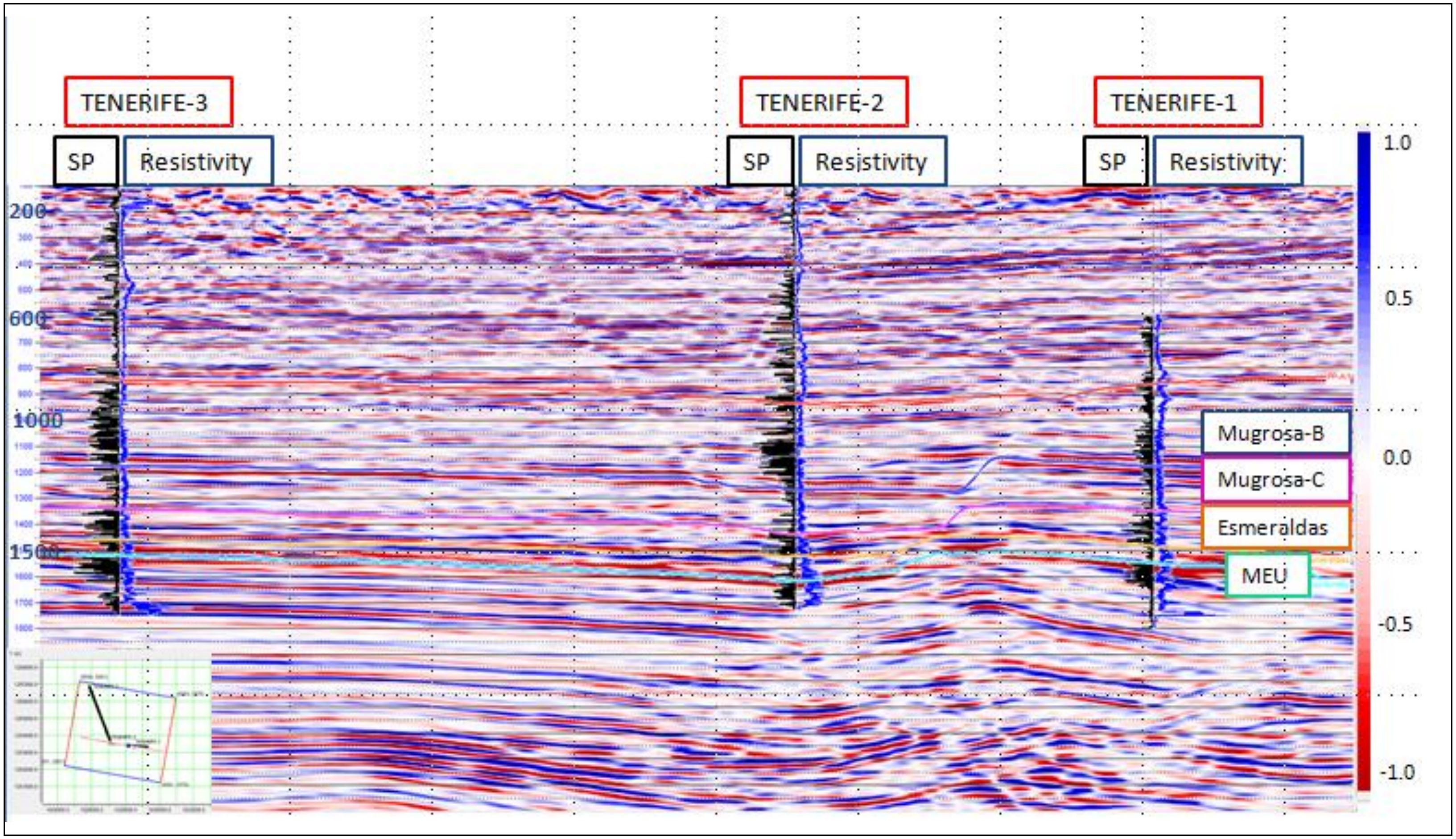

Figure 4.13 (a): Seismic section of the PP-migrated volume with a bandpass of 5-8-18-50 along the arbitrary line shown in the base map-bottom left.

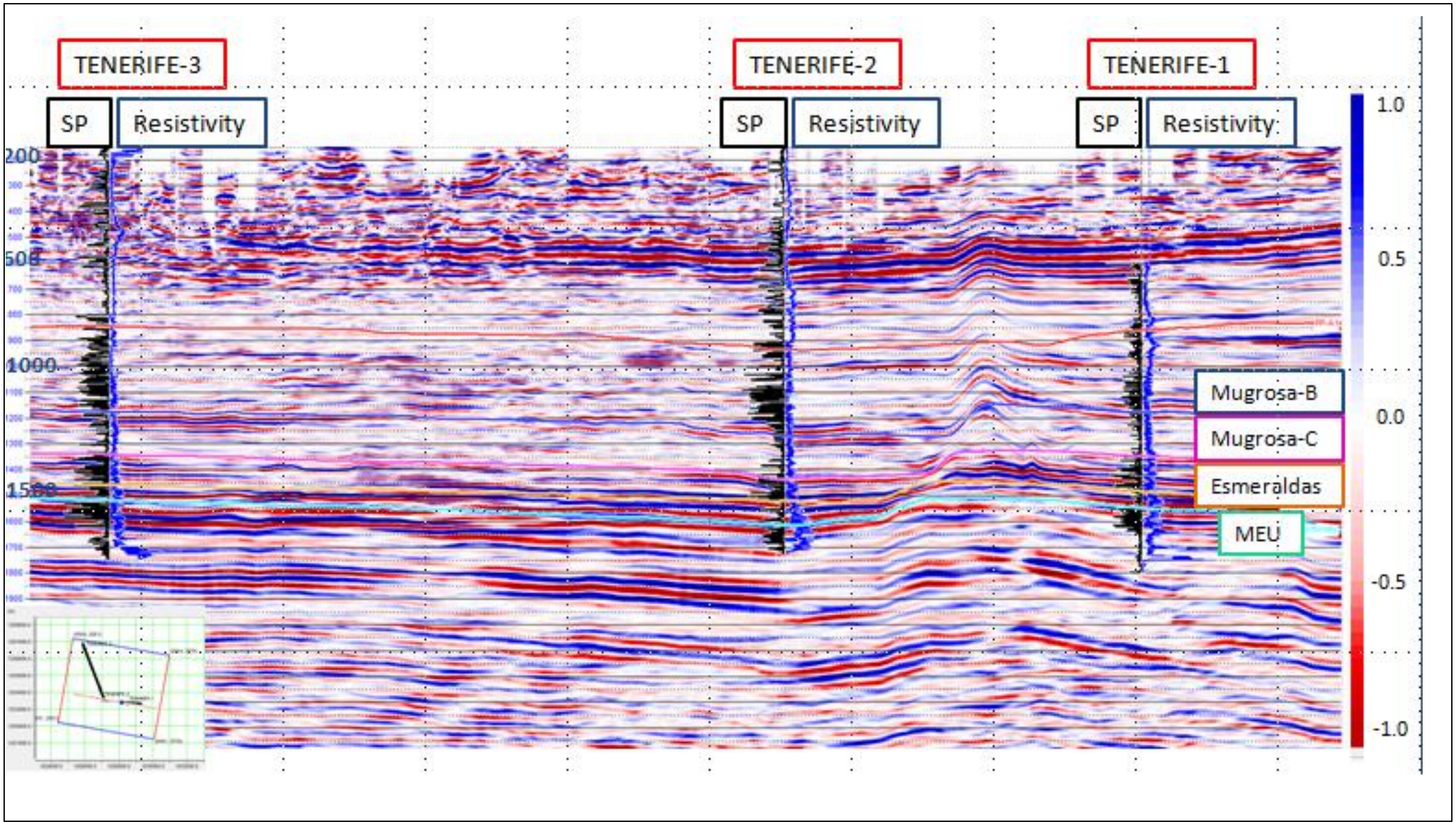

Figure 4.13 (b): Seismic section of the PP-migrated volume with a bandpass of 5-8-26-50 along the arbitrary line shown in the base map-bottom left.

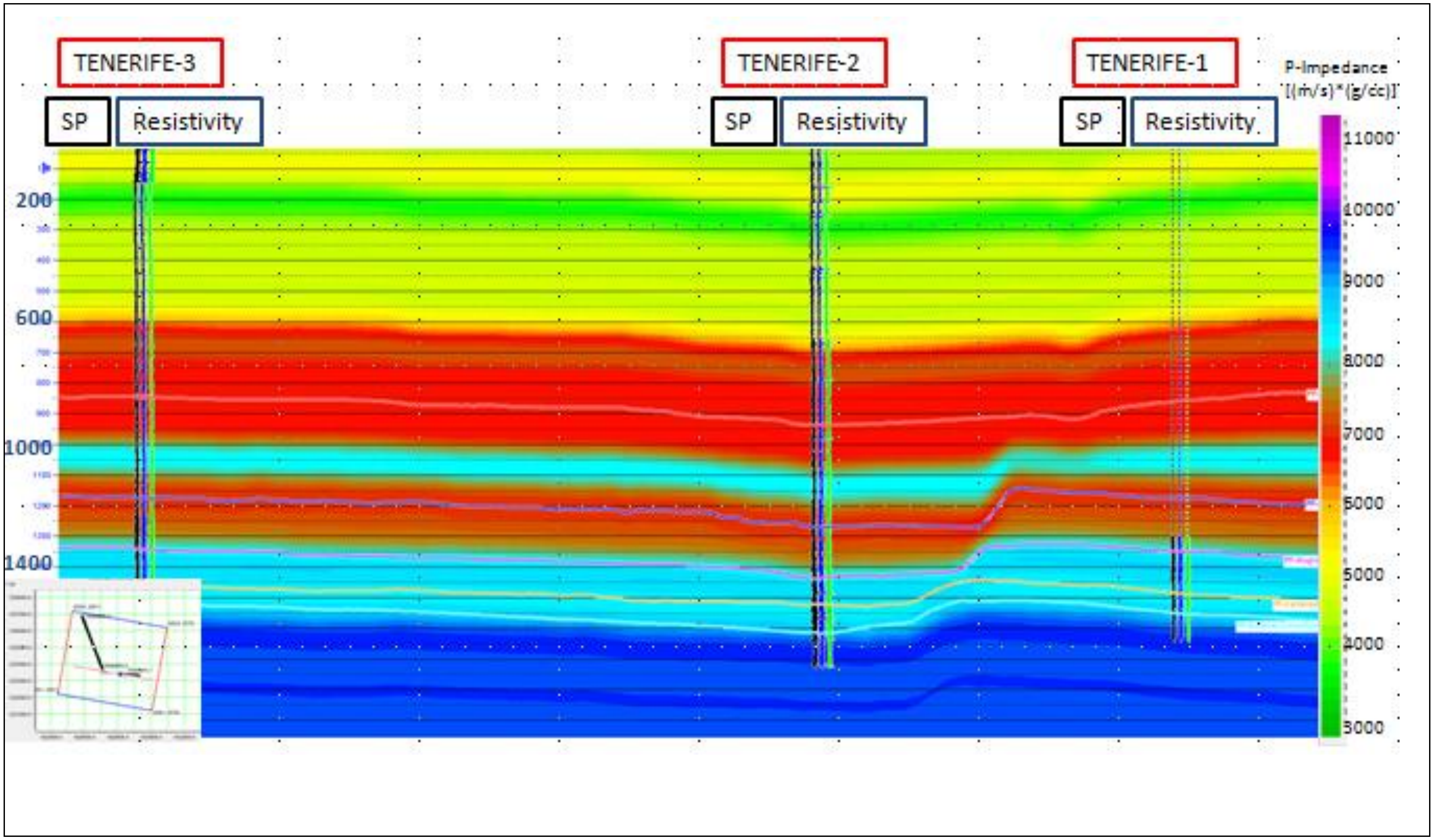

Figure 4.14 (a): Model for the PP-model-based inversion along an arbitrary line (shown in the base map-bottom left).

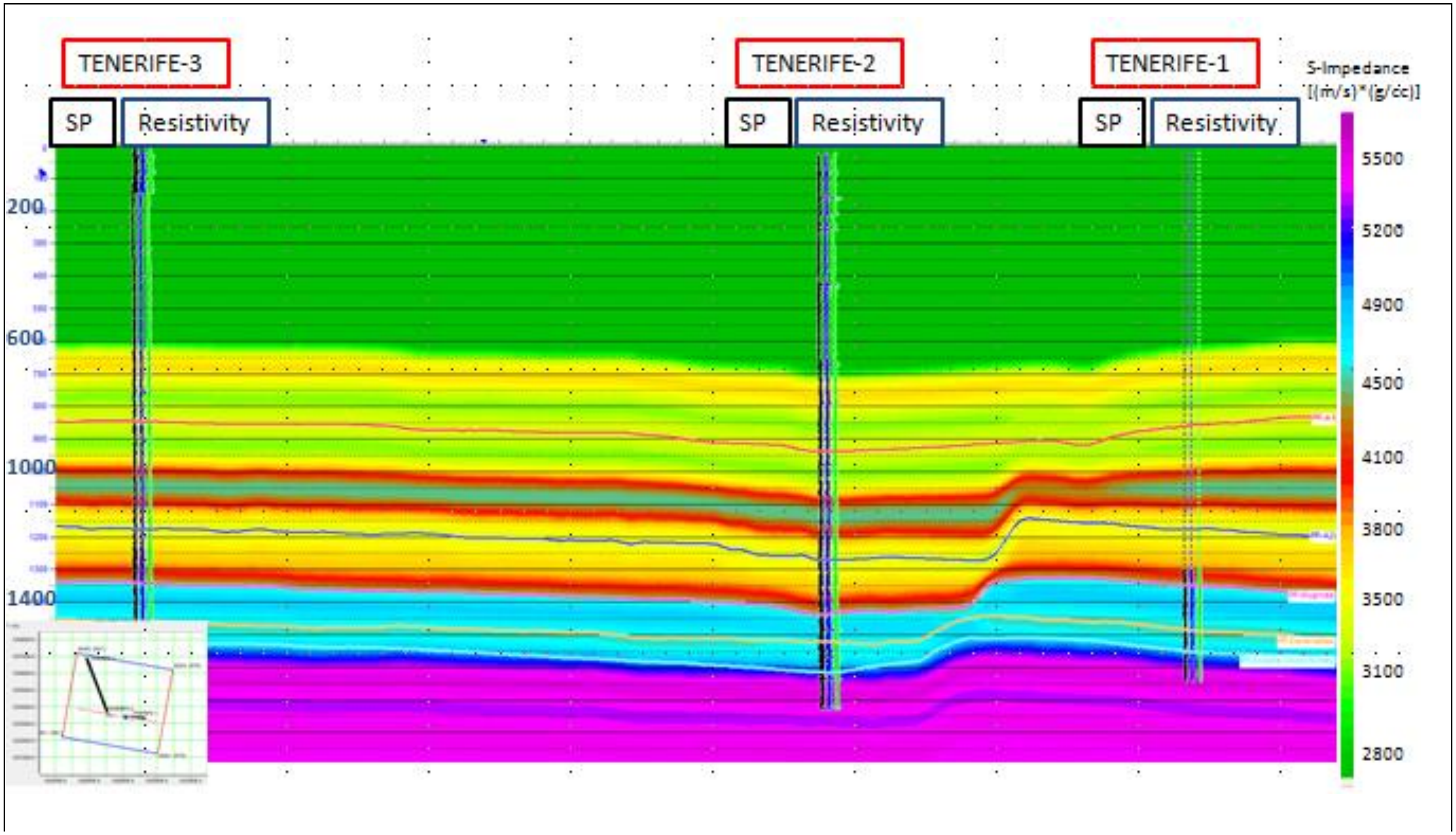

Figure 4.14 (b): Model for the PS-model-based inversion along an arbitrary line (shown in the base map-bottom left).

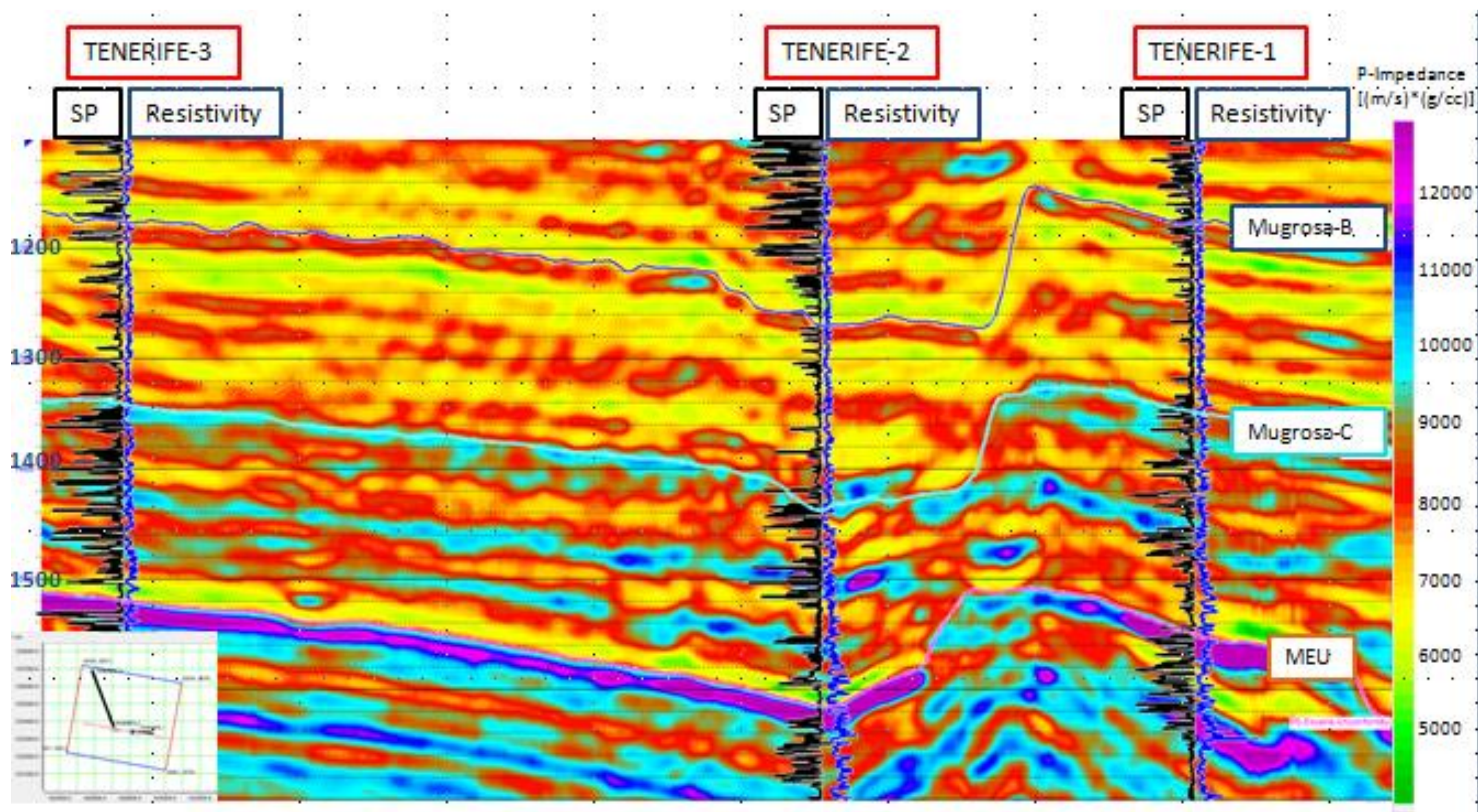

Figure 4.15 (a): PP-impedance centered in the Mugrosa Formation along an arbitrary line (shown in the base map-bottom left).

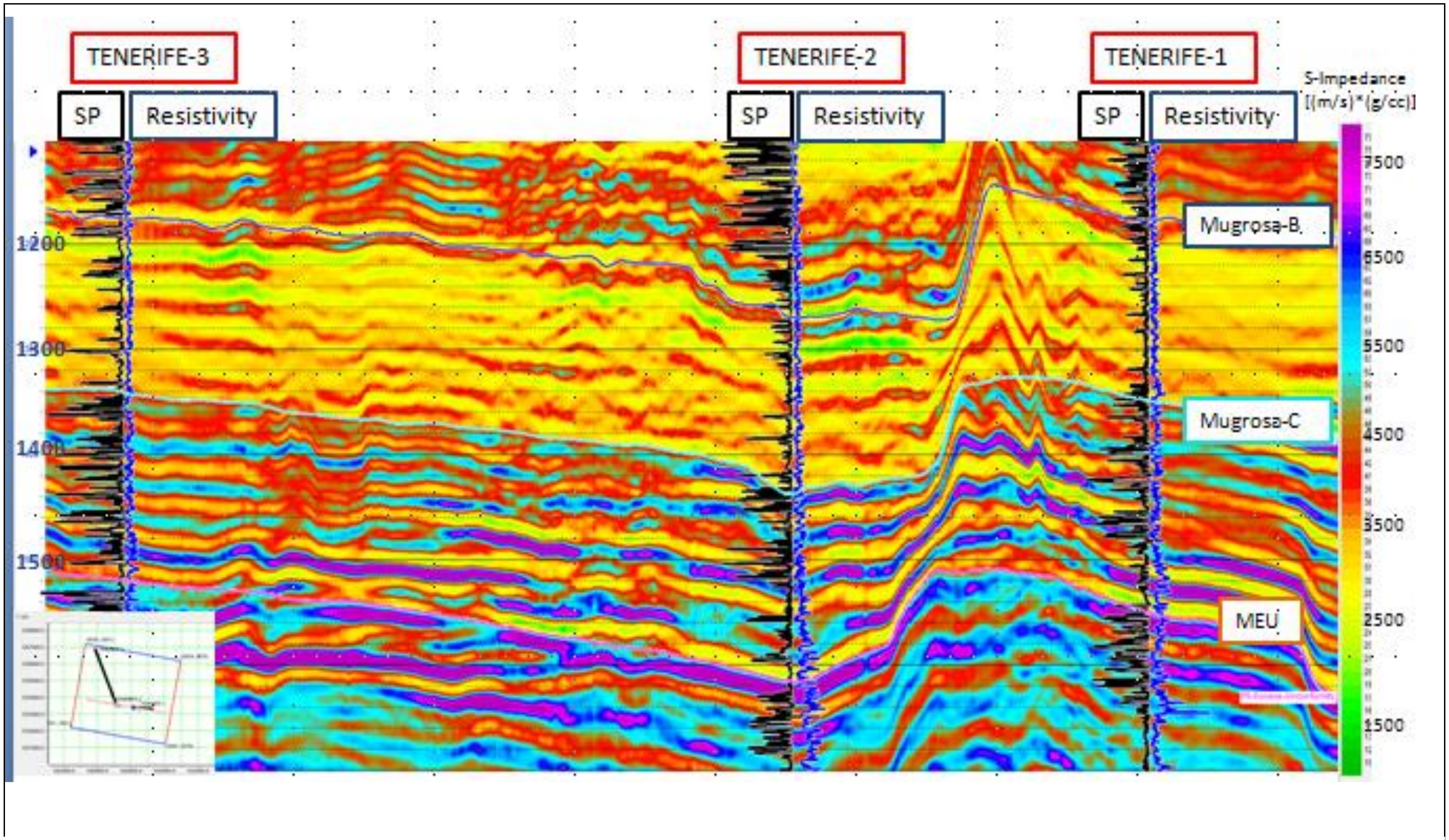

Figure 4.15 (b): PS-impedance centered in the Mugrosa Formation along an arbitrary line (shown in the base map-bottom left).

In Figure 4.15 the PP- and PS- impedances can be observed in a vertical section (in time) zooming in the target area; the top of the Mugrosa-C Formation is marked with a cyan horizon. Intercalated high and low impedance intervals can be observed, being the high impedance once related to sand bodies. Figure 4.16 shows the PP- and PS- impedance maps along a Mugrosa-C horizon map.

As it was mentioned before, Vp/Vs maps can be obtained from AI/SI; being AI and SI the PP- and PS- impedances respectively. So, the quotient of the two impedance volumes was calculated creating a high frequency Vp/Vs volume. In Figure 4.17 a horizon map coincident with the top of the Mugrosa-C Formation is displayed.

As it was known from previous reports from the Tenerife Field that wells Tenerife-1 and -2 were productive and -3 was dry, the Vp/Vs values expected for the first two wells were low. A low Vp/Vs value was observed in Tenerife-2 but not in Tenerife-1 nor in Tenerife-3. A possible explanation to this could be related to the character of the Mugrosa Formation at the wells.

Figure 4.18 shows the PP-impedance for the same arbitrary line along the wells mentioned above, as well as the SP and resistivity logs for the three wells; the top of Mugrosa-C is marked in cyan. In Figure 4.19 the logs corresponding to the three wells are displayed highlighting the Mugrosa-C Formation. Analyzing these two figures it can be confirmed that in Tenerife-1the gross thickness of the sands within the Mugrosa-C Formation is of 14 m and the net thickness is of 7 m. For a given interval velocity of 3500 m/s, a resolution of ~30 m can be achieved. So, a very probable cause of why the sand bodies within the Mugrosa Formation are not well determined in the Vp/Vs maps for Tenerife-1 can be that they are far below conventional seismic resolution.

For Tenerife-2 the gross and net thicknesses of the sands within the Mugrosa-C Formation are ~22m and ~14m respectively. Also the GR log's indication that they are clean sands confirms its association with the low Vp/Vs values observed in the horizon map in Figure 4.17.

For Tenerife-3 the gross thickness of the sands within the Mugrosa-C Formation is ~25m and the net thickness is ~20m; but according to the GR log, the shallow half of the interval is composed of shaly sands. This could be a cause of the not very low Vp/Vs value observed in the horizon map in Figure 4.17.

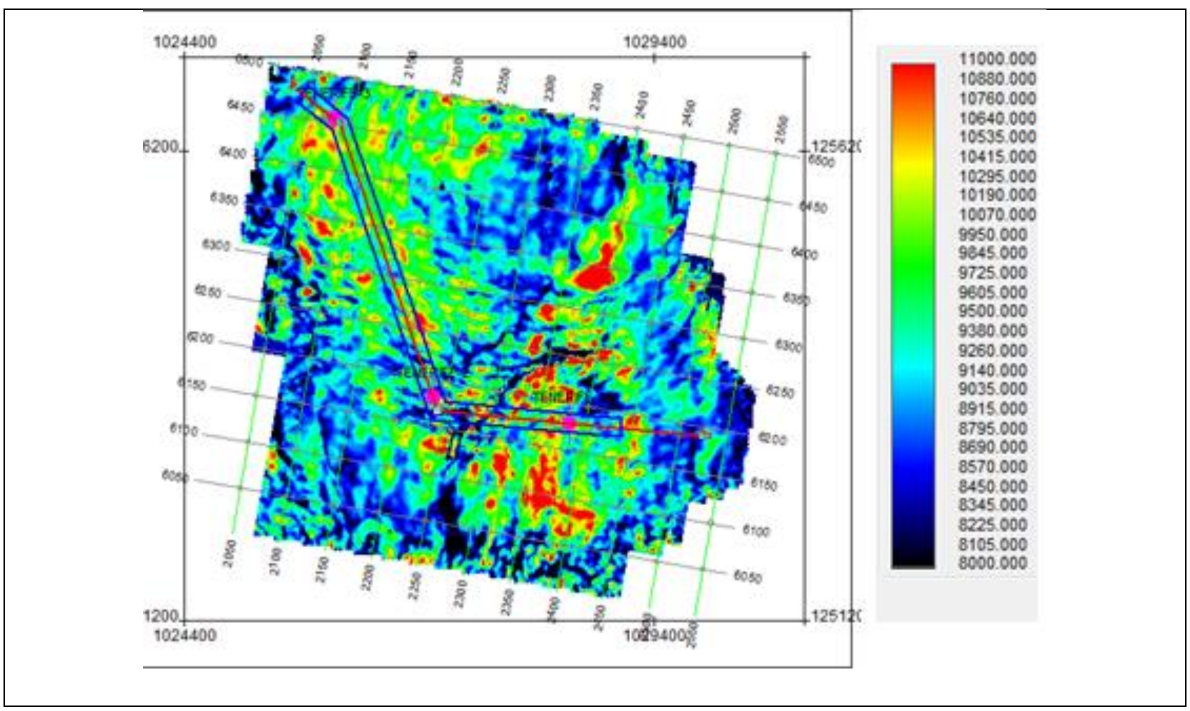

Figure 4.16: PP-impedance displayed in a horizon map coincident with the top of Mugrosa Formation.

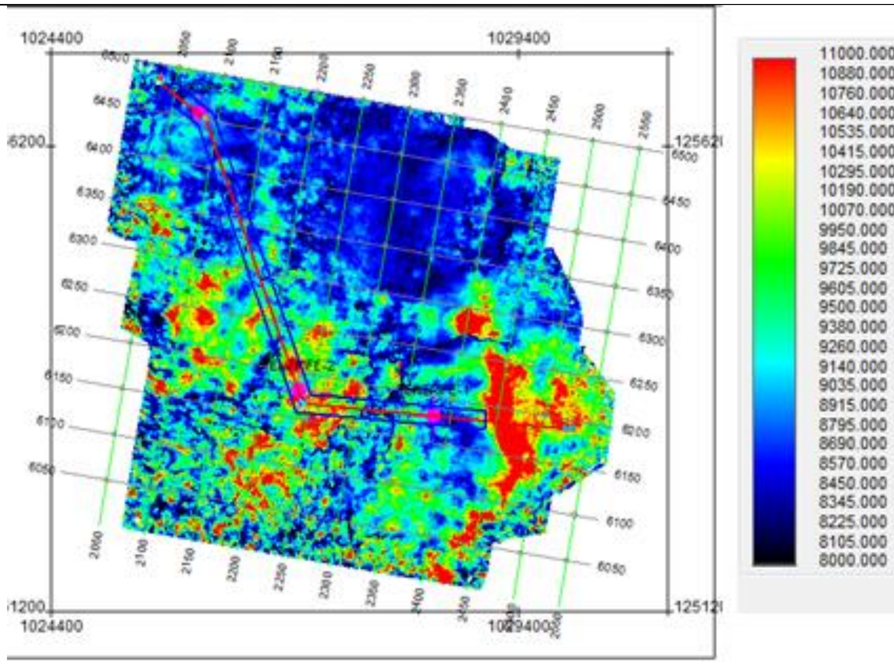

Figure 4.16 (cont.): PS-impedance displayed in a horizon map coincident with the top of Mugrosa Formation.

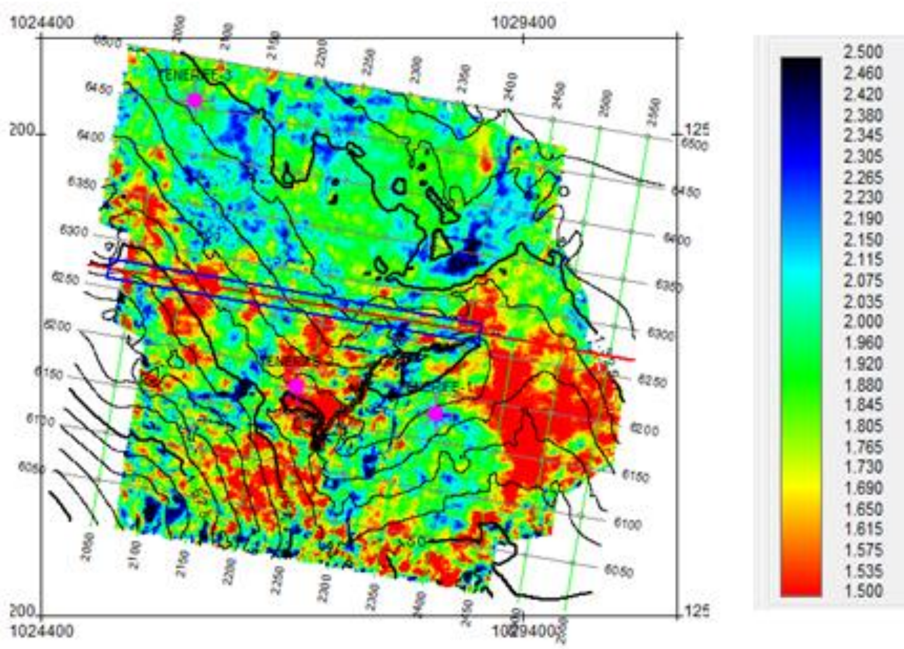

Figure 4.17: Vp/Vs displayed in a horizon map coincident with the top of Mugrosa-C Formation over imposed to Mugrosa-C PP-time structural map.

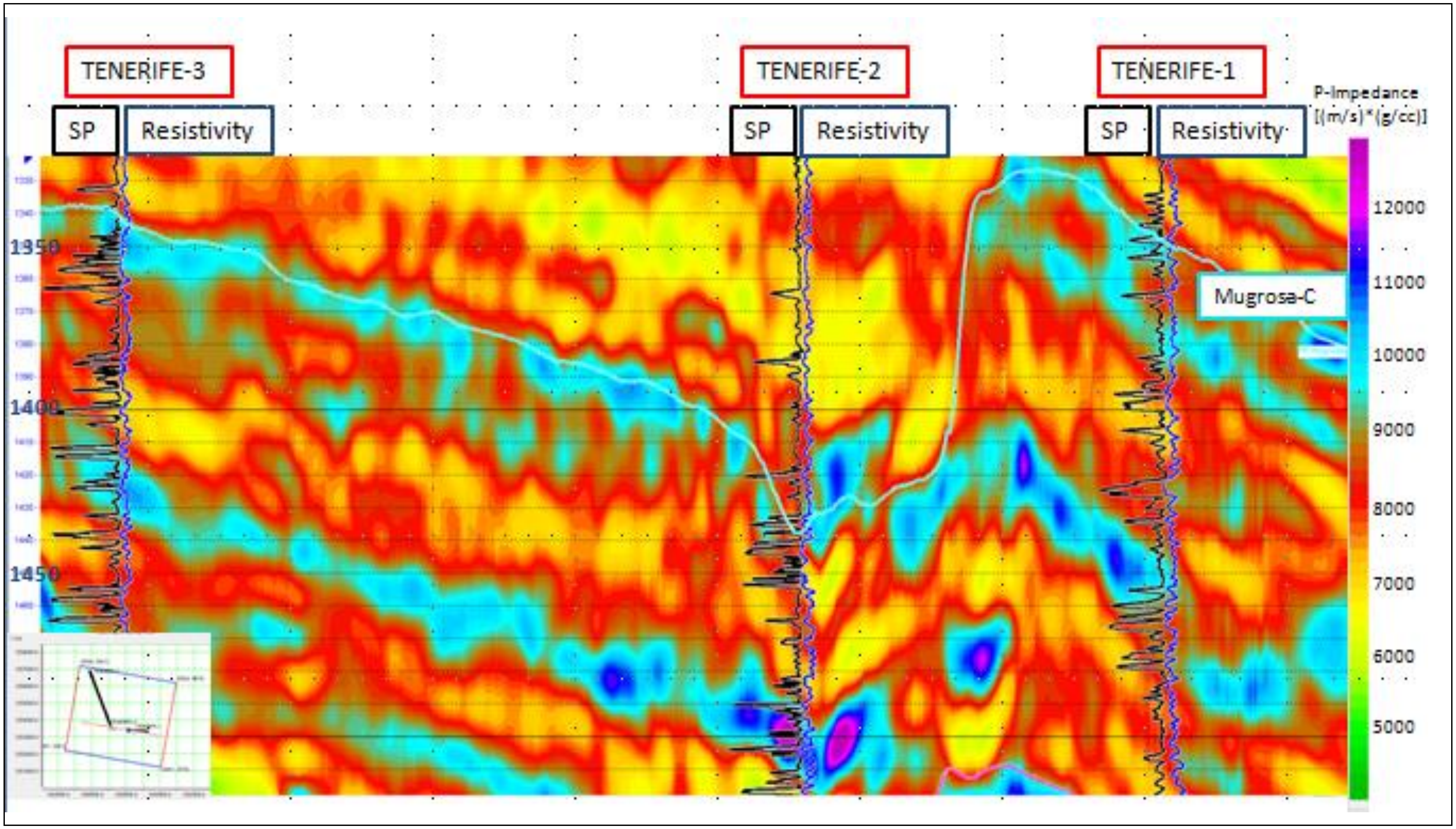

Figure 4.18: PP-impedance along the arbitrary line, SP and resistivity logs for Tenerife-1, - 2 and -3. The top of the Mugrosa Formation is marked in cyan.

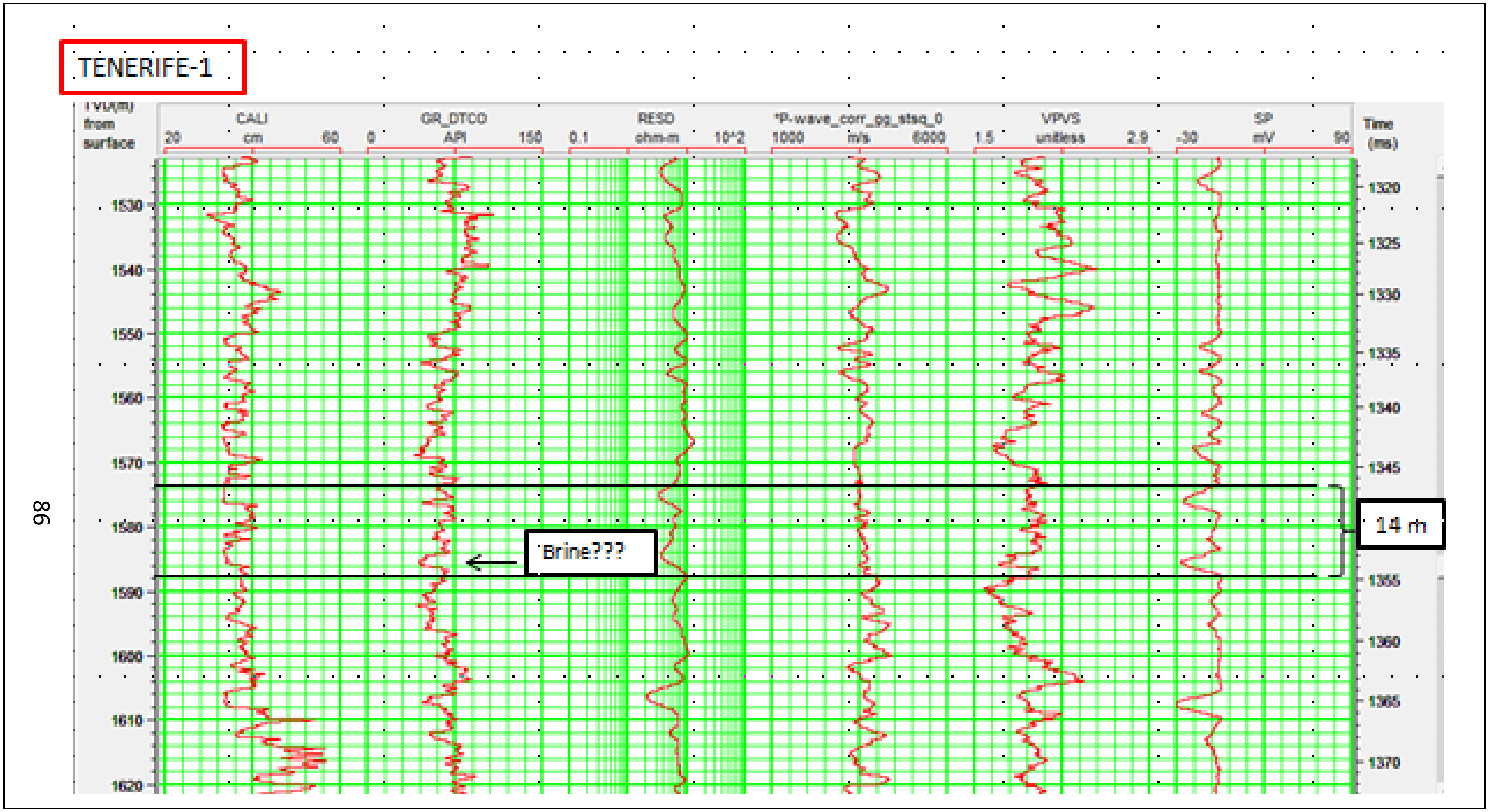

Figure 4.19 (a): Well logs for Tenerife-1. The Mugrosa Formation is marked between black lines.

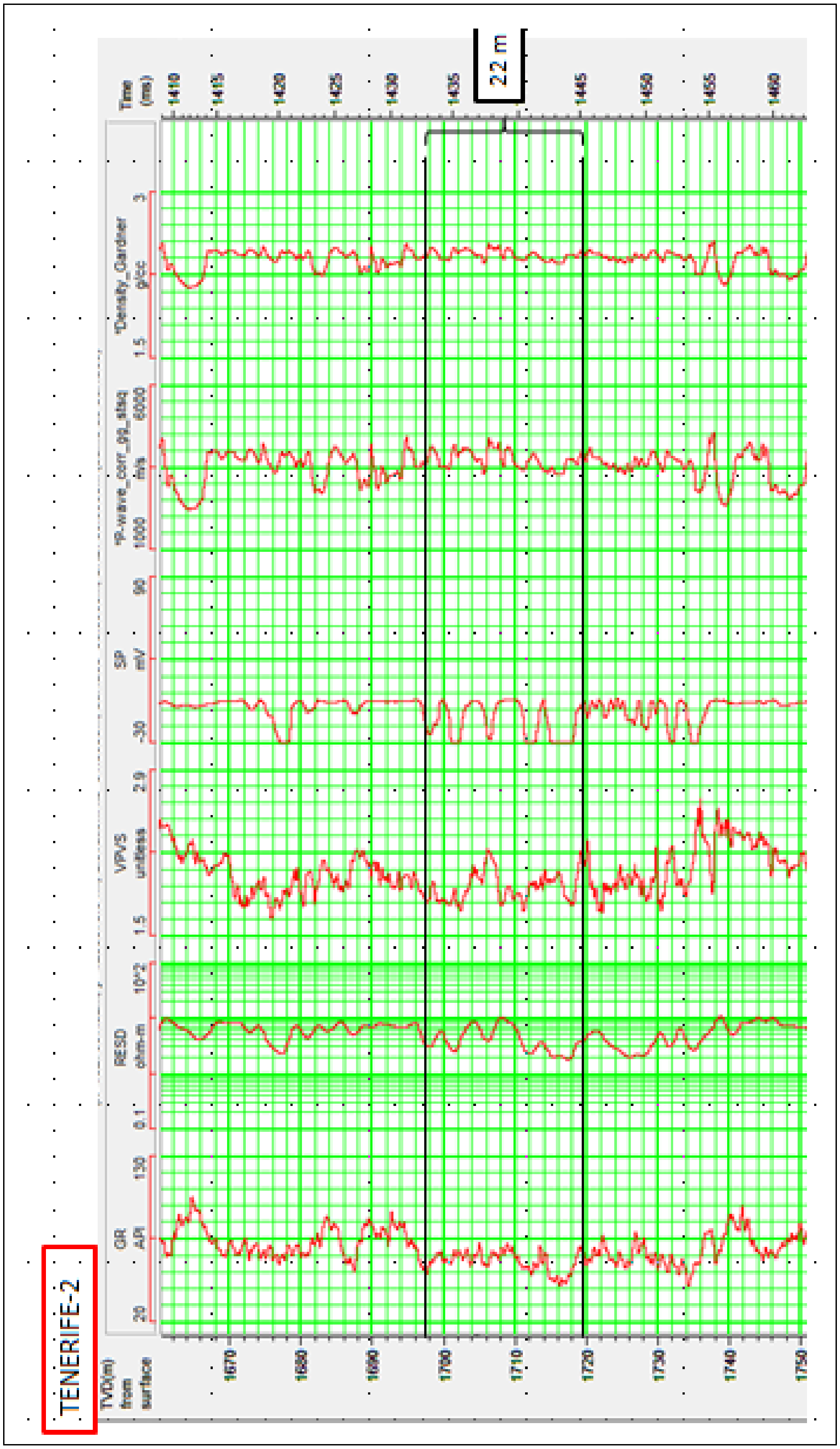

Figure 4.19 (b): Well logs for Tenerife-2. The Mugrosa Formation is marked between black lines.

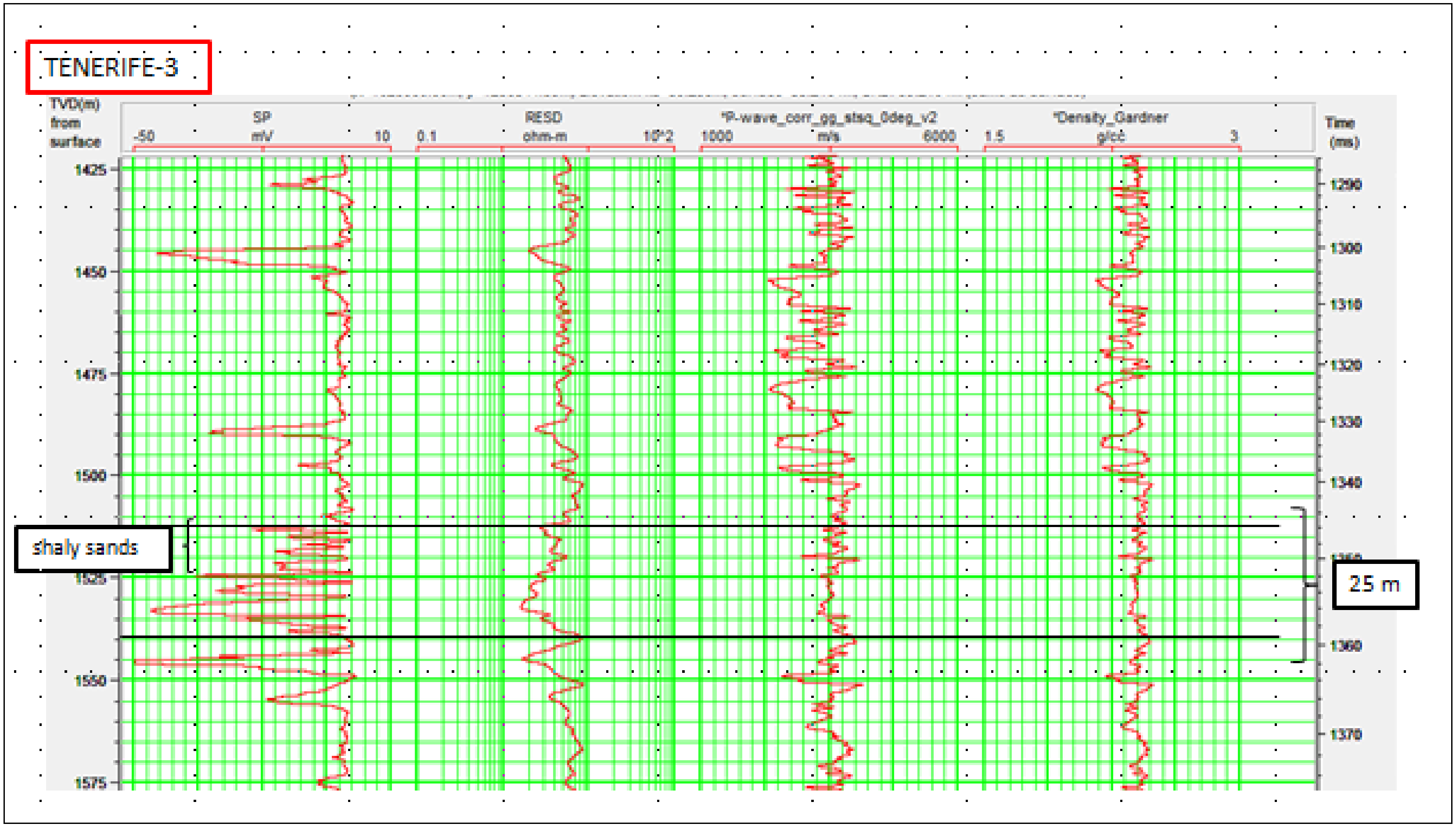

Figure 4.19 (c): Well logs for Tenerife-3. The Mugrosa Formation is marked between black lines.

Besides from the Mugrosa-C Formation, VP/Vs maps were computed for other interpreted horizons (tops of Mugrosa-B and Eocene Unconformity) to identify other possible target areas (Figure 4.20). These maps were not extracted from the top of Esmeraldas Formation as it was previously observed in the cross-plots that, in the interval Esmeraldas – Eocene Unconformity, Vp/Vs is not a good indicative of lithology.

Both horizon maps in Figure 4.20 are over imposed to each corresponding time structural map, allowing a good delineation of the faults. In both of them, high Vp/Vs values are associated with Tenerife-3, whereas Tenerife-1 and -2 are coincident with low Vp/Vs values, suggesting the presence of higher quality reservoir sands. Another possible target is marked with a star characterized by low Vp/Vs values in a structural high.

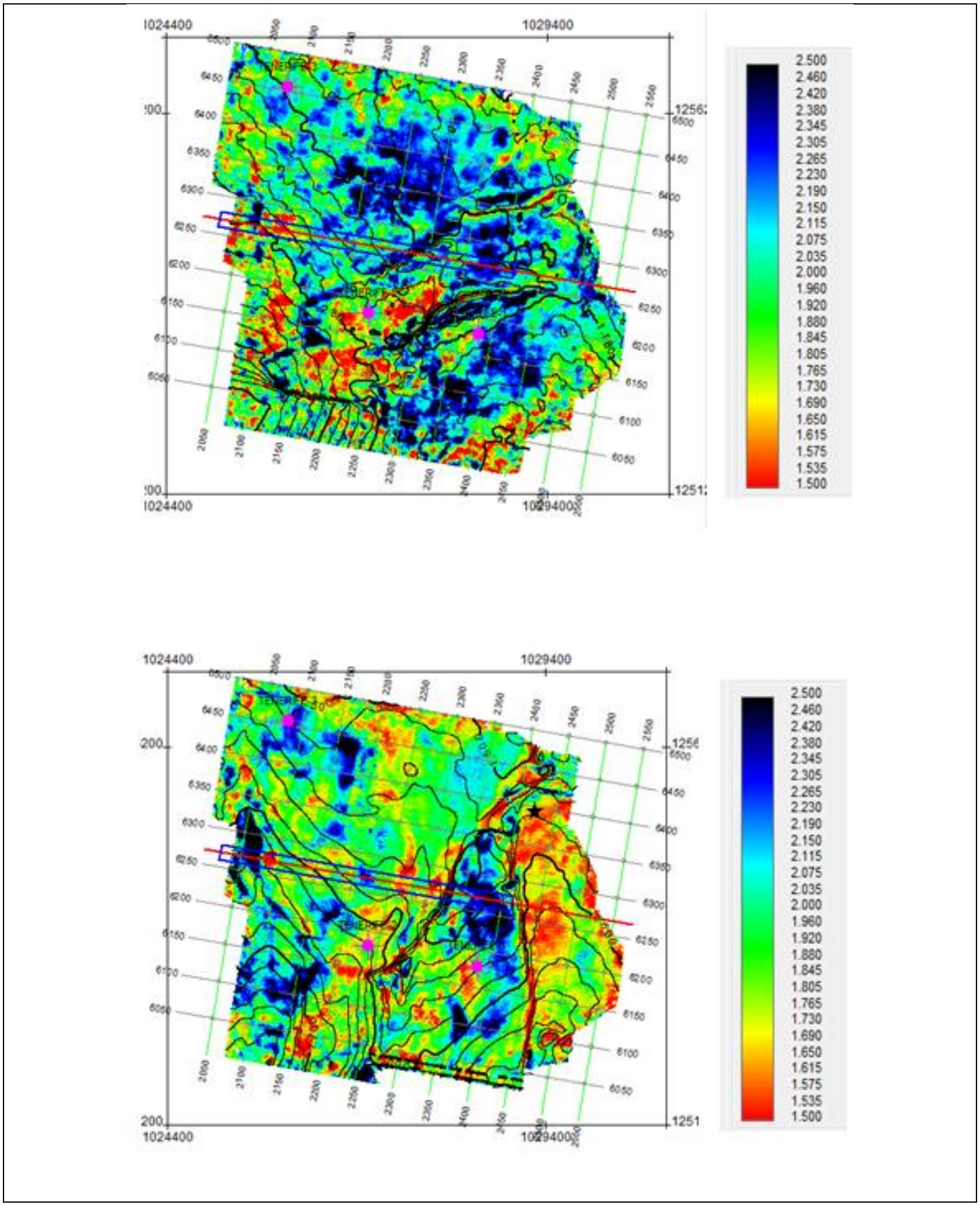

Figure 4.20: Vp/Vs displayed in a horizon map coincident with the top of (top) A2 and (bottom) the Eocene Unconformity, over imposed to each PP-time structural map.

Chapter 5: Discussion and Conclusions

This work was intended to investigate whether PS-waves can be used to better identify hydrocarbon-saturated sands than PP-waves alone. This is based on the fact PP- and PS-waves reflect differently at interfaces, usually providing information about lithology and/or fluid content.

The data for analysis corresponded to Tenerife Field, one of Ecopetrol's operated areas located in Middle Magdalena Valley, Colombia. It included a migrated 3D3C volume, raw shot gathers from two 2D3C test lines acquired with different amount of charge and different source and receivers depths; plus well logs and VSP from three wells in the field.

The first part of this work described a suggested processing flow for PP- and PS-waves which was applied to the vertical and radial channel. The vertical was processed following the conventional flow but for the radial channel some modifications were done to try to get the best possible PS-waves imaging. These included refraction statics computation by picking shear wave refractions; positive and negative offset separation for velocity picking, providing cleaner semblances and dynamic stacks; and DMO as an alternative to pre-stack time migration (PSTM). PP- and PS-migrated stacks were compared to analyze seismic responses of both types of waves with different acquisition parameters (shot size and depth, receiver burial). The results showed that, for this particular area, for PP-waves, increasing the amount of the charge, duplicating source and receivers' depth and even increasing the fold doesn't improve the image. But, for PS-waves, it was observed that the source size and depth are more influent than the receivers depth, and also more fold is critical. These conclusions are based in signal to noise ratio and continuity of events. These observations can be influent, in an economic sense, when planning future acquisitions in the area as they can help in choosing the appropriate acquisition parameters depending on the objective of the survey.

The first part of the seismic interpretation consisted in correlating the PP- and PS-2D migrated sections (Figure 4.6). The PS 2D seismic section was converted to PP-time to allow a direct correlation between the events. A good correlation was observed; also similar amplitudes were found in almost all the seismic section except for a portion (which was coincident with the target) where the events were more attenuated in the PP-stack than in the PS-. This lead to a more detailed interpretation, considering the well logs and 3D-3C PP- and PS-volumes, to try to map the reservoir sands within the target.

The reservoir is a sequence composed of sandstones (usually from 2 to 5 m thick), occasional carbonates and clays with a total thickness of 500 - 800 m within the Mugrosa Formation. The targets are these sand bodies, which are far below conventional seismic resolution, but due to the meandering river sedimentation depositional environment, they can extend to 30 m.

The goal of the 3C-3D interpretation was to be able to map these hydrocarbon saturated sands by correlating the well logs, PP- and PS-3D migrated volumes, plus PP- and PS-model-based inversions. Cross-plots of Vp, Vs, Vp/Vs, GR, and resistivity logs from the three wells were analyzed, suggesting the presence of hydrocarbon sands and confirming that Vp/Vs maps could be a good indicator of lithology and/or fluid saturation.

This led to the building of two types of Vp/Vs maps: a regional and a high resolution one. The regional Vp/Vs map was computed from three of the interpreted horizons, enclosing the Mugrosa-C Formation, in the 3D-3C migrated volumes. The high-resolution Vp/Vs maps were obtained by the quotient of the Acoustic and Shear wave impedances, obtained from the PP- and PS-inversions.

A horizon map along the top of the Mugrosa-C Formation of the Vp/Vs volume was analyzed correlating low Vp/Vs values with one of the producing wells (Tenerife-2). Tenerife-1 (productive) and -3 (dry) didn't present low Vp/Vs values, being this possibly related to the character of the Mugrosa sands in this wells. Also Vp/Vs maps were computed for other two interpreted horizons suggesting other possible target areas determined by low Vp/Vs values in a structural high.

Thus, in the Tenerife Field, Vp/Vs is responding to the reservoir quality; a good stack of clean sands is clearly determined by low Vp/Vs, whereas a stack of shaly sands doesn't present Vp/Vs anomalies.

To conclude, a good lithology estimation was achieved based on Vp/Vs maps, but it could be highly improved with high resolution seismic data. Future work could include interpretation and post-stack joint inversions of high resolution PP- and PS-seismic volumes for a better delineation of the sand/shale bodies; pre-stack inversions for a reliable density determination; and an AVO and fluid substitution analysis to see the effect of hydrocarbon/brine saturation at the possible reservoir sands.

References

Agudelo, W., E. Pineda, R. Gomez, J. Guerrero, N. Rojas, R. Stewart, and N. Van de Coevering, 2013, Using converted-wave seismic data for lithology discrimination in a complex fluvial setting: Tenerife oil field, Middle Magdalena Valley, Colombia: The Leading Edge, **32**, p. 72-78.

Barrero, D., A. Pardo, C. A. Vargas, and J. F. Martinez, 2007, Colombian Sedimentary Basins: Nomenclature, Boundaries and Petroleum Geology, a New Proposal: Agencia Nacional de Hidrocarburos – A.N.H

Bland, H. C., and E. V. Gallant, 2001, Wind noise abatement or 3-C geophones: CREWES Research Report, Volume 13.

Garotta, R., 1987, Two-component acquisition as a routine procedure: In Danborn S. H. and S. N. Domenico, eds., Shear-wave exploration: Soc. Expl. Geophys., p. 122-136.

Gomez, E., 2001, Tectonic Controls on the Late Cretaceous to Cenozoic Sedimentary Fill on the Middle Magdalena Valley Basin, Eastern Cordillera and Llanos Basin, Colombia [Ph.D thesis]: Ithaca, New York, Cornell University, p.619.

Gomez, E., T. Jordan and R. Allmendiger, 2005, Syntectonic Cenozoic sedimentation in the Northern middle Magdalena Valley Basin of Colombia and implications for exhumation of the Northern Andes: Geological Society of America Bulletin, p. 547-569.

Guliyev, E., T. L. Davis, and R. J. Michelana, 2006, Application of multicomponent seismic for Vp-Vs ratio extraction: tight gas sandstone example, Rulison field, Colorado: 76th Annual International Meeting, SEG, Expanded Abstacts, p. 1123-1127.

Halliburton, ProMAX® Tutorial, Common Offset F-K DMO.

Hardage, B.A., M. V. DeAngelo, P. E. Murray, D. Sava, Multicomponent seismic technology: Society of Exploration Geophysicists, 2011.

Harrison, M. P., 1992, Processing of P-SV Surface Seismic Data: Anisotropy Analysis, Dip Moveout, and Migration: [Ph. D Thesis]: University of Calgary.

ION, Tenerife 3C 3D Converted Wave Processing Report, 2010: ION Technical Report.

Levin, F. K., 1971, Apparent velocity from dipping interface reflections: Geophysics, **36**, p. 510-516.

Lobo, Alvarez A., 1999, Evaluacion Integrada de Yacimientos del Campo La Cira-Infantas: Reporte Tecnico – Ecopetrol.

MacLeod, M., R. Hanson, M. Hadley, K. Reynolds, D. Lumley and T. Probert, 1999, The Alba field OBC seismic survey: SEG Expanded Abstracts, **18**, 725-727.

Morales, L.G., 1958, General geology and oil occurrences of Middle Magdalena Valley, Colombia: In L. G. Weeks, ed., Habitat of oil: APPG, p. 641-695.

Moreno, C. J., Horton B. V., Caballero A., Mora M., Parra and J. Sierra, 2011, Depositional and provenance record of the Paleogene transition from foreland to hinterland basin evolution during Andean orogenesis, northern Moddle Magdalena Valley Basin, Colombia: Journal of South American Earth Sciences, **32**, p. 26-263.

Mulholland, M., 1943, The history of development and general geology of the La Cira and Infantas oil fields: Tropical Oil Company; Internal Report.

Prieto, M.E., Mantilla J., Owens B. K., Lobo A. and F. Fernandez, 2009, Redevelopment Progress for Colombia’s La Cira-Infantas Field: Society of Petroleum Engineers, SPE 120794

Ramirez, R. E., 1998, Stratigraphy of the Tertiary of the Middle Magdalena Basin (Colombia), central and northern parts, [M.S. Thesis]: Austin, University of Texas, p.199.

Ronen, J. and J. F. Claerbout, 1985, Surface-consistent residual statics corrections by stack power maximization: Geophysics, **50**, p. 2759-2767.

Sanderson, W. J., 1951, Geological report on the La Cira and Infants oil Fields: Tropical Oil Company; Internal Report.

Schafer, A. W., 1991, Converted-wave statics methods comparison: CREWES report, 107-125.

Sheriff, R. E., 1991, Encyclopedic Dictionary of Exploration Geophysics, Third Edition: Society of Exploration Geophysicists, p. 384.

Stewart, R. R., J. E. Gaiser, R. J. Brown and D. C. Lawton, 2003, Converted wave seismic exploration: Applications: Geophysics, **68**, p. 40-53.

Stewart, R.R., Gaiser J. E., Brown R. J., and D. C. Lawton, 2002, Tutorial - Converted-wave seismic exploration: Methods: Geophysics, **67**, p.1348-1363.

Swolfs, H., 1947, The stratigraphy of the La Cira-Casabe-Cimitarra area with an appendix on longitudinal section through the Western Middle Valley wells: Tropical Oil Company; Internal Report.

Tatham, R. H., and M. D. McCormack, 1991, Multicomponent seismology in petroleum exploration: Society of Exploration Geophysicists.

Velasquez-Espejo, A. J., 2012, 3D Multicomponent Seismic Characterization of a Clastic Reservoir in the Middle Magdalena Basin, Colombia, [M.S. Thesis]: Colorado School of Mines.

Wei, X. and X. Li, 2003, Case study of using converted PS-waves to image gas reservoirs in the Ordos Basin, China: SEG Expanded Abstracts, **22**, p. 769-772.

Appendix A

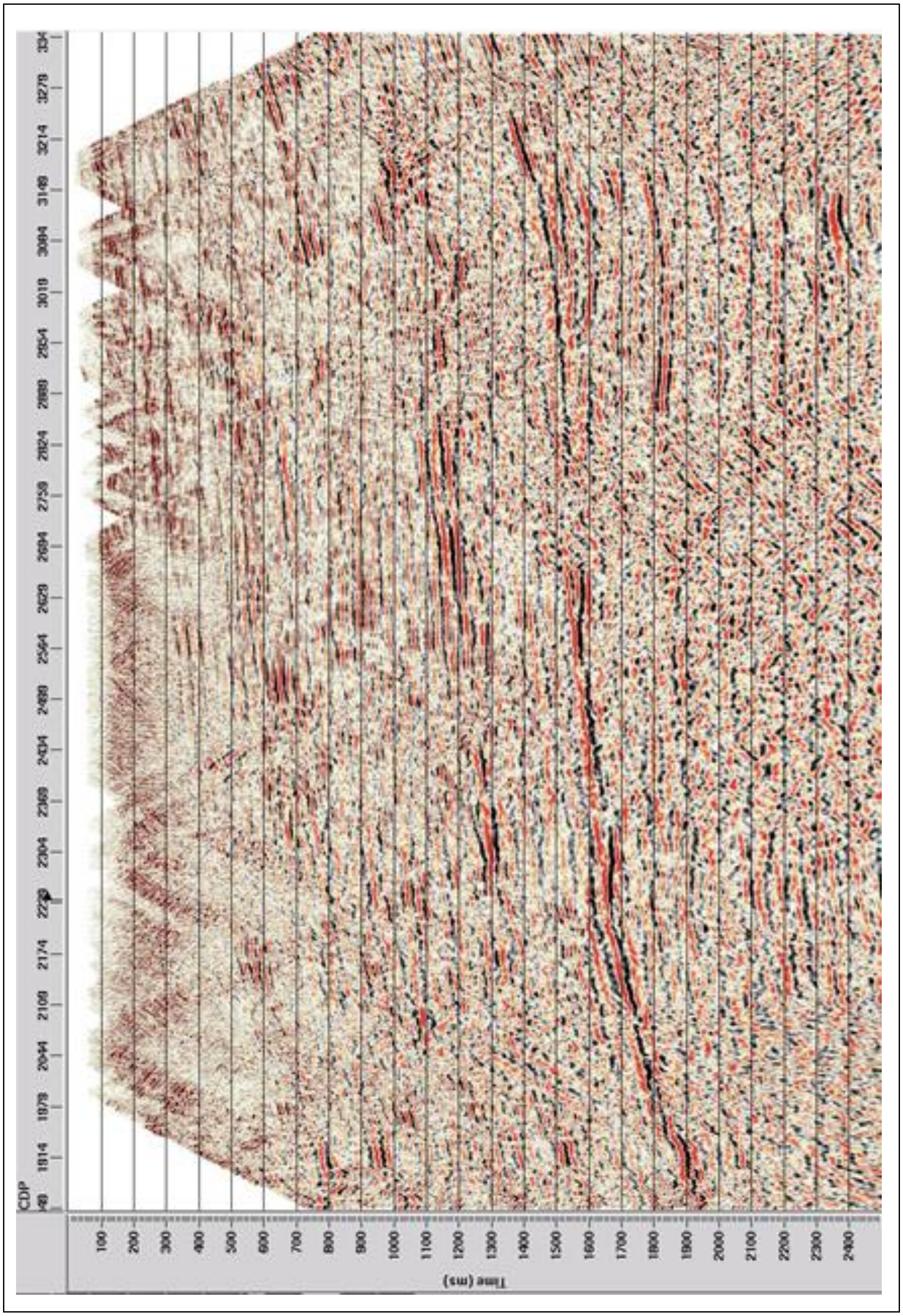

Figure A.1: PP - Stack with elevation statics and a sparse velocity.

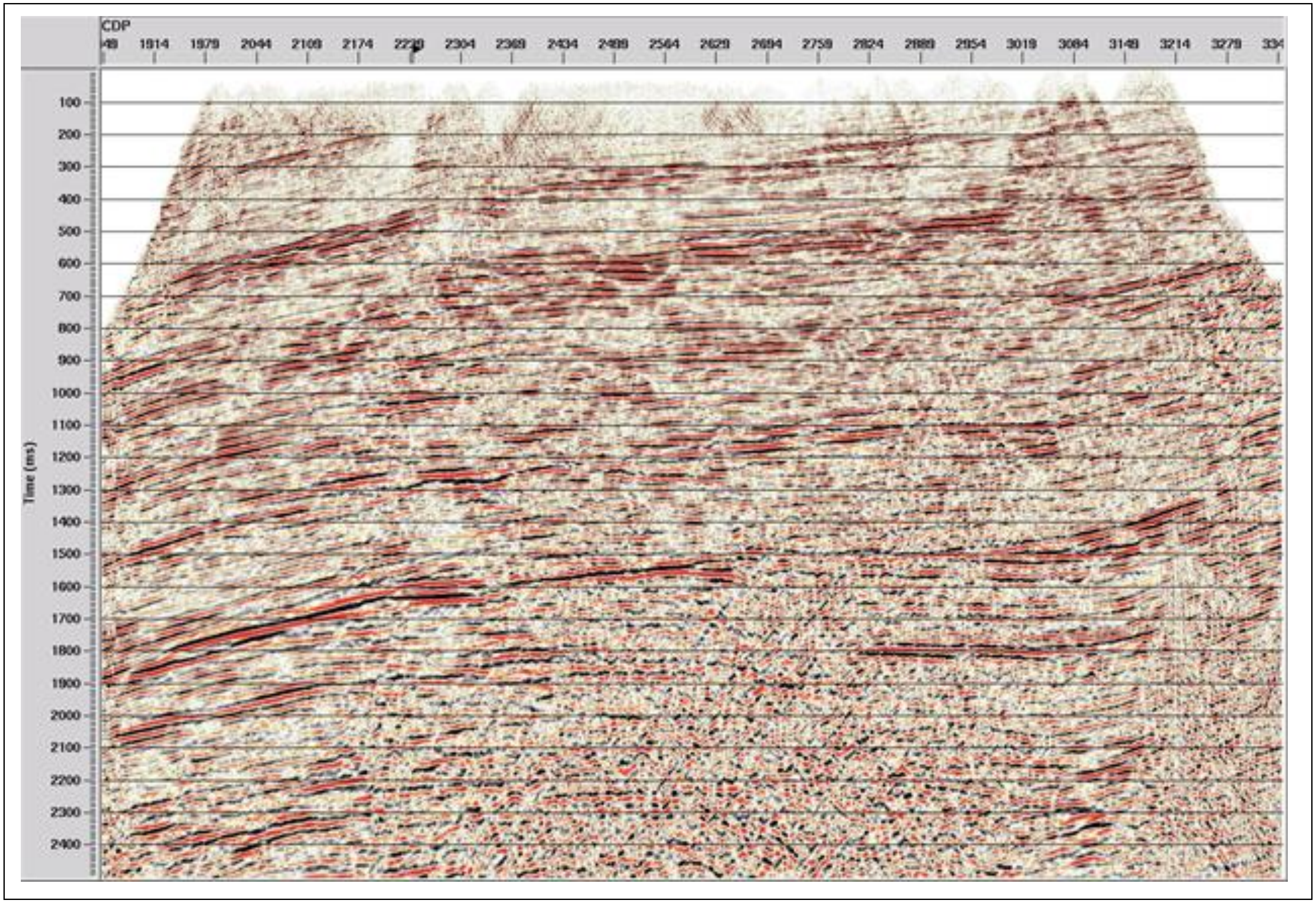

Figure A.2: PP - Stack after a velocity picking every 500 m and a second run of residual statics.

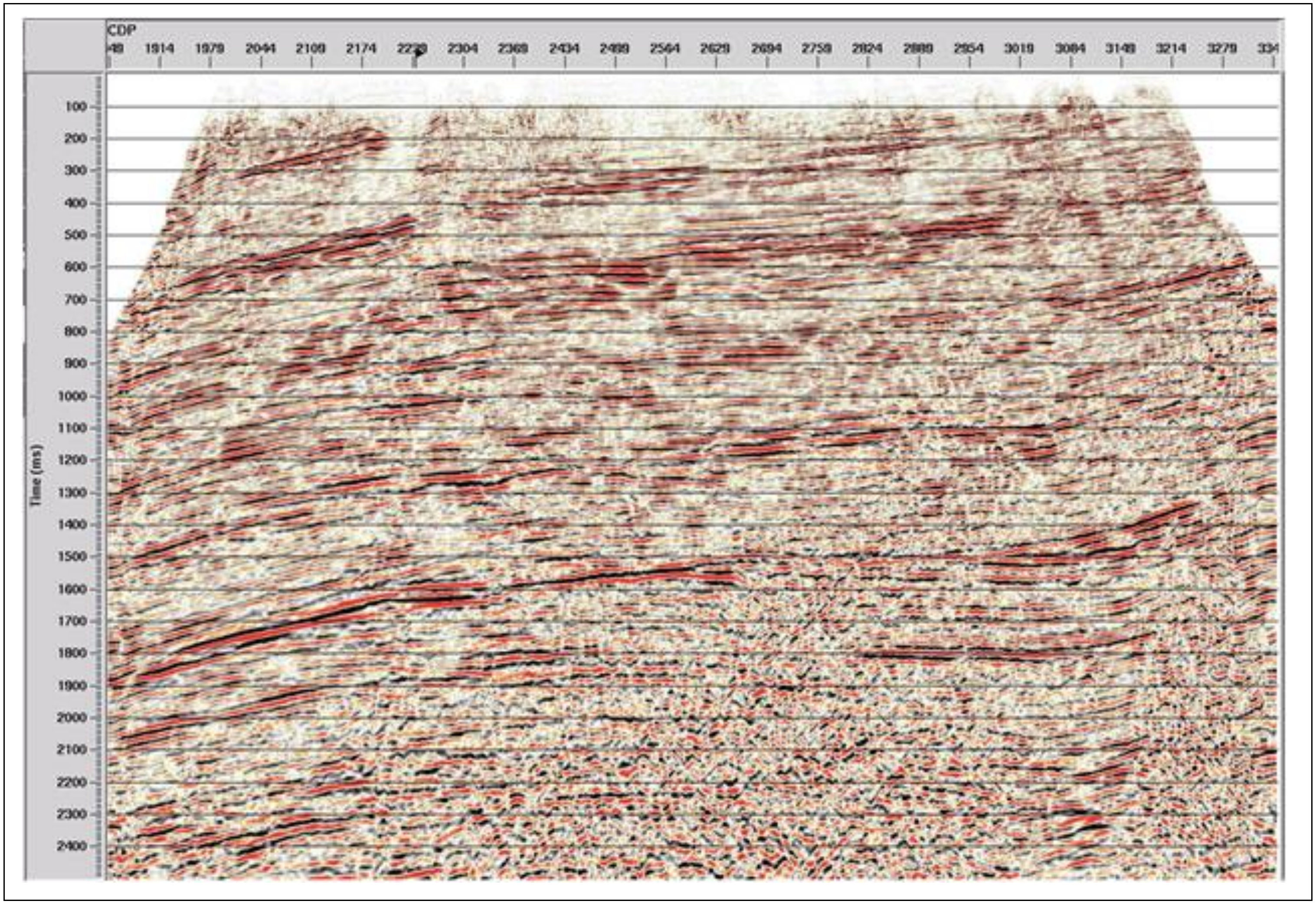

Figure A.3: PP - Stack after CDP-domain noise attenuation and trim statics.

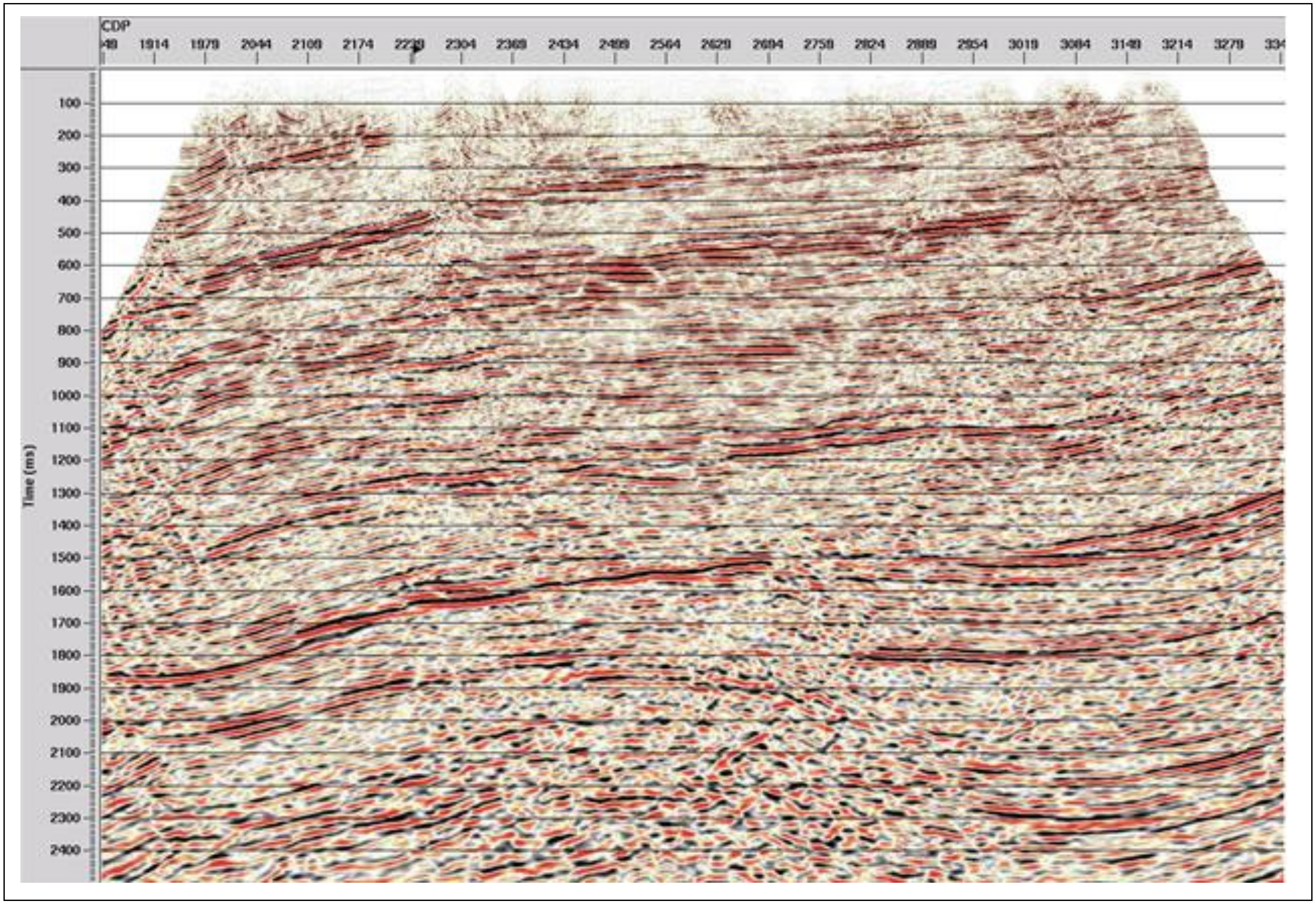

Figure A.4: PP - Post-stack Time Migration.

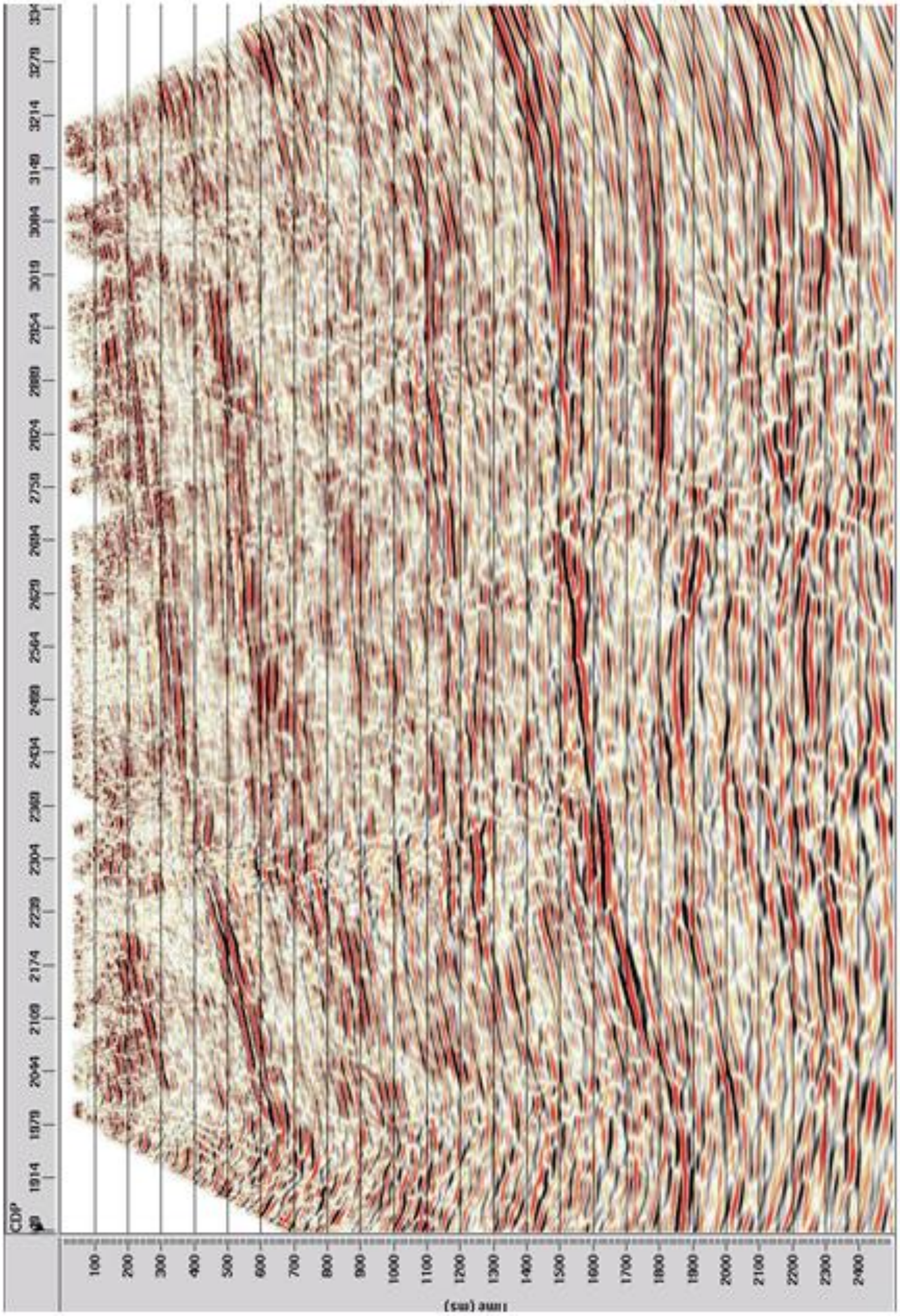

Figure A.5: PP - Pre-stack Time Migration (PSTM).

Appendix B

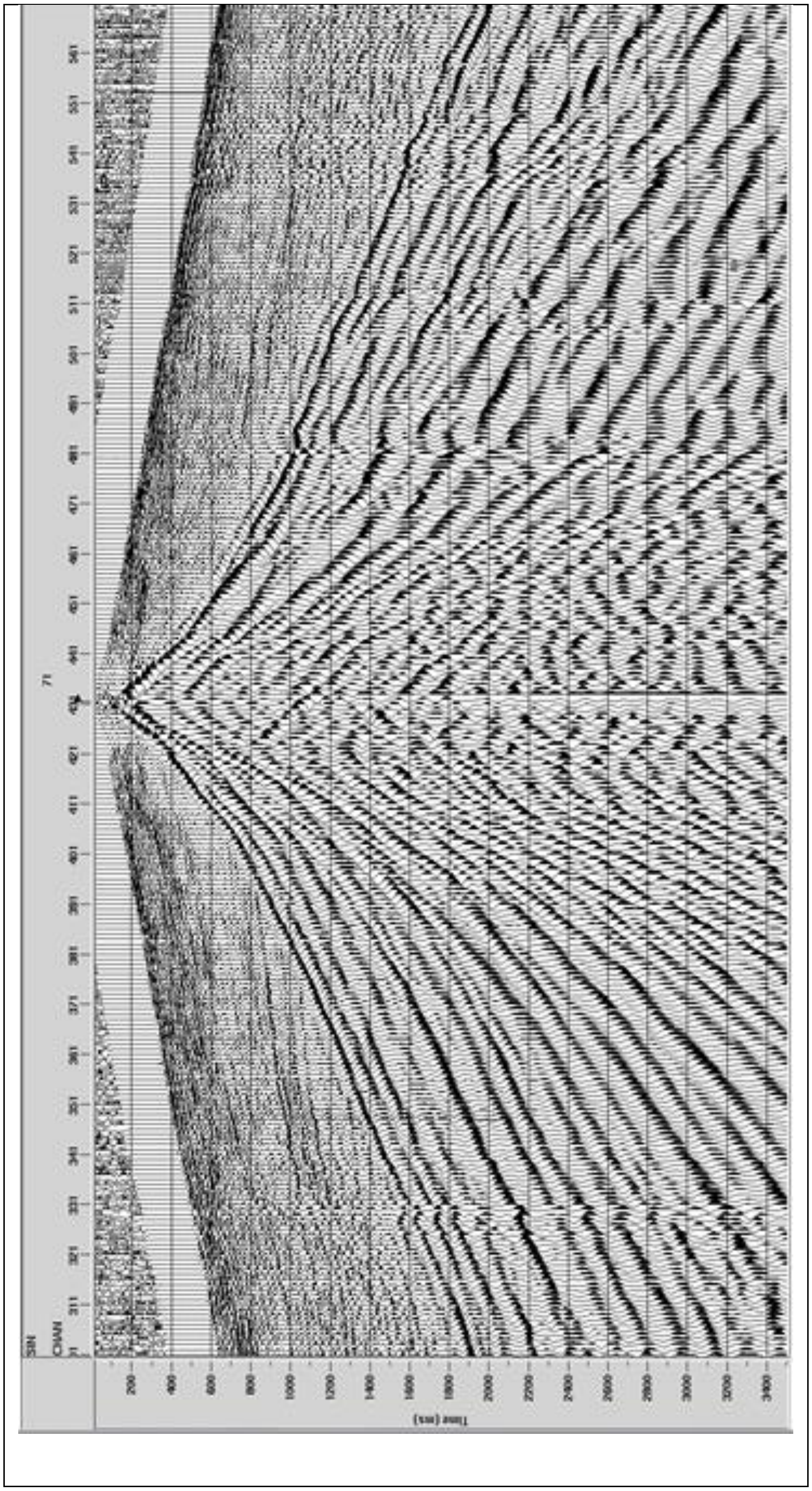

Figure B.1: PS – Field data before Polarity Reversal.

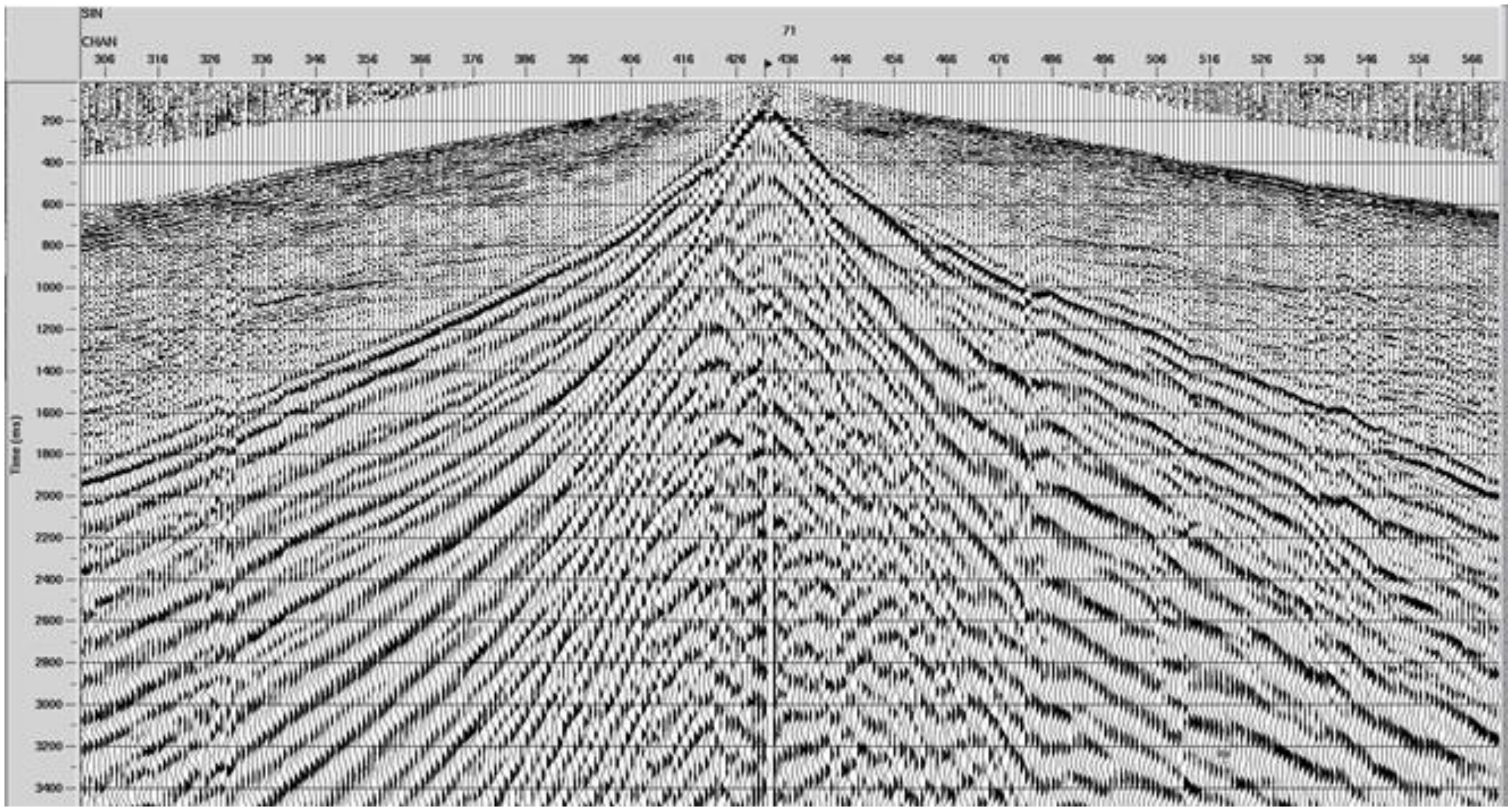

Figure B.2: PS – Field data after Polarity Reversal.

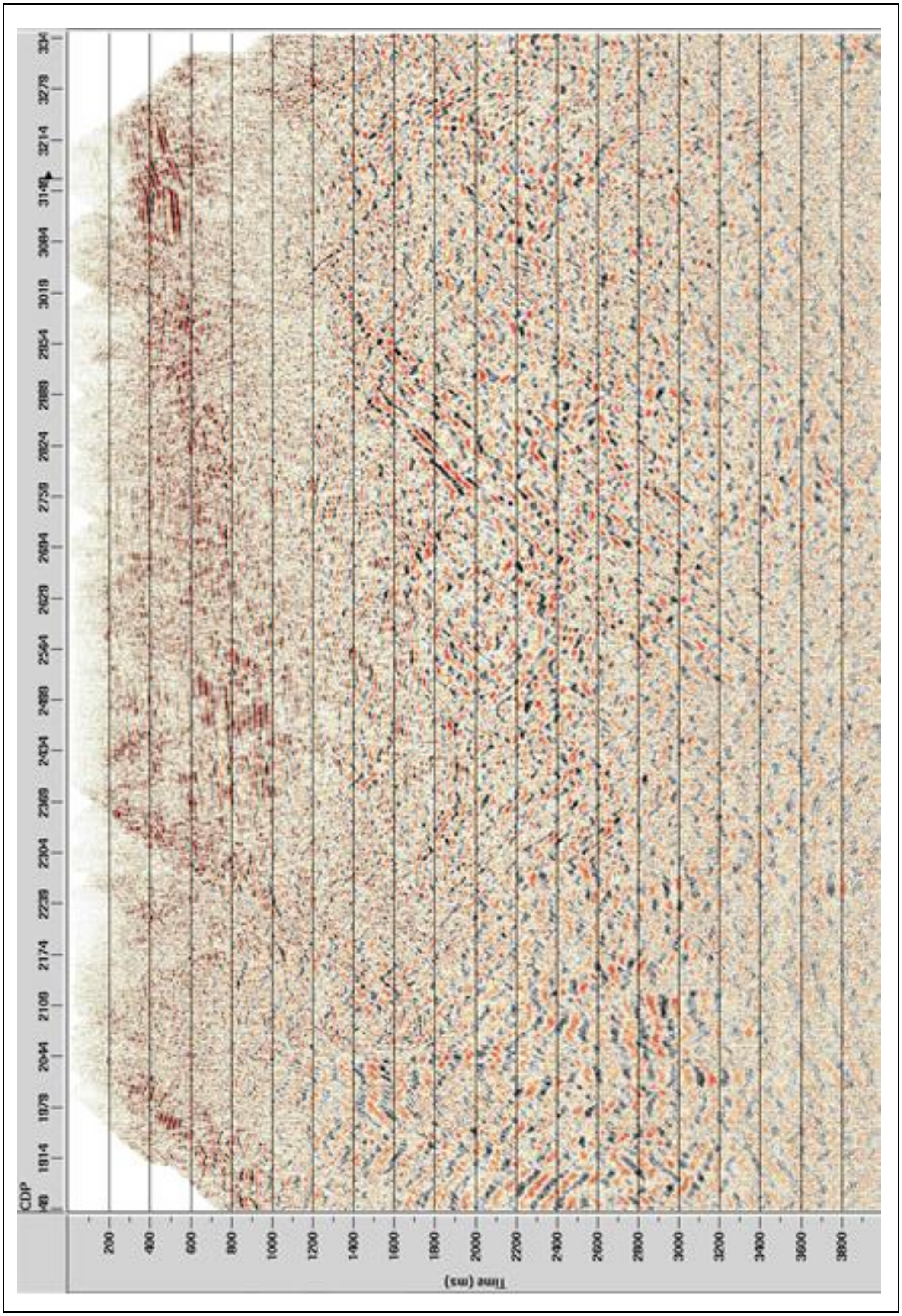

Figure B.3: PS - Stack with elevation statics and an initial velocity.

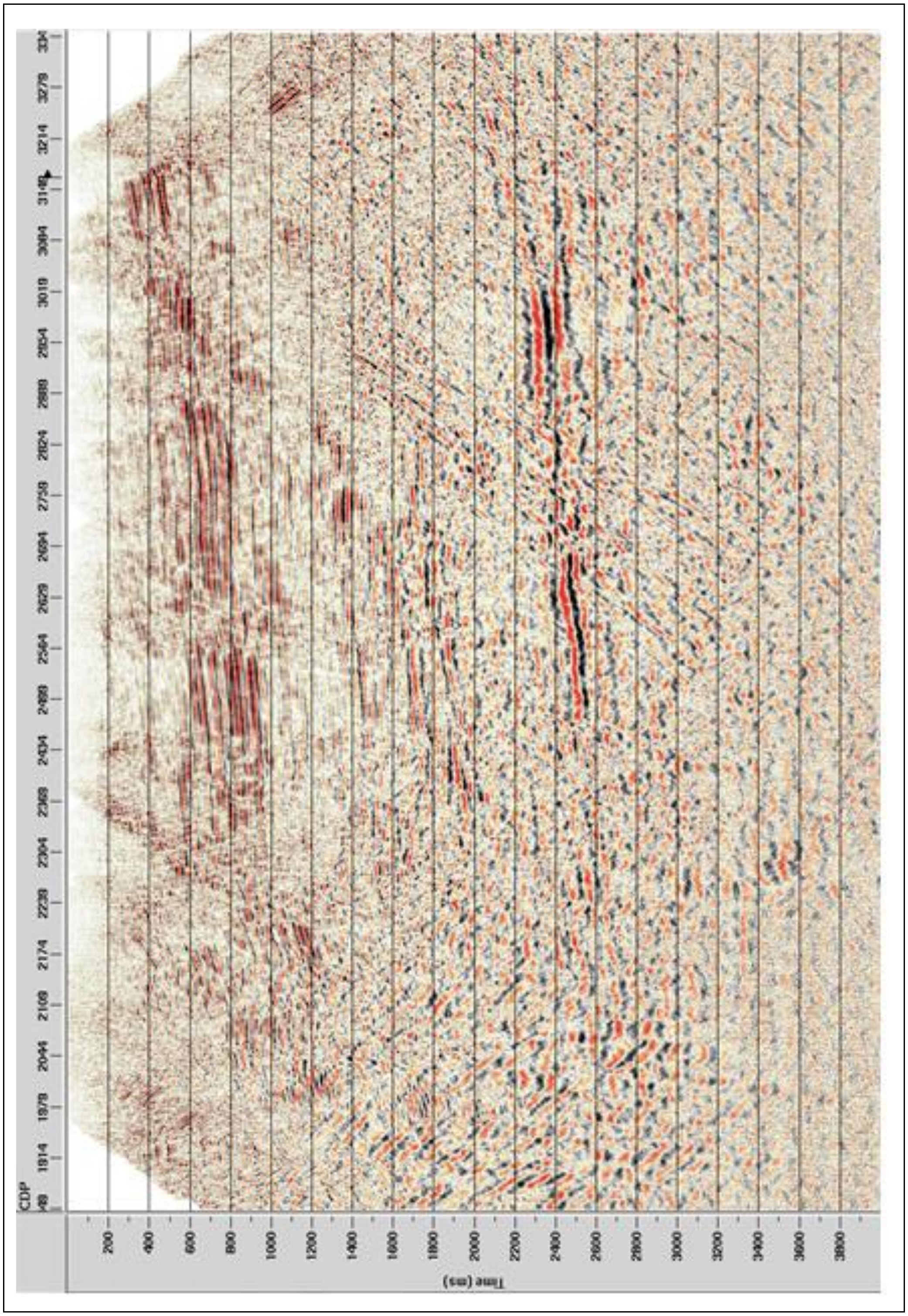

Figure B.4: PS - Stack with second velocity picking and residual statics.

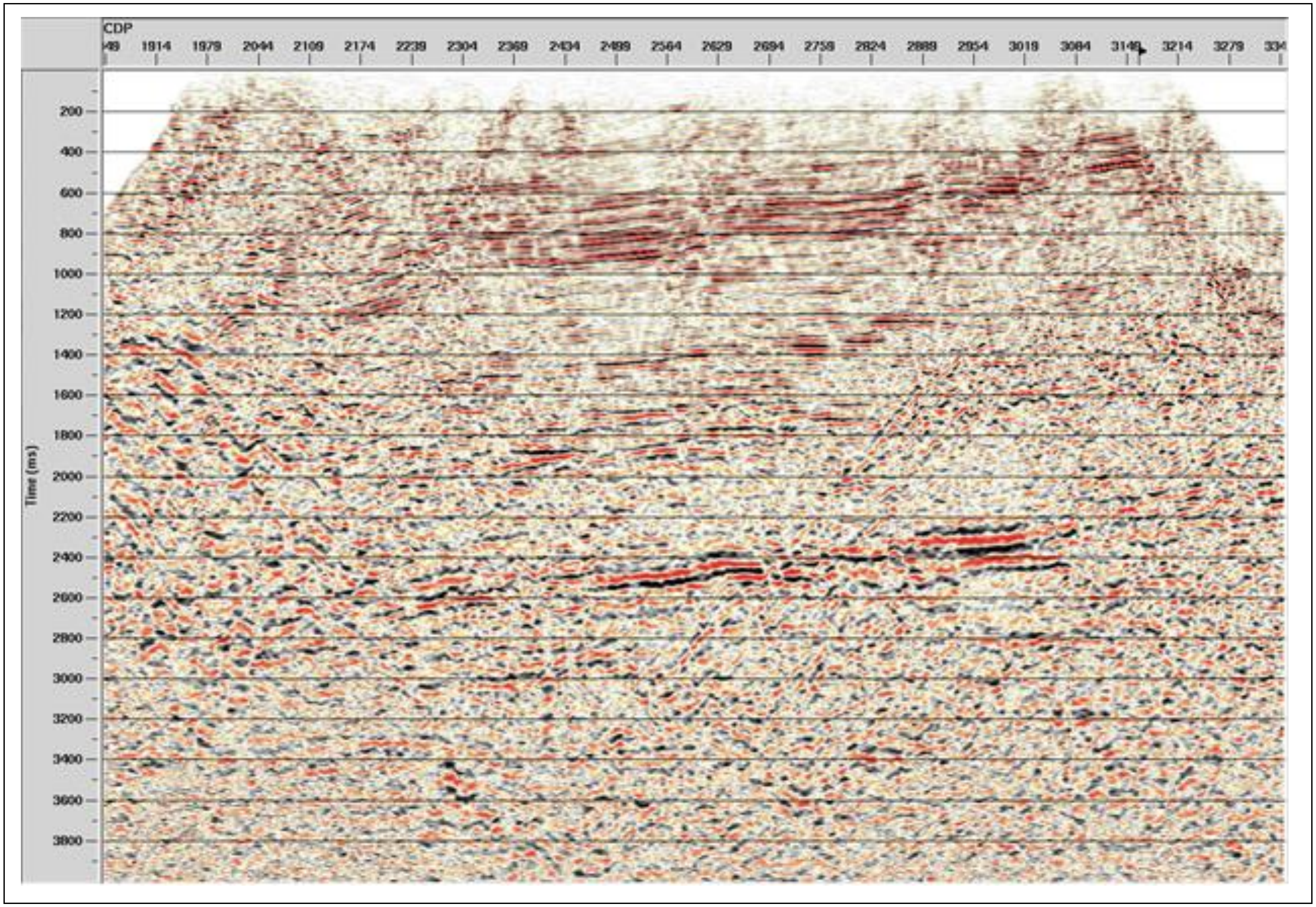

Figure B.5: PS - Stack after CDP-domain noise attenuation and trim static.

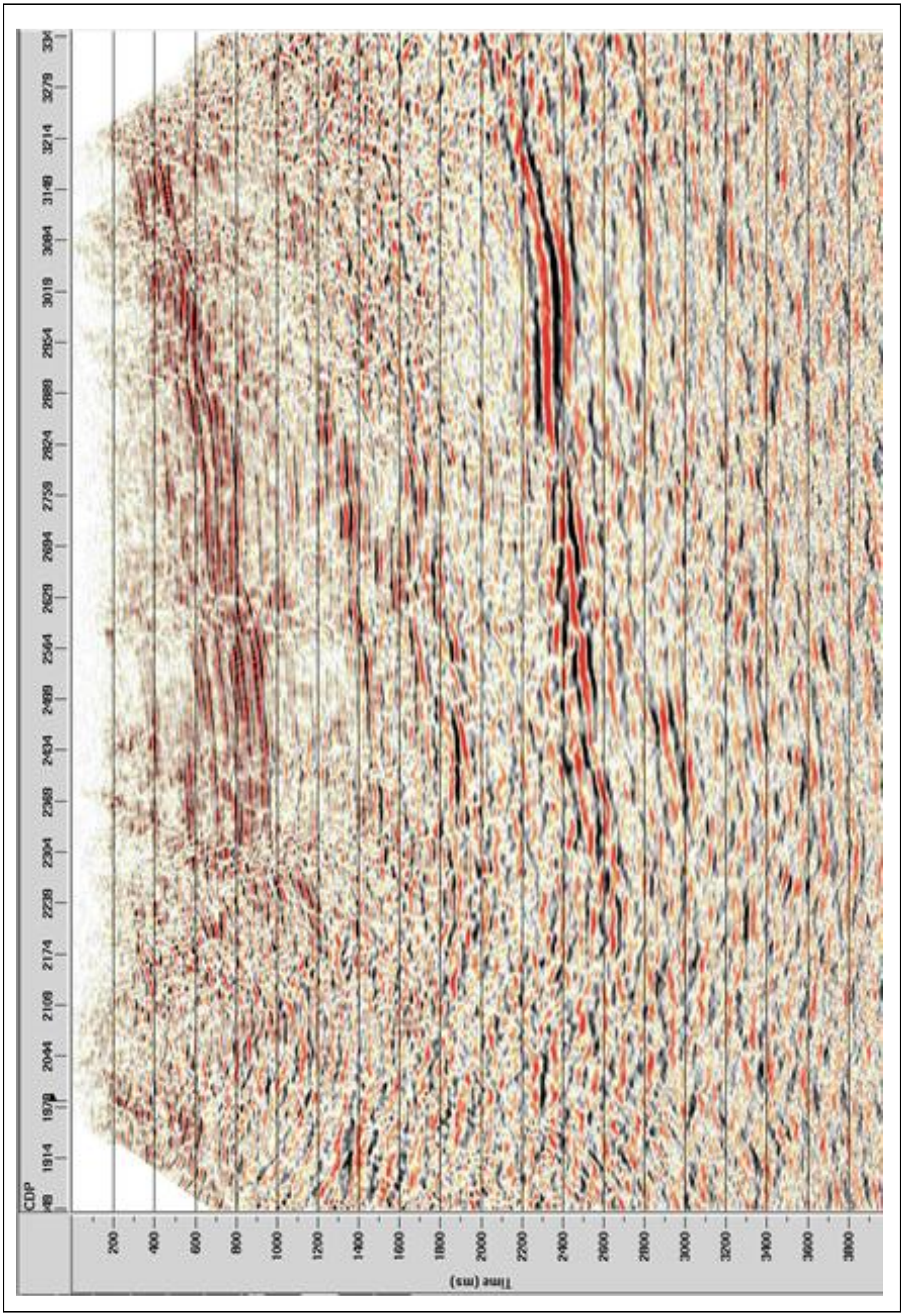

Figure B.6: PS - Stack after DMO.